Energy Saving Position Control of Valve Controlled and Direct Pump Controlled Pneumatic Actuators

Energy Saving Position Control of Valve Controlled and Direct Pump Controlled Pneumatic Actuators

By

Yufeng Huang, B.Eng.

A Thesis

Submitted to the School of Graduate Studies

In Partial Fulfillment of the Requirements

For the Degree

Master of Applied Science

McMaster University

MASTER OF APPLIED SCIENCE (2024) McMaster University
(Mechanical Engineering) Hamilton, Ontario, Canada

TITLE: Energy Saving Position Control of Valve Controlled and Direct Pump Controlled Pneumatic Actuators

AUTHOR: Yufeng Huang
B.Eng., (MECHANICAL DESIGN AND MANUFACTURING AND AUTOMATION)
Hefei University of Technology, Hefei, China

SUPERVISOR: Dr. Gary M. Bone, Professor

NUMBER OF PAGES: xxi, 115

Lay Abstract

Pneumatic actuators are a durable and reliable actuation method. However, they suffer from low system energy efficiency due to misuse of compressed air, leakage, and the throttling losses of pneumatic components. In this thesis, we study the position control of two different pneumatic circuits, known as direct pump control (DPC) and valve control (VC), and compare their position control performance and energy consumptions. The pneumatic system was mathematically modelled first. A novel air pump model and a novel friction model were developed. Model-predictive control algorithms were then proposed for each circuit. Each algorithm finds the optimal combination of pump and valves binary states for controlling the position of the load and reducing energy consumption. Experiments were conducted to find the best controller parameters. The results from long duration experiments show that VC generally has better position control performance in steady state than DPC, but it consumes more energy than DPC.

Abstract

Pneumatic actuators are reliable and durable. They are also friendly to the environment, and low-cost compared with hydraulic systems and electrical actuation systems. One of the bottlenecks constraining the development of pneumatic systems is they suffer from low system energy efficiency due to misuse of compressed air, leakage, and the throttling losses of pneumatic components. We hypothesize that the energy efficiency of a position controlled pneumatic actuator can be improved by designing a better pneumatic circuit and controlling it with an advanced control algorithm.

In this thesis, we study the position control of two different pneumatic circuits, known as direct pump control (DPC) and valve control (VC), and compare their position control performance and energy consumptions. The DPC circuit consists of a double acting pneumatic cylinder that is controlled by two positive displacement air pumps, and four ON/OFF solenoid valves. The VC circuit consists of the same cylinder controlled by four ON/OFF solenoid valves, and an air tank that is pressurized by a single pump. Nonlinear system models of the two circuits were developed, in which a novel air pump subsystem model and a novel friction model were proposed and validated by comparing simulation and experiment results.

Discrete-valued model predictive control algorithms were then developed for each circuit. These algorithms were designed to find the optimal combination of pump and valves binary states for controlling the position of the load and reducing energy consumption. After tuning their parameters based on a series of short experiments, long duration experiments were conducted to allow the position control performance and energy consumption of the two circuits to be compared fairly.

From the results of the long duration experiments, the root mean square error and mean absolute error of DPC are 19.77% and 13.42% lower than those of VC. However, the mean steady state error is 0.74 mm, and the mean overshoot is 1.73 mm, which are 17.46% and 53.10% higher than VC's results. This means VC has better steady state precision, while DPC is superior at tracking the setpoint trajectory transients. Regarding the energy consumption, 92.84% of the system energy was saved using DPC with one working cycle, and 36.64% was saved when the number of working cycles was increased to 29, which proves DPC is more energy efficient.

Acknowledgment

Above all, I would like to express my sincere gratitude to my research supervisor, Dr. Gary M. Bone, for providing me such a precious opportunity to learn and carry out research at Robotics and Manufacturing Automation Lab (RMAL). He is my first mentor guiding me through the rigorous academic training, and I learned a lot from his committed and responsible personalities on both research and teaching. With his support and insights, I have achieved my goal of pursuing the M.A.Sc degree in Canada, enabling me to address real-world optimization problems independently by designing fully functional controllers and conducting experiments to prove their feasibility.

I am also very grateful to have Dr. Liping Wang as my 1-year Co-op manager, who is highly energetic, persistent, and always glad to share and discuss the valuable engineering experience with me. This journey in industry pushed me to reflect on my career goals, my strengths, and it finally became one of the main motivations that encouraged me to pursue PhD program in the coming years. My achievements during my master program could not leave Liping's encouragement; he is my role model whom I aspire to emulate in my future career.

I would like to thank all my wonderful team members from RMAL: Zeyuan(Desmond) Peng, Zhiyang Gu, Yingying Li, Yin-chi(Andy) Chen, and Hamid Razmjooei. Particularly, Desmond and I started the M.A.Sc program at the same period, and we have experienced lots of impressive trips in Canada together. Yingying is my best gym bro who has guided me through the strength and aerobic training very nicely in the past full year.

Finally, I would like to thank all my families and friends for helping me and sharing so many unforgettable moments with me. Special appreciation to my parents, Chuanzhao Huang and Xiaoqin Que. I am so lucky to have them as my parents, who listen to me patiently, love and support me unconditionally, and stand by me at every stage of my growth. They always encourage me to treat people around sincerely and embrace the world bravely. I am so proud to have them with me.

Contents

List of Figures

List of Tables

Abbreviations

ANN	Artificial neural networks
ARC	Adaptive robust control
ARX	Autoregressive exogenous input
BITAE	Backward integral of time-weighted absolute error
CV	Charge valve
DAQ	Data acquisition
DC	Direct current
DPC	Direct pump control
DVMPC	Discrete-valued model predictive control
DVMPC3P	Discrete-valued model predictive control for DPC circuit
DVMPC3V	Discrete-valued model predictive control for VC circuit
EV	Exhaust valve
FP	Fitting percentage
GUI	Graphical user interface
ITAE	Integral of time-weighted absolute error
MAE	Mean absolute error
MAXAE	Maximum absolute value of the prediction error within the prediction horizon
MEANAE	Mean absolute value of the prediction error within the prediction horizon

MOS	Mean absolute valve of the overshoot
MPC	Model-predictive control
MSSE	Mean absolute valve of the steady state error
NC	Normally close
OOP	Objective-oriented programming
OS	Overshoot
PCVEC	Predicted charge valve energy consumption
PID	Proportional plus integral plus derivative
PPEC	Predicted pump energy consumption
PRBS	Pseudo-random binary signals
PTEC	Position tracking error cost
PVEC	Predicted valve energy consumption
PWM	Pulse-width modulation
QPPS	Quadrature pulses per second
RMSE	Root mean square error
RMSPE	Root mean square pressure error
RPM	Revolutions per minute
SDSSE	Standard deviation of the steady state error
SMC	Sliding mode control
SSE	Steady state error
VC	Valve control

Nomenclature

A_a , A_b	Cross-sectional areas of chamber A and chamber B
A_{rod}	Cross-sectional area of the cylinder rod
b	Critical pressure ratio
C_{choked}	Sonic conductance in choked flow
$C_{unchoked}$	Sonic conductance in unchoked flow
E_{cv}	Energy consumption of charge valves
E_p	Energy consumption of pumps
E_v	Energy consumption of valves
F_{dn}	Dynamic friction along the negative guide direction
F_{dp}	Dynamic friction along the positive guide direction
F_f	Friction force
$\hat{F}_f$	Predicted friction force
$F_{f,temp}$	Temporary friction force used for friction characterization tests
F_p	Pneumatic force
$\hat{F}_p$	Predicted pneumatic force
F_s	Static friction
J	Cost function
K	Specific heat ratio of air

L	Stroke length
M	Moving mass (including the piston, rod, carriage, and payload)
$\dot{m}_a$, $\dot{m}_b$	Mass flow rates into chamber A and B
$\dot{m}_1$, $\dot{m}_2$, $\dot{m}_3$, $\dot{m}_4$	Mass flow rates through the CV2, EV2, CV1 and EV2
$\dot{m}_t$	Mass flow rate though the air tank
$\dot{m}_{pA}$, $\dot{m}_{pB}$	Mass flow rate produced by the pump A and pump B
$\dot{m}_{pA}^*$, $\dot{m}_{pB}^*$	Scaled mass flow rate produced by the pump A and pump B
$\dot{m}_c$, $\dot{m}_d$	Mass flow rate through the charge valve and exhaust valve
M_1 , M_2 , M_3 , M_4 , M_5	Five operating modes used by the DVMPC
N_{delta}	Number of prediction steps included within each move
N_m	Number of moves used in DVMPC
N_p	Prediction horizon used in DVMPC
n_a , n_b	Motor speeds of pump A and pump B
n_a^* , n_b^*	Normalized motor speeds of pump A and pump B
$n_{\min}$, $n_{\max}$	Preset lower boundary and upper boundary for motor speed normalization
P_{atm}	Atmospheric pressure
P_a , P_b	Pressures in chamber A and chamber B

$\dot{P}_a$, $\dot{P}_b$	Pressure derivatives in chamber A and chamber B
P_a^* , P_b^*	Normalized pressures in chamber A and chamber B
$P_{\min}$, $P_{\max}$	Preset lower boundary and upper boundary for pressure normalization
P_t	Pressure in the air tank
$\dot{P}_t$	Pressure derivative in the air tank
p_1 , p_2	Upstream and downstream pressures of the orifice
p_a , p_b	Power consumptions of pump A and pump B
p_a^* , p_b^*	Normalized power consumptions of pump A and pump B
$p_{\min}$, $p_{\max}$	Preset lower boundary and upper boundary for power consumption normalization
P_{cv1} , P_{cv2} , P_{ev1} , P_{ev2}	Power rates of CV1, CV2, EV1, and EV2
$\hat{p}_{cv1}$, $\hat{p}_{cv2}$, $\hat{p}_{ev1}$, $\hat{p}_{ev1}$	Predicted power consumption of CV1, CV2, EV1, and EV2
R	Universal gas constant
S_p	Binary switch for the air tank pressure monitoring
T	Air temperature
T_s	Sample period
T_0	Room temperature
T_1	Upstream air temperature

t_i	Future sampling instant
t_k	Current sampling instant
U_{opt}	Optimized control sequence in DVMPC
u_a , u_b	Motor speed setpoints for pump A and pump B
u_1 , u_2 , u_3 , u_4	Pumps/valves control inputs
$\hat{u}_1$, $\hat{u}_2$, $\hat{u}_3$, $\hat{u}_4$	Predicted pumps/valves control inputs
V_{a0} , V_{b0}	Tube-related dead volumes of chamber A and chamber B
V_t	Volume of the air tank
$V_{\tan k}$	Volume of the air tank used in valve characterization tests
V_{t0}	Tube-related dead volume of the air tank
$W_{\dot{m}_t}$	Air tank mass flow rate working state
$\mathrm{W}_{\dot{\mathrm{P}}_\mathrm{t}}$	Air tank pressure derivative working state
y_{b0}	Maximum carriage displacement
y_{a0}	Minimum carriage displacement
y , $\dot{y}$, $\ddot{y}$	Position, velocity, and acceleration of the carriage
$\hat{y}$, $\hat{\dot{y}}$, $\hat{\ddot{y}}$	Predicted position, velocity, and acceleration of the carriage
ω_{bi} , ω_i , ω_v , ω_p , ω_{cv}	Cost function weighting coefficients used in DVMPC
ρ_0	Air density at room temperature

Chapter 1 – Introduction

1.1 Motivation of the research

Pneumatic actuators are reliable and durable. They are cost-effective; and inherently safer and friendlier to the environment than hydraulic actuators and electrical actuators employing rare earth magnets. They are widely used in industry, and also very popular in the wearable and soft robotics research fields. For example, soft pneumatic actuators are well suited to tasks that traditional rigid robots are poorly suited for, such as, picking fruit, wearable exoskeletons for enhancing human performance, and health care.

Although pneumatic actuation has the advantages mentioned above, the energy efficiency of pneumatic systems is relatively poor. The air compression process occupies a considerable amount of industrial energy consumption, and compressed air usually can not be fully utilized, since the problems of leakage and throttling loss are continuously occurring. The same problems also constrain the development of emerging applications of soft robots.

Hydraulic systems are closely related to pneumatic systems, and methods for improving their energy efficiency have been both studied and implemented commercially. Most hydraulic actuators are position controlled using a strategy known as "valve control (VC)". This strategy is typically implemented using a single pump, four-way servo valves and proportional directional valves. This produces precise position tracking performance, but since all of the flows are throttling controlled, a significant amount of energy is wasted as the fluid flows through the valve orifices. In contrast, the hydraulic systems based on the strategy known as "direct pump control (DPC)" have higher energy efficiency. With DPC, the displacement(s) of the pump(s) are controlled to provide the desired flows. Although due to the pump's large moment of inertia and the system nonlinearities, it is not possible to achieve the precise and quick actuator position control obtainable with VC, DPC avoids orifice losses as much as possible, which leads to its energy savings.

Unlike hydraulic systems, the DPC of pneumatic systems has received very little attention in academia or industry to date. Similarly, the application of advanced control methods, such as model-predictive control, to pneumatic actuator control with an emphasis on energy savings is a relatively unexplored research area. The need for energy savings with pneumatics actuators, and the lack of significant progress in this area, are the prime motivations for this thesis.

1.2 Objective and organization of the thesis

The objective of this thesis is to research model-predictive control (MPC) algorithms that provide energy savings without compromising actuator position control performance. These algorithms will be developed for VC and DPC pneumatic circuits and their performance will be experimentally verified. The subobjectives are listed below:

1. Study the latest literature on the modeling and energy saving position control of pneumatic systems and identify the research gaps.
2. Design the pneumatic circuits and build the test rigs required for acquiring the experimental data, including the electrical energy consumed.
3. Develop the nonlinear models of the system components and identify their parameters from the experimental data.
4. Develop the MPC algorithms for the VC and DPC circuits.
5. Define suitable performance metrics for the position control and energy consumption.
6. Study the effects of the MPC parameters on the performance metrics, and find the best parameter tunings for the VC and DPC circuits.
7. Objectively compare the experimental results.

The organization of the thesis is as follows. In Chapter 2, the state-of-the-art research in energy saving position control strategies for pneumatic system and pneumatic components mathematical modeling are reviewed. The nonlinear system model, including cylinder chamber dynamics, air tank dynamics, solenoid valve, air pump, friction of cylinder subsystem, and energy consumption model, is developed and experimentally validated in Chapter 3. In Chapter 4, the designs of the MPC algorithms for the DPC and VC circuits are proposed. Experimental results are reported and discussed in Chapter 5. The conclusions and achievements of the thesis research are summarised in Chapter 6, along with suggestions for future work.

Chapter 2 – Literature Review

2.1 Introduction

In this chapter, the state-of-the-art research in energy saving position control strategies for pneumatic systems, and in the mathematic modeling of pneumatic systems will be reviewed in Sections 2.2 and 2.3, respectively. A summary identifying the research gaps will be presented in Section 2.4 to conclude the chapter.

2.2 Energy saving position control strategies

2.2.1 Energy usage and general energy saving methods

Although pneumatic actuation is considered as a durable and low-cost drive method, it has been reported that up to 20% of energy consumption in industries is used for air compression and distribution, and around 40% of the compressed air is wasted at the various stages of a pneumatic system (Vittorini & Cipollone, 2016). The reasons include, but are not limited to: 1) leakage may happen at every connection and component in the loop like pipe joints, flanges, regulators, valves, etc.; 2) misuse of compressed air; 3) over-pressurization, e.g., operating all components at the mainline pressure; and 4) pressure drops in air distribution (piping losses, orifice losses). Based on this information, it is obvious that improving the energy efficiency of pneumatic systems is a critical issue for reducing their energy impact and carbon footprint.

Hepke & Weber (2013) summarized several energy saving measures that can be used with pneumatic actuators. During the design phase, based on the specific operating scenario, efforts should be made to select the proper working pressure, avoid oversizing the design, and instead choose each component properly. When operating the actuators (and machine they are being used with), these energy saving strategies could be implemented: 1) reducing the friction at each interface, 2) recovering or reusing the kinetic energy, exhaust air, and heat produced during the working process, and 3) designing the proper system configurations and develop the advanced controller to optimize the energy consumption. Regarding point 2, as an example, the exhaust air could be transformed into gravitational potential energy, or elastic potential energy, and this stored energy could be used in other applications.

In a pneumatic system, the energy source produces compressed air to support the working of actuators. Wehner et al. (2014) compared three pneumatic energy sources for autonomous and wearable soft robotics: microcompressors, tanks containing compressed gas, and direct chemical reactions. Battery-powered microcompressors are often considered as the best choice for low pressure, low flowrate applications, although their peak pressures and flowrates are inferior to the other energy sources, and microcompressors emit a large amount of noise. However, their drawbacks of low pressure and low flowrate can be compensated by arranging compressors in series or parallel, respectively. A tank of compressed gas is capable of providing high pressures and high flowrates stably, but flow through its regulator produces large throttling losses such that its energy density is worse than a battery-powered microcompressor. Direct chemical reactions include: monopropellant decomposition, hypergolic reaction, and combustion. With the highest net fuel energy density, they may be suitable for applications demanding extremely high power-density. Unfortunately, the reactions usually produce loud noises, high local temperatures and are very difficult to model. Compared with the first two sources, the research on direct chemical reactions still needs extensive development before it becomes practical.

Merkelbach et al. (2015) analyzed various methods for pneumatic system energy saving. The standard configuration used a 5/2 solenoid valve. The first energy-saving method was to shut off the pressure source at a certain position of the stroke using a 2/2 solenoid valve. The second method was to use a "crossflow" 2/2 solenoid valve that connected the two chambers of the actuator. The third method was to orient the cylinder vertically instead of horizontally. They calculated the exergy of the pressurized air rather than its energy. Their experiments showed that the "shut-off" strategy could save up to 20% exergy without much influence on the position dynamics behaviors, as long as no force is required at the end of the stroke. They also showed that crossflow strategy could reduce the exergy by 50% compared with the standard configuration. However, it also led to very slow actuator speeds due to the low driving force.

2.2.2 VC

VC of an actuator's position or pressure is widely used in conjunction with an accumulator, which is a tank of compressed air that is filled to the desired pressure by an air pump and pressure regulator. Various types of valves may be used, including 2/2, 3/2, 4/2 solenoid valves and proportional valves. These may be used either individually or in combination, depending on the cost limitations, control strategy, and the expected control performance. VC is popular in applications requiring precise position control. With a solenoid valve, the flowrate through the valve can be varied using pulse-width modulation (PWM), or it can be manipulated by optimizing the valve's ON/OFF time sequence. The latter method is known as "direct switching". With a proportional valve, the orifice can be varied continuously using an analog voltage input.

Al-Dakkan et al. (2006) proposed a dynamic constraint-based energy saving controller for a pneumatic position control system. They replaced a conventional 4/2 proportional valve with two 3/2 proportional valves. The system used sliding mode control (SMC) as a benchmark. They added a dynamic constraint that minimizes the chamber pressures to the SMC controller with the goal of providing energy savings. They charged a 5-gal air tank up to 90 psig, and the pressure drop during the test was regarded as the metric to evaluate the "energy" consumption. It must be noted that pressure drop is not a true measurement of energy consumption. The "energy" saving ratio on the two configurations ranged from 27% to 45% for the tracking sinusoidal desired trajectories with frequencies of 0.25 Hz -1.5 Hz. The peak saving ratio of 45% occurred with the 0.5 Hz desired trajectory. No specific position error data for quantitative comparisons were provided in the paper, so it is unclear if the "energy" savings was accompanied by worse position control performance.

Shen & Goldfarb (2007) proposed the idea of adding a 2/2 crossflow proportional valve to a standard 5/3 proportional valve controlled pneumatic actuator circuit to realize energy savings. The crossflow valve connecting the two chambers of cylinder allowed the recycling of pressurized air, and thus less air from the source was used. A SMC algorithm was designed to vary the orifice areas of the two valves for position tracking. Sinusoidal and step reference trajectories were tested. The mass of compressed air consumed from the source (obtained by integrating the output of a mass flowrate meter) was considered as the "energy" consumption. The experimental results for sinusoidal references (with frequencies from 0.25-1.5 Hz) demonstrated that the tracking performances with/without the crossflow valve were very similar. Using the crossflow valve eliminated the air required from the source during the initial 20-30% and final 20% of each working cycle, which led to "energy" savings from 25-52% in their experiments. The savings tended to decrease when the sinusoidal frequency was increased due to the orifice area of the crossflow valve becoming saturated.

Du et al. (2018) proposed an offline nonlinear dynamic optimization algorithm to improve the energy efficiency in pneumatic actuator open-loop position control. They used four 2/2 solenoid valves instead of the traditional 5/3 valve to control a double-acting cylinder for end-to-end motion. The ON/OFF time sequence of the four valves for a S-curve motion profile was obtained using the proposed algorithm. They used the standard volume of the air (obtained by integrating by the measured flowrate) to evaluate the "energy" consumption. Note that using the standard volume of air is not a true energy measurement. Their results showed that 50% - 62% of the compressed air was saved with different levels of air source pressure compared with the traditional circuit. However, they did not give the detailed information on the traditional circuit experiments, in which the consumed air kept increasing during the whole test. Even under the "energy" saving configuration, the inlet valve and exhaust valve connected to chamber A were both open at the start of some tests, which means there were still opportunities for further optimizing the valves ON/OFF sequence to save more "energy".

Qi et al. (2019) proposed a three-mode discrete-valued model-predictive controller (termed DVMPC2) for pneumatic actuator position control. The system configuration is similar to the one used by Du et al. (2018), but the ON/OFF states of the four solenoid valves were calculated online (i.e., at every sampling instant), using ~0.1 s prediction horizon. Several performance metrics including integral of time-weighted absolute error (ITAE), root mean square error (RMSE), overshoot (OS), steady-state error (SSE), and valve switches per second (SPS) were used to compare the proposed DVMPC2 and an advanced SMC algorithm. The ITAE, RMSE, OS, and SPS of DVMPC2 are 80%, 52%, 43%, and 20% lower than those of SMC. Although they included the SPS in the cost function to reduce the switching frequency for energy savings, no energy measurements or comparisons showing how much energy was conserved by this approach were included.

2.2.3 DPC

Pneumatic DPC has the potential to save energy compared with VC, but also has potential drawbacks. Achieving a fast position control is challenging due to the low bandwidth of most air pumps. In addition, it may not be possible to buy an air pump that matches the flowrate required for the target actuator(s). Probably for these reasons, very few researchers have attempted to apply DPC to the position control of pneumatic actuators. To the best of our knowledge, only two papers on this topic have appeared in the literature to date.

The first paper proposing the air DPC concept, and including controller design, was by Han & Toshiro (2003). They began by designing and fabricating their own miniature air pump with a maximum volume flowrate is 2.5 L/min and maximum output pressure of 120 kPa. Their pneumatic circuit consisted of this pump, a 2/2 solenoid valve connected to the atmosphere (to allow air to be released), and a single acting spring return cylinder with a 40 mm bore and a 48 mm stroke. They designed a modified PI control law to manipulate the duty cycles of the drive signals for the pump and solenoid valve in order to control the position of the cylinder's rod. The control law included the four modes: 1) if the position error was larger than 0.4 mm the pump ran at 100% duty cycle and the solenoid valve was closed; 2) if the error was between 0 and 0.4 mm, the valve was closed, and the PI law was used to calculate the pump's duty cycle over the range 0-32% duty cycle; 3) if the error was between −5 mm and 0, the PI law was used to calculate the valve's duty cycle over the range 22-46%; and 4) if the error was less than −5 mm, the valve was fully opened, and the pump was turned off. The desired trajectory consisted of a series of steps up to 45 mm. The results showed that the position did not reach steady state. Instead, the piston was able to stay within a ± 0.4 mm band around the desired steady state positions.

Du et al. (2017) proposed an energy saving circuit design for a pump-controlled pneumatic cylinder. The pneumatic circuit included an air compressor, a 5/2 solenoid valve, and the cylinder. The inlet and outlet of the air pump were connected to the two chambers of the cylinder. They mathematically modelled the system components. The pump's flowrate was modelled as a cubic function of its input voltage. They designed a fuzzy PID speed controller and conducted a series of end-to-end motion tests with two types of air pumps and three payload masses. The experimental results showed good robustness to payload mass variations. The standard volume of air, calculated from the measured flowrate from the air pump, was used to evaluate the "energy" consumption. Compared with the traditional valve-controlled circuit, the results suggest that the proposed scheme could save up to 75% of the "energy". Unfortunately, the paper does not provide inadequate information about the hardware used with their circuits, and no information about the hardware used for the traditional circuit.

In contrast, DPC is much more common in hydraulic applications, and researchers have compared the DPC with many other system configurations using diverse metrics to highlight the distinct advantages of using DPC. The most relevant paper is by Lyu et al. (2019). They compared the position control performance and energy efficiency of three different hydraulic circuits. The first circuit used DPC with a variable displacement pump. Two 2/2 solenoid valves with large orifices were arranged between the pump and each chamber of the cylinder, and two 4/3 proportional valves were controlled to release the fluid from the chambers. The adaptive robust control (ARC) law was implemented to calculate the desired flowrate through each chamber from the given desired position trajectory, then the corresponding flow distribution and inverse flowrate models were used to calculate the pump displacement and proportional valve controls. The second circuit used VC. A 6.3 L accumulator, preset to 2.5 MPa, was the hydraulic pressure source, and four 4/3 proportional valves were controlled to distribute the desired flowrate to realize cylinder position control. The third circuit was a combination of DPC and VC. The variable displacement pump was applied first to provide the majority of flow without throttling loss, then the valves, supported by the pressurized fluid from the accumulator, were precisely controlled to achieve the desired tracking performance. The desired position trajectory, lasting 30 s, was an S-curve from 0 m to 0.4 m, with the peak velocity of 0.15 m/s. The integration of the position error for these three circuits were 45.50 $\mathrm{mm \cdot s}$, 8.80 $\mathrm{mm \cdot s}$, and 9.00 $\text{mm}\cdot\text{s}$, and peak position error were 7.60 mm, 1.50 mm, and 1.40 mm, respectively. The energy consumption of the pump and valves were separately calculated by integrating the product of the pressure and volumetric flowrate from their circuits. As a result, the DPC circuit consumed 2.99 kJ energy, VC circuit consumed 11.69 kJ energy, while the hybrid circuit consumed 5.37 kJ energy (including 2.89 kJ from valves and 2.48 kJ from pump). For the energy efficiency comparison at the system level, it would be fairer to evaluate it using the system input energy, instead of the pump and/or valve output energy. Also, the participation of accumulator energy stored in advance (and later consumed), should be included to be more objective, and the gross energy consumption of the VC circuit should be evaluated in a long cycle test.

2.3 System modeling

The performance of MPC depends on the quality of the models it employs. For the position control of pneumatic actuators, the models of the solenoid valve, cylinder chamber dynamics, air pump, and the friction force are all important. The most relevant research will be reviewed in the following in this section.

2.3.1 Valve and cylinder chamber modeling

The ISO 6358 standard specifies the discharge and charge test used for determining the flowrate characteristics of compressed fluids flowing through a fixed or variable orifice. It was adopted to model solenoid valves in many papers (e.g., Harris et al. (2012), Doll et al. (2015)). The detailed model is presented below.

$$\dot{m} = \begin{cases} CP_1\rho_{ref}\sqrt{\dfrac{T_{ref}}{T_1}} & if \;\; \dfrac{P_2}{P_1} \le b \\ CP_1\rho_{ref}\sqrt{\dfrac{T_{ref}}{T_1}}\sqrt{1-\left(\dfrac{\dfrac{P_2}{P_1}-b}{1-b}\right)^2} & if \;\; \dfrac{P_2}{P_1} > b \end{cases} \tag{2.3.1}$$

where $\dot{m}$ is the mass flowrate through the orifice; P_1 and P_2 are the upstream pressure and downstream pressures, respectively; T_1 is the upstream air temperature; b is the pressure ratio; C is the sonic conductance; and ρ_{ref} and T_{ref} are the gas density and gas temperature at which the sonic conductance is measured.

As for the pressure and temperature evolution inside the cylinder chamber during the charging and discharging processes, it is generally accepted that the compressed air dynamics can be described by the following equations (Falcão Carneiro & De Almeida, (2006)):

$$\frac{dP}{dt} = -\gamma \frac{P}{V}\frac{dV}{dt} + \gamma \frac{R}{V}\dot{m}_{in} T_s - \gamma \frac{R}{V}\dot{m}_{out} T + \frac{(\gamma - 1)T}{PV}\dot{Q} \tag{2.3.2}$$

$$\frac{dT}{dt} = \frac{T}{V}\frac{dV}{dt}(1-\gamma) - \dot{m}_{out}\frac{RT^2}{PV}(\gamma - 1) + \dot{m}_{in}\frac{RT}{PV}(\gamma T_s - T) + \frac{(\gamma - 1)T}{PV}\dot{Q} \tag{2.3.3}$$

where P is the air pressure; γ is the specific heat ratio of the air, V is the volume of the chamber, $\dot{m}_{in}$ and $\dot{m}_{out}$ are the mass flowrate entering and leaving the chamber, respectively; T_s is the chamber inlet air temperature, which is usually assumed equal to the ambient temperature T_{amb}; and T is the air temperature inside the chamber. $\dot{Q}$ is the heat convection between the air inside of the chamber and the inner surface of the cylinder, which can be modeled by:

$$\dot{Q} = hS_h(y)(T_s - T) \tag{2.3.4}$$

where h is the heat transfer coefficient, and $S_h(y)$ is the heat transfer surface area related with piston position. Due to the much higher heat capacity of the cylinder material compared with the air, the temperature of the cylinder shell can be regarded as being equal to the ambient temperature.

Although (2.3.2) and (2.3.3) describe the air dynamics, the model simplification is still required in most practical applications. In some of previous work (Valdiero et al. (2011), Doll et al. (2015), Rouzbeh & Bone (2020)), the air temperature dynamics was ignored, and it was assumed that air temperature remained the same as the ambient temperature. In this case, (2.3.2) becomes:

$$\frac{dP}{dt} = -\gamma \frac{P}{V}\frac{dV}{dt} + \gamma \frac{R}{V} T_{amb} (\dot{m}_{in} - \dot{m}_{out}) \tag{2.3.5}$$

Another widely used strategy is to adopt the reduced-order thermodynamic models for the cylinder chamber (e.g., Meng et al. (2011), Harris et al., (2012), Rad & Hancu (2017)). They assumed the process inside of the chamber is polytropic ($PV^n = const.$). With this assumption, (2.3.2) and (2.3.3) can be simplified as shown below:

$$\frac{dP}{dt} = -\gamma \frac{P}{V}\frac{dV}{dt} + \gamma \frac{R}{V} \dot{m}_{in} T_s - \gamma \frac{R}{V} \dot{m}_{out} T + \frac{\gamma - 1}{V} h S_h(x)(T_s - T) \tag{2.3.6}$$

$$T = T_S \left(\frac{P}{P_s} \right)^{\frac{(n-1)}{n}} \tag{2.3.7}$$

where n is the polytropic index.

2.3.2 Air pump modeling

There are two types of air pumps: dynamic pumps and positive displacement pumps. A dynamic pump (e.g., centrifugal, axial, radial, etc.) transfers kinetic energy from the motor to the air using a spinning impeller, and then moves the accelerated air to the discharge port. They are widely used in low pressure, high flowrate applications for low viscosity fluids. A positive displacement pump sucks and traps a certain amount of air within a cavity which changes volume, and then forces it to the discharge port. It is selected to handle more difficult working conditions like high pressure applications with high viscosity fluids. Positive displacement pumps can be further categorized into reciprocating types (e.g., piston pumps and diaphragm pumps) and rotary types (e.g., vane pumps, screw pumps, and gear pumps).

Pérez-Segarra et al. (2003) summarized the three common approaches used to model gas pumps, which are also called “compressors”. The first approach evaluates the compressor's performance thermodynamically under cyclical conditions by means of global energy and mass balances. The second approach involves developing a more advanced simulation using conservation laws involving continuity, momentum, and energy. The third approach requires developing a detailed computational simulation of the flow in multidimensional and transient form. Its drawback is it typically requires a huge amount of computation resources and time. Using the second approach, the authors proposed a detailed hermetic reciprocating compressor model with mass conservation, linear momentum, and energy formulated for instantaneous local mean variables. The following input information is required: inlet and outlet pressure, inlet fluid temperature, compressor geometry, valve dynamic model analysis, electrical motor characteristic curve, ambient conditions, thermophysical properties database and empirical input provided by authors. Using AMD-K7 processors working at 900MHz, it took 3.63 hours to simulate a full cycle. The model was evaluated later by the experiments with different refrigerants and compressors with diverse displacements over a wide range of temperatures (Rigola et al. 2003). It accurately predicted the compressor’s performance. Unfortunately, this model takes too much computation time for it to applied in real-time control.

Hu et al. (2014) used a generic network modeling method for reciprocating compressors. The system was divided into its components, e.g., compression chamber, valve, shaft, motor, crankcase. Each component is treated as an independent process, then refrigerant flow, heat flow, and the power consumption relationships were used to connect the whole network. To improve the extension ability for simulating the compressor of arbitrary configuration and further-step system optimization, objective-oriented programming (OOP) method was applied to develop a graphical user interface (GUI) for compressor system modeling. The model was validated experimentally using a CO_2 two-stage compressor, and the deviations in mass flowrate and power consumption were mostly within $\pm 8\%$ and $\pm 5\%$.

Belman-Flores et al. (2015) proposed a reciprocating compressor model with artificial neural networks (ANN) method. The input variables include inlet pressure and temperature, outlet pressure, and compressor rotation speed. The output parameters are refrigerant mass flowrate, discharge temperature, and energy consumption. For comparison, they presented a physics-based model, in addition to those inputs used in ANN, compressor geometry parameters and thermodynamics properties are used for modeling. However, they did not consider the chamber geometry and friction, valve model, and refrigerant leakage in the model. Both models were validated experimentally with refrigerants R1234yf and R134a. They showed that the mean relative error is below 1% for ANN model, which is much better than physics-based model result (below 10%). The paper did not give the specific information on the time required for the ANN model calculations.

Tanveer & Bradshaw (2020) modeled the reciprocating compressor numerically. Their model involves the flow geometry, compression process and frictional losses. A series of sub-models such as heat transfer and reed valve dynamics were included in the compression process. The algorithm was implemented in both MATLAB and Modelica, and the results were compared with those using two existing compressor modeling platforms, PDSim and GT-Suite. The quantitative and qualitative criteria were implemented to provide insight on compressor modeling in terms of calculation friendliness, model troubleshooting difficulties, and potential for model development.

2.3.3 Friction modeling

Friction is a non-conservative force, the work done by friction is path dependent, and the process is highly related with tribology knowledge. These facts make friction a complicated physical phenomenon to model. For pneumatic cylinders, the friction force mainly comes from the piston seal and rod seal. Considering the additional moving components, the attached linear encoder or linear potentiometer used for position measuring, the linear bearing supporting the payload, and assembly misalignment errors will introduce additional friction forces, making the modeling even more complex and dependent on the specific application scenario. Most of the classical friction models used with pneumatic systems included static, Coulomb, and viscous components (e.g., Bone & Ning, 2007).

Rao & Bone (2008) adopted the classical friction model that includes the static friction, Coulomb friction, and viscous friction, plus the Stribeck effect. Several open-loop tests were conducted for a wide range of valve input signals and initial chamber pressures. The position and chamber pressures were measured to calculate the friction force, then a friction-velocity map was obtained and used to identify the parameters of the friction model using nonlinear least squares method. Yile & Bone (2015) extended the classical friction model by considering the pressure difference effect in addition to the effect of the velocity. The coefficient of determination, R^2, was used to evaluate the fitting performance of the model. They showed that the values of R^2 for friction along positive and negative direction were 0.87 and 0.8, much better than 0.44 and 0.49 calculated using the classical friction model.

Falcão Carneiro & De Almeida (2012) carried out research on pneumatic system modeling. In particular, they conducted a series of closed-loop tests with a simple P controller to collect the friction data. They found that when they modeled the friction as a function of velocity, the data was highly scattered and the Stribeck effect was hard to capture. As a result, they described the friction by a surface related with velocity and acceleration. A "friction artificial neural network" consisting of three layers involving 10, 6, and 1 *tansig* neurons, respectively, was used to predict the value of the friction force. A test dataset with 2500 samples randomly selected from the experiment was used to validate the model. The mean value of the error was 0.17 N and the standard deviation was 7.07 N.

Azzi et al. (2019) built an experimental test rig to characterize the friction of commercial pneumatic cylinders. With their rig, the piston and rod seals could be tested separately. They investigated seals with different geometries, including U-Cup seals, O-rings and X-seals. They found that under atmospheric pressure, the piston seal contributes ~25% of the total friction force, while this surged to ~90% when the chamber pressure was increased to 10 bar. The specific seal cross-section and diameter were both observed to have great effect on the friction. The U-Cup seals were found to be the most sensitive to the air pressure. The authors showed how the friction force changes over 1-10 bar pressure and 0-300 mm/s velocity ranges and concluded that the effect of pneumatic pressure on the friction was more significant than that of the velocity.

Jiménez et al. (2020) explained the method they used to measure the static friction. They used a short sampling period of 0.1ms to capture the value of the static friction. A 5/2 solenoid valve was employed between a double acting cylinder and pressure source. The valve was switched cyclically 45 times to cause the piston to move forwards and backwards repeatedly. At each cycle, the chamber pressures were collected at the instant when the piston started moving and were used to calculate the static friction force. They found there was slight difference in the static friction for the forward and backward directions. The friction became larger as the source pressure increased. For horizontal motions, the forward static force increased from 15.1 N to 27.1 N when source pressure was increased from 200 kPa to 500 kPa. The authors only analyzed the experimental results, and did not perform any modeling in this paper.

2.4 Summary

The state-of-the-art literature on energy saving position control for pneumatic systems and mathematical modeling of pneumatic systems were reviewed in this chapter.

Most of the previous works on pneumatic actuator position control employed a single air pump followed by an accumulator as the energy source and manipulated various valves with different control laws. As the literature shows, this VC method can produce precise position control performance, but its energy usage is typically ignored. VC mainly wastes energy due to the inefficient use of compressed air and throttling losses that occur with the valves. Methods using non-conventional pneumatic circuits (e.g., employing crossflow valves) and novel control laws have produced some savings, although the approaches to measure the system's energy have not been rigorous.

The alternative to VC is DPC. It uses a small-scale air pump to directly drive the chambers of the pneumatic actuator to avoid valve throttling losses. It is a more energy efficient strategy in theory, but the research on this topic is very limited, with only two papers appearing in the literature to date. Applying DPC to pneumatic systems is an underexplored research topic with significant potential for improving energy efficiency. With this in mind, MPC algorithms will be developed for VC and DPC pneumatic circuits in Chapter 4, and experimentally verified in Chapter 5.

The metrics used for evaluating pneumatic system energy consumption are another area in the literature that needs to be better addressed. Currently, most of the works used the volume of consumed air, or the supply pressure drop, as "energy" metrics. However, these metrics ignore the effect of temperature on the compressed air and do not truly measure energy. Measuring the mass flowrate of the compressed air is another option, but mass flowrate meters are usually very expensive, and this metric still does not measure energy. It is also incorrect to use corresponding valve/pump output energy to represent the system energy consumption, since that doesn't consider the efficiency of valve/pump themselves, which are also parts of an integrated system. For example, under the high-pressure working condition, the system input energy is larger due to lower pump volumetric efficiency (since the leakage increases with the pressure), but this part of the energy consumption is not considered by the previously mentioned energy metrics. Similarly, the accumulator must have been charged by the air pump before the start of each VC experiment so this energy consumption should be included. To address the above deficiencies, improved methods for predicting and measuring the system's energy consumption are proposed and implemented in Chapters 3-5.

For the pneumatic system modeling, the model for solenoid valves and cylinder dynamics are quite mature and they are already successfully employed in many high-performance control systems, but the air pump models suitable for controller implementation are lacking. The existing models are able to accurately predict the pump outputs, but they take too much computation to be utilized in real-time control algorithms. A model which can predict an air pump's mass flowrate under various working conditions with reasonable accuracy and a small computational cost is an unsolved problem that will be addressed in Chapter 3.

Regarding friction modeling, the friction of pneumatic cylinder is typically modeled as a function of velocity, sometimes with additional pressure term. However, for the low friction cylinder used in thesis these existing solutions were insufficient. It was necessary to develop novel solutions for the friction force data collection, analysis, and modeling, as will be shown in Chapter 3.

Chapter 3 - System Modeling

3.1 Introduction

The accuracy of the predictions calculated using the system model will play an important role in the performance of the MPC controller. The motion determined by Newton's second law requires the accurate prediction of pneumatic force and friction. The pneumatic force is determined by the cylinder geometry and air dynamics, in which the mass flowrate produced by the air pump under different working conditions and constrained by the valve orifice should be carefully modeled. The friction model also has a great impact on the final calculation of net force. For the energy saving objective, we also require mathematical models to predict the energy consumption during the MPC's decision making.

In Section 3.2, the proposed DPC and VC circuits, their operation, and the hardware used to implement them are described. The derivation of the cylinder and air tank dynamics models are given in Section 3.3. Next, in Section 3.4, the modeling of the charging valves and exhaust valves is elaborated. In Section 3.5, we present the characterization of the air pump, and its three sub-models: motor dynamics model, mass flowrate model, and energy consumption model. Finally, a new strategy for modeling cylinder's low friction force is introduced in Section 3.6. Each model is validated by experimental results. Please note that all pressures reported in this thesis are absolute pressures. Gauge pressure is not used.

3.2 DPC and VC pneumatic circuits

The DPC circuit used in this research is shown schematically in Figure 3.2.1. Each chamber of the cylinder is connected to an independent air pump (Hilitand, VN-C4, 40 L/min, with a built-in brush 12 VDC motor). To mount the ams-OSRAM AS5040 magnetic encoder for air pump's motor speed measurement, a small 3D printed ring was used to attach the disk magnet to the end of motor's back shaft; and a fixture was designed, and 3D printed to locate the encoder's circuit board properly. The detailed fixture arrangement is shown in Figure 3.2.2. The circuit in Figure 3.2.1 has

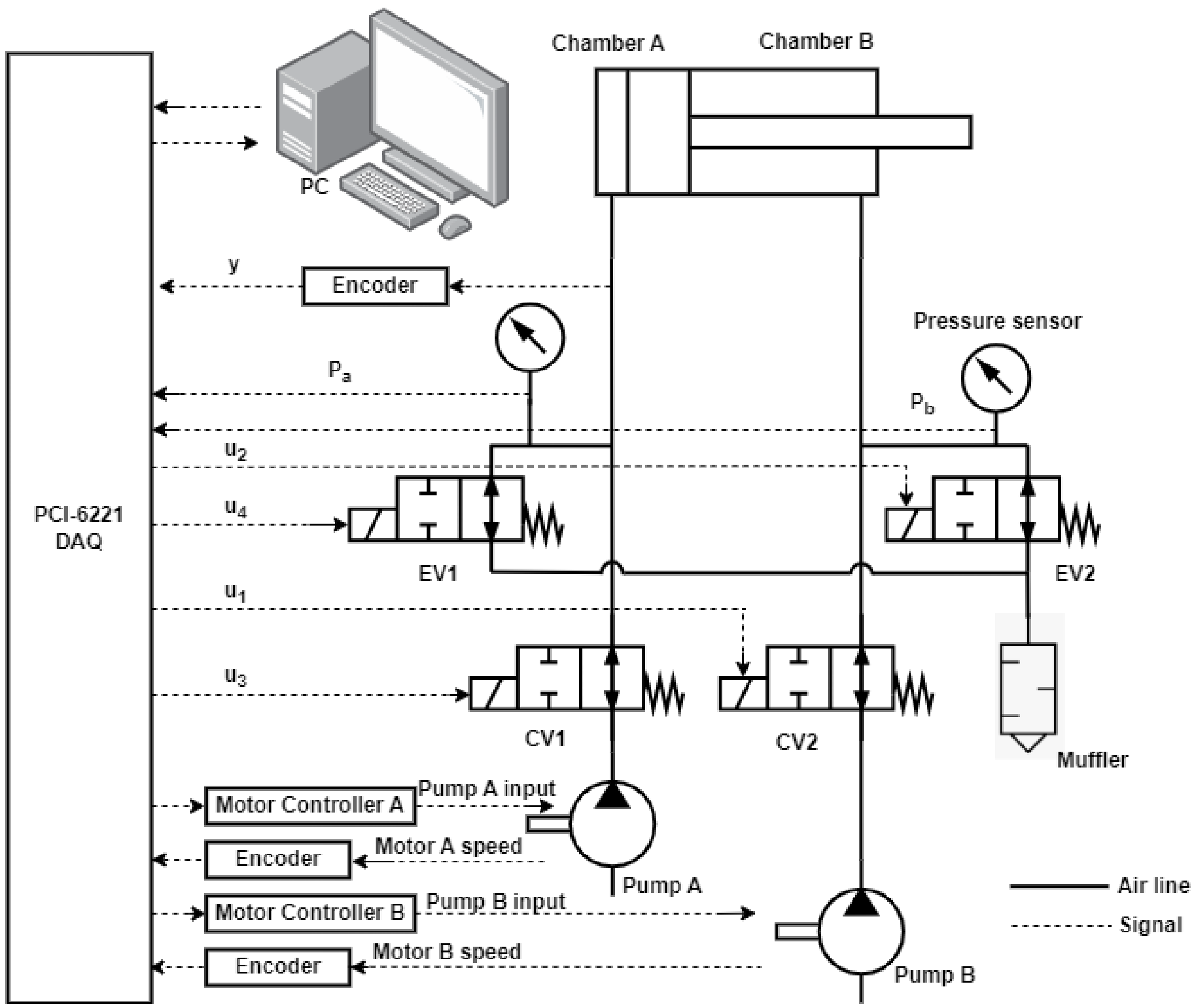

Figure 3.2.1 DPC schematic diagram.

the advantage of giving the MPC controller more control degrees-of-freedom than the single pump circuits used by Du et al., (2017), and Lyu et al., (2019), and the disadvantage of having to purchase an additional pump. The rodless chamber of the cylinder is named as chamber A, and its air source comes from pump A. Charging valve 1 (CV1), is synchronized with the working state of air pump, controls the charging from the pump and prevents extra air flow from the environment when the cylinder pressure is lower than atmospheric pressure. The exhaust valve 1 (EV1) controls the cylinder discharging to the atmosphere. There is a small muffler connected to the outlet of EV1 to reduce the exhaust noise. Similarly, the chamber containing the rod is named as chamber B, which is charged by pump B. Charging valve 2 (CV2) and exhaust valve 2

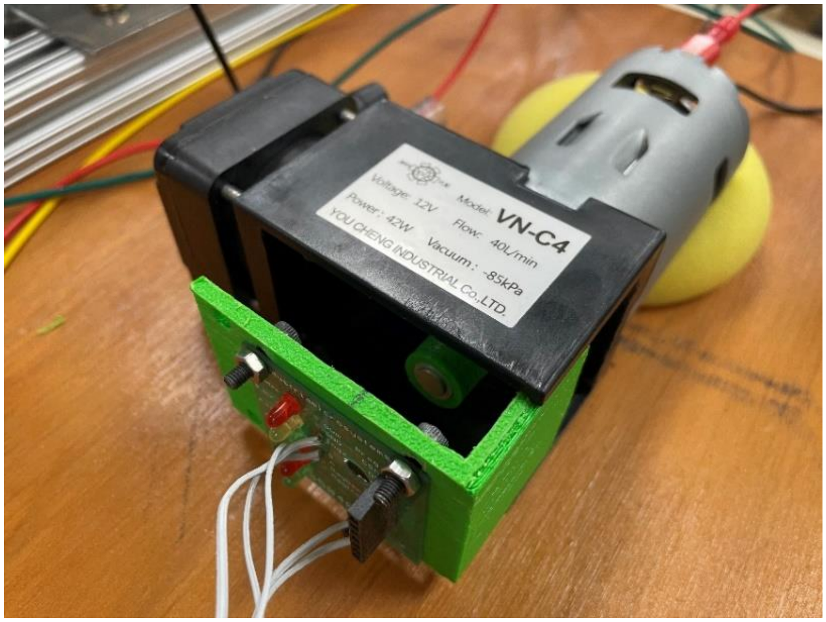

Figure 3.2.2 Fixture and ring made for mounting a AS5040 encoder's circuit board and disk magnet to each pump.

(EV2) controls the charging and discharging of the chamber B. All valves are MAC solenoid valves, model 34B-AAA-GDFB-1BA. They were converted from 3/2 NC valves to 2/2 NC valves by plugging their third ports. Their coils are driven by ODC5 24 VDC output modules. The valves were chosen since they produce high flowrates at low pressures, so their throttling losses are relatively small. Two pressure sensors (Honeywell, MLH100PGL01G), filtered by RC circuits with a 5 Hz cutoff frequency, are used to measure the chamber pressures. The two pump motors are speed-controlled by a Basicmicro RoboClaw 2x15A motor controller. The RoboClaw calculates the motor speed using the pulses from a magnetic encoder that was custom-mounted on its back shaft. The pump and valve currents are measured by Allegro MicroSystems ACS 714 and ACS 723 current sensors, respectively, whose outputs are also filtered by 5 Hz RC filters. The cylinder subsystem consists of a double acting pneumatic cylinder (Airpot, Airpel E24 D5.0N with a 0.945 inch bore size, and a full stroke of 5 inch), mounting base with a linear guide on it, and its carriage (plus a payload) coupled to the end of cylinder's rod. The maximum range of motion of the carriage is 0.12 m. A linear encoder (US Digital, EM2-0-2000-1 with a resolution of 0.003175 mm) is employed to measure the carriage's position. A NI PCI-6221 data acquisition card is used to obtain the sensor signals and send the control commands calculated by the MPC running on the PC to the two pumps and four valves. The PC has a 3.70 GHz Intel Xeon E5-1630 v3 processor and 16.00 GB RAM, running under 64-bit Windows 10 Pro. A 100 Hz sampling rate was used for all of the experiments. The experimental setup is shown in Figure 3.2.3.

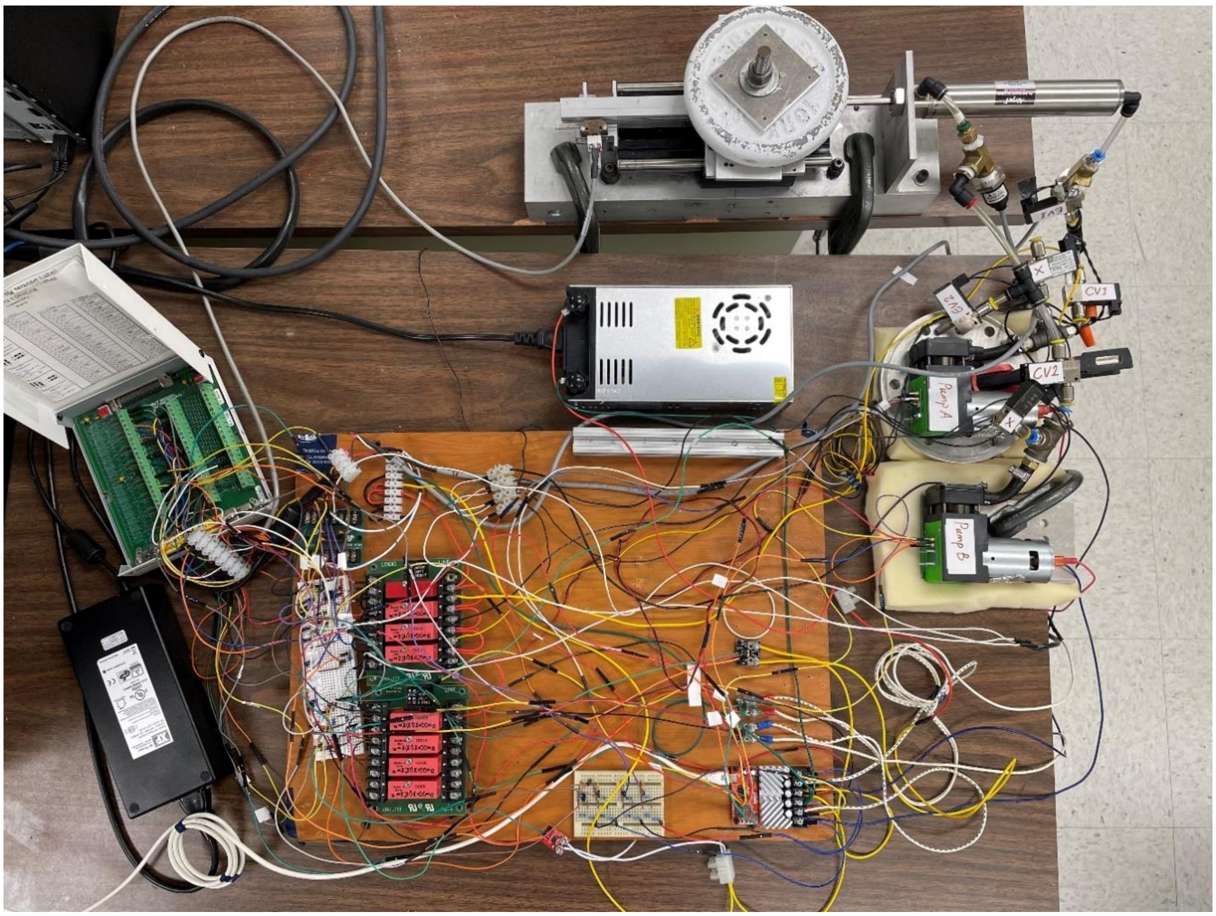

Figure 3.2.3 DPC experimental setup.

For the VC circuit, its air supply source is a tank filled with high-pressure air (Festo, CRVZS-2, with a 2 L volume), and the pump will only work to replenish the tank pressure when necessary. The tank's pressure is measured using a Honeywell MIPAN2XX100PSAAX pressure sensor with a 5 Hz RC filter. The other components are the same as those used with the DPC circuit. The VC circuit's schematic diagram is presented in Figure 3.2.4. The experimental setup is shown in Figure 3.2.5.

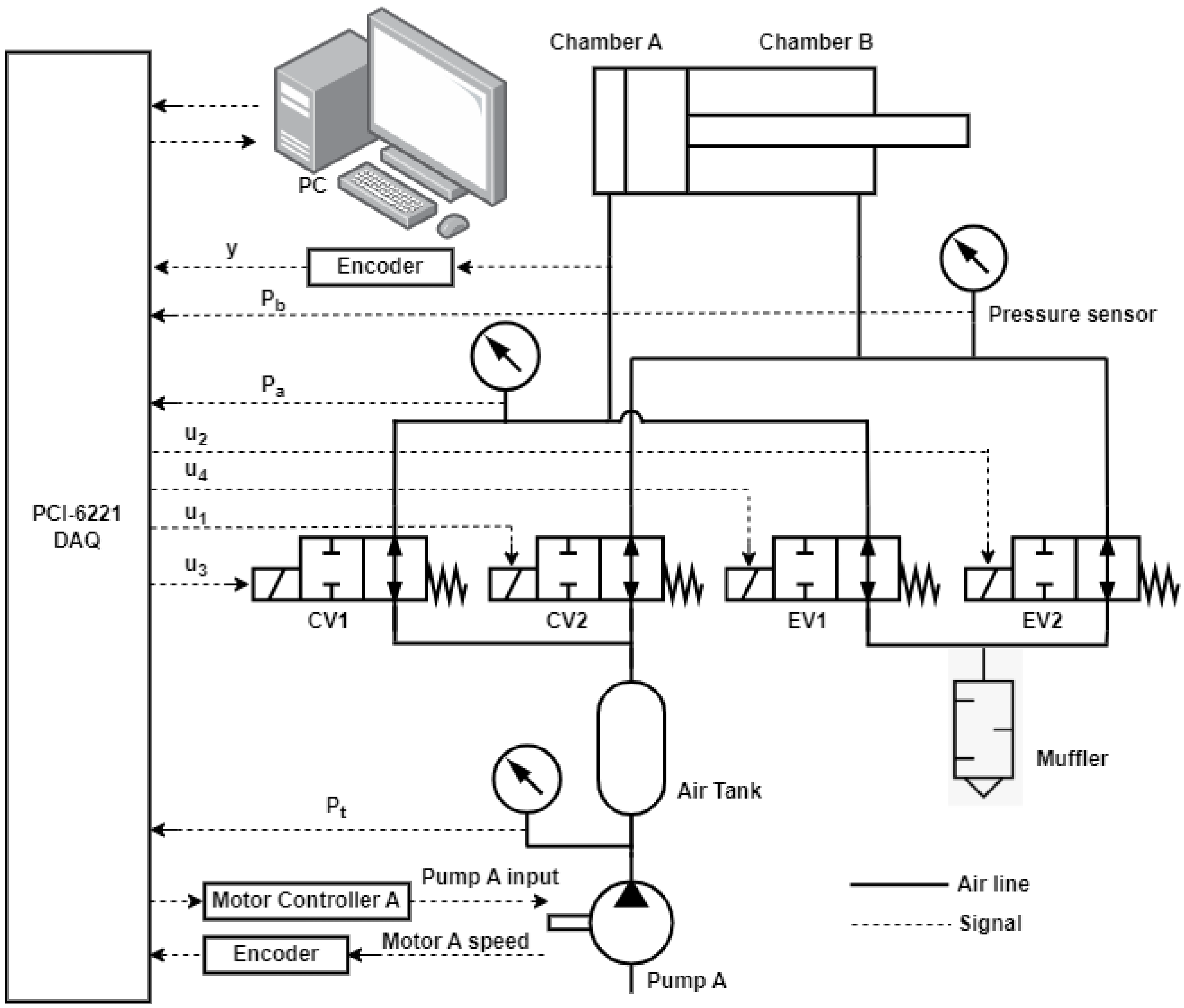

Figure 3.2.4 VC schematic diagram.

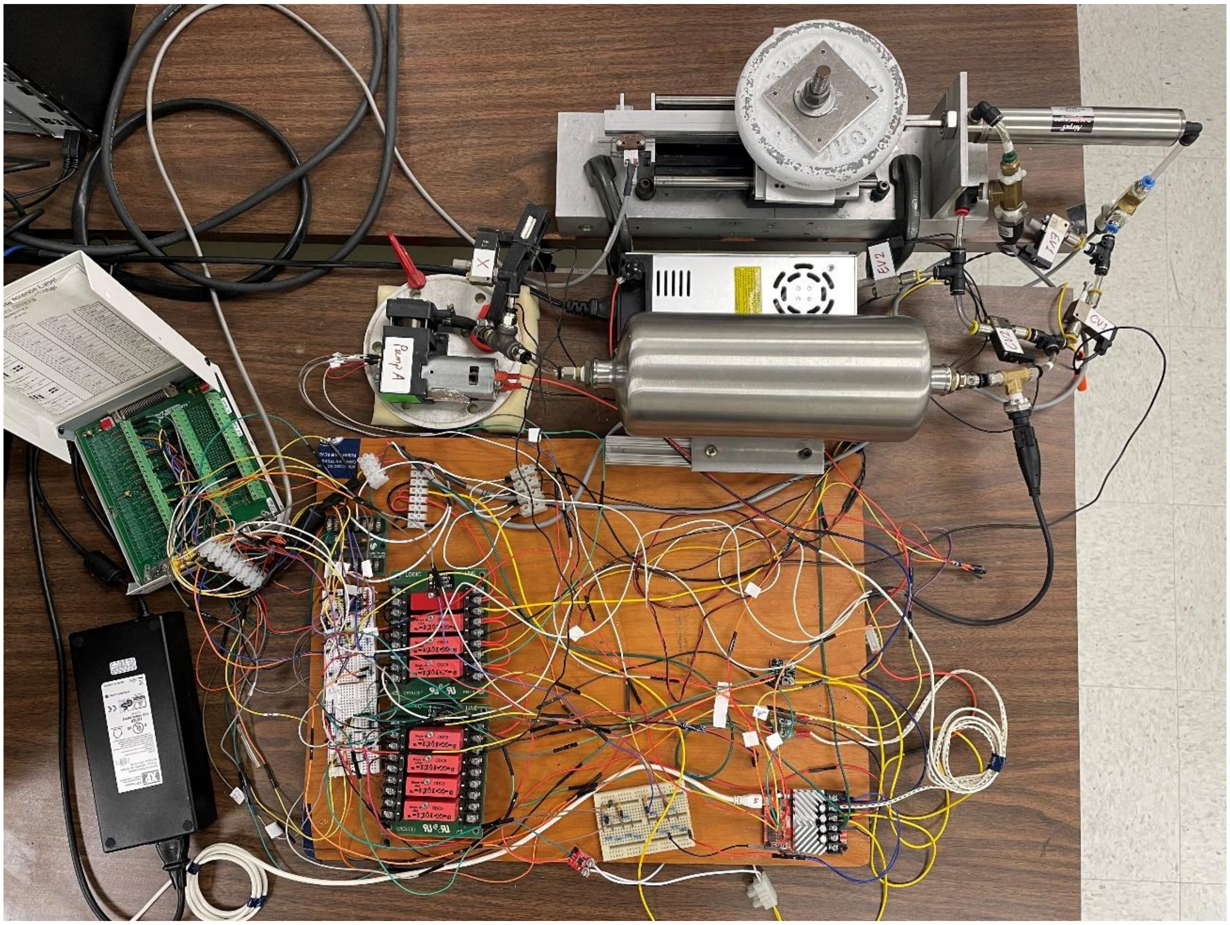

Figure 3.2.5 VC experimental setup.

3.3 Cylinder and air tank dynamics model

Considering the ideal gas law, conservation of mass, and conservation of energy for each chamber, the dynamic equations for chambers A and B of the cylinder are listed below (Rao & Bone (2008)):

$$KRT\dot{m}_a = KA_a\dot{y}P_a + (A_a y + V_{a0})\dot{P}_a \tag{3.3.1}$$

$$KRT\dot{m}_b = -KA_b\dot{y}P_b + (A_b(L-y) + V_{b0})\dot{P}_b \tag{3.3.2}$$

where K is the ratio of specific heat of air; R is the universal gas constant; T is absolute temperature of the air; A_a and A_b are the cross-sectional area of the two chambers; y and $\dot{y}$ are the carriage's displacement and velocity, respectively; P_a and P_b are the pressures of chambers A and B. $\dot{P}_a$ and $\dot{P}_b$ are the pressure derivatives of chamber A and chamber B respectively. The range of y is:

$$y_{a0} \le y \le y_{b0} \tag{3.3.3}$$

where y_{a0} is the minimum carriage displacement and y_{b0} is the maximum carriage displacement; L is the stroke length; and V_{a0} and V_{b0} are the tube-related dead volumes (including tubes and connectors) of the two chambers. Note that $y_{a0} > 0$ and $y_{b0} < L$. Lastly, $\dot{m}_a$ and $\dot{m}_b$ are the mass flow rate into the two chambers, that can be calculated by (3.3.4) and (3.3.5).

$$\dot{m}_a = \dot{m}_3 - \dot{m}_4 \tag{3.3.4}$$

$$\dot{m}_b = \dot{m}_1 - \dot{m}_2 \tag{3.3.5}$$

where $\dot{m}_1$, $\dot{m}_2$, $\dot{m}_3$, and $\dot{m}_4$ refer to the mass flowrate through CV2, EV2, CV1, and EV2, respectively. The modeling of the mass flowrates will be presented in the Sections 3.4 and 3.5 in detail.

By rearranging (3.3.1) and (3.3.2), the pressure derivatives of two chambers could be calculated as follows:

$$\dot{P}_a = \frac{KRT\dot{m}_a - KA_a\dot{y}P_a}{A_a y + V_{a0}} \tag{3.3.6}$$

$$\dot{P}_b = \frac{KRT\dot{m}_b + KA_b\dot{y}P_b}{A_b(L-y) + V_{b0}} \tag{3.3.7}$$

Lastly, based on the Newton's second law, we could get:

$$M\ddot{y} = P_a A_a - P_b A_b - P_{atm}(A_a - A_b) - F_f \tag{3.3.8}$$

where M is the moving mass (which includes the piston, rod, carriage and payload), $\ddot{y}$ is the payload acceleration, and F_f is the friction force, whose model will be introduced in the Section 3.6.

The dynamics modeling of air tank is derived based on (3.3.1) and (3.3.2). When the tank is charging chamber A or chamber B, the volume becomes a variable depends on the dynamics of connected chamber. The pressure derivative of tank is modelled as follows:

$$\dot{P}_{\mathrm{t}} = \begin{cases} \dfrac{KRT\dot{m}_t - KA_a\dot{y}P_a}{A_a y + V_{a0} + V_{\mathrm{t}} + V_{t0}} & if\ \mathrm{W}_{\dot{\mathrm{P}}_{\mathrm{t}}} = 1 \\ \dfrac{KRT\dot{m}_t + KA_b\dot{y}P_b}{A_b(L-y) + V_{b0} + V_{\mathrm{t}} + V_{t0}} & if\ \mathrm{W}_{\dot{\mathrm{P}}_{\mathrm{t}}} = 2 \\ \dfrac{KRT\dot{m}_t}{V_{\mathrm{t}} + V_{t0}} & if\ \mathrm{W}_{\dot{\mathrm{P}}_{\mathrm{t}}} = 3 \\ 0 & \text{else} \end{cases} \tag{3.3.9}$$

where $\dot{P}_t$ is the pressure derivative of air tank, V_t is the volume of air tank, V_{t0} is the tube-related dead volume (including tubes and connectors). $\mathrm{W}_{\dot{\mathrm{P}}_{\mathrm{t}}}$ is the tank pressure derivative working state: $\mathrm{W}_{\dot{\mathrm{P}}_{\mathrm{t}}} = 1$ stands for the situation whenever CV1 is powered, and the tank is charging the chamber A; $\mathrm{W}_{\dot{\mathrm{P}}_{\mathrm{t}}} = 2$ stands for the situation whenever CV2 is powered, and the tank is charging the chamber B; $\mathrm{W}_{\dot{\mathrm{P}}_{\mathrm{t}}} = 3$ stands for the situation when both CV1 and CV2 are unpowered, while air pump is replenishing the tank pressure. For the rest of situations, the pressure of air tank is constant, i.e., the pressure derivative is zero. $\dot{m}_t$ is the mass flow rate through the air tank, which could be modeled by the following equations:

$$\dot{m}_t = \begin{cases} -(\dot{m}_3 + \dot{m}_1) & if\ \ W_{\dot{m}_t} = 1 \\ \dot{m}_{pA} - (\dot{m}_3 + \dot{m}_1) & if\ \ W_{\dot{m}_t} = 2 \\ 0 & \text{else} \end{cases} \tag{3.3.10}$$

where $\dot{m}_{pA}$ is the mass flow rate provided by the air pump A during the replenishment, whose modeling will be elaborated in Section 3.5.4. $W_{\dot{m}_t}$ is the tank mass flow rate working state. $W_{\dot{m}_t} = 1$ means the air pump is not charging the tank, but the tank stored compressed air is consumed by CV1 or CV2; $W_{\dot{m}_t} = 2$ means the air pump is replenishing the tank pressure, while at the same time, CV 1 or CV 2 is powered for cylinder chambers charging. For the rest of situations, modelled zero mass flow rate means no air entering or leaving the air tank.

3.4 Valve model

3.4.1 Introduction

From Section 3.3, we know that accurate position prediction requires accurate mass flowrate predictions, so it is important to predict the exact mass flowrate through each solenoid valve's orifice. The ISO 6358 standard provides a detailed reference on the determination of flowrate characteristics of components using compressible fluids. It employs the following equation:

$$\dot{m} = \begin{cases} Cp_1\rho_{ref}\sqrt{\dfrac{T_{ref}}{T_1}} & if \ \dfrac{p_2}{p_1} \le b \\ Cp_1\rho_{ref}\sqrt{\dfrac{T_{ref}}{T_1}}\sqrt{1-\left(\dfrac{\dfrac{p_2}{p_1}-b}{1-b}\right)^2} & if \ \dfrac{p_2}{p_1} > b \end{cases} \tag{3.4.1}$$

where $\dot{m}$ is the mass flowrate through the orifice; p_1 and p_2 are the upstream and downstream pressures, respectively; b is the critical pressure ratio; C is the sonic conductance; and ρ_{ref} and T_{ref} are the gas density and gas temperature at which the sonic conductance is measured; T_1 is the upstream gas temperature.

The basic idea is to first determine the sonic conductance and pressure ratio, then (3.4.1) can be used to calculate the mass flowrate from the measured upstream and downstream pressure. To perform model fitting, it is necessary to know accurate values of the mass flowrate. However, it requires complicated and often expensive instruments to measure the gas mass flowrate. For example, the Hastings HFC-202 mass flowrate sensor used by Shen & Goldfarb (2007) costs over CAN$1600. A common and less expensive way to get the mass flowrate is to utilize (3.4.2), i.e., the equation derived by differentiating both sides of ideal gas law simultaneously with the volume constant, and transform the mass flowrate measurement into the pressure derivative calculation of a fixed volume of air container based on the original ISO 6358 model. It should be noted that for better fitting performance, we used separate sonic conductance values, C_{choked} and $C_{unchoked}$ for modeling the choked and unchoked flow regimes, respectively. Finally, the mass flowrate model for charging valve and exhaust valve can be written as (3.4.3) and (3.4.4).

$$\dot{m} = \frac{V_{\text{tank}}}{KRT_{ref}} \dot{p} \tag{3.4.2}$$

where V_{tank} is the volume of the air tank used in the experiment.

$$\dot{m}_c(p_1, p_2) = \begin{cases} C_{choked} p_1 \rho_0 \sqrt{\dfrac{T_0}{T_1}} & if \;\; \dfrac{p_2}{p_1} \le b \\ C_{unchoked} p_1 \rho_0 \sqrt{\dfrac{T_0}{T_1}} \sqrt{1 - \left(\dfrac{\dfrac{p_2}{p_1} - b}{1 - b} \right)^2} & if \;\; \dfrac{p_2}{p_1} > b \end{cases} \tag{3.4.3}$$

$$\dot{m}_d(p_1) = \begin{cases} C_{choked} p_1 \rho_0 \sqrt{\dfrac{T_0}{T_1}} & if \;\; \dfrac{p_{atm}}{p_1} \le b \\ C_{unchoked} p_1 \rho_0 \sqrt{\dfrac{T_0}{T_1}} \sqrt{1 - \left(\dfrac{\dfrac{p_{atm}}{p_1} - b}{1 - b} \right)^2} & if \;\; \dfrac{p_{atm}}{p_1} > b \end{cases} \tag{3.4.4}$$

where $\dot{m}_c$ is the mass flowrate through the charging valve, and $\dot{m}_d$ is the mass flowrate through the exhaust valve. ρ_0 is the gas density at room temperature. T_0 is the room temperature. C_{choked} is the sonic conductance in choked flow. $C_{unchoked}$ is the sonic conductance in unchoked flow.

3.4.2 Valve characterization testing

The schematic of the valve characterization test setup is shown in Figure 3.4.1, and the detailed components are listed in Table 3.4.1. The whole test includes three charging-exhausting cycles as shown in Figure 3.4.2: The air is provided from the central air source with a regulator, and we use air tank A between air source and charge valve to be characterized to maintain a more stable inlet pressure. The charge valve is closed at the beginning holding the pressure set at the regulator end, then the charge valve is ON while the exhaust valve is OFF in the following 15s. After that, the charge valve is OFF, and the exhaust valve connecting to the environment is ON to release the tank pressure in another 15s, during which the regulator is adjusted manually for the next cycle. In the real application, the charge valve inlet pressure depends on the air tank working pressure, so for modeling perspective, we select the first two cycles' pressure data for training and validate the modeling accuracy by the third cycle, whose inlet pressure is set between the first two cycles'. With respect to exhaust valve, we directly use the air tank B pressure data from the second cycle to train the model and use the data from the third cycle for model validation.

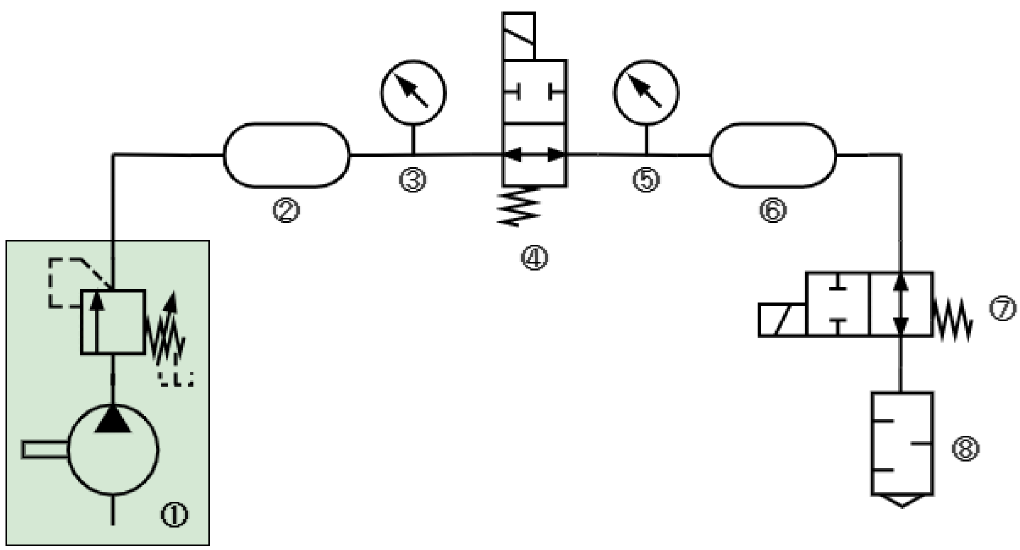

Figure 3.4.1 Schematic of the valve characterization test setup.

Table 3.4.1 Hardware used for the valve modeling test.

①	Central air source with regulator
②	Air tank A (2L)
③	Pressure sensor for air tank A
④	Inlet valve to be characterized
⑤	Pressure sensor for air tank B
⑥	Air tank B (574ml)
⑦	Exhaust valve to be characterized
⑧	Muffler

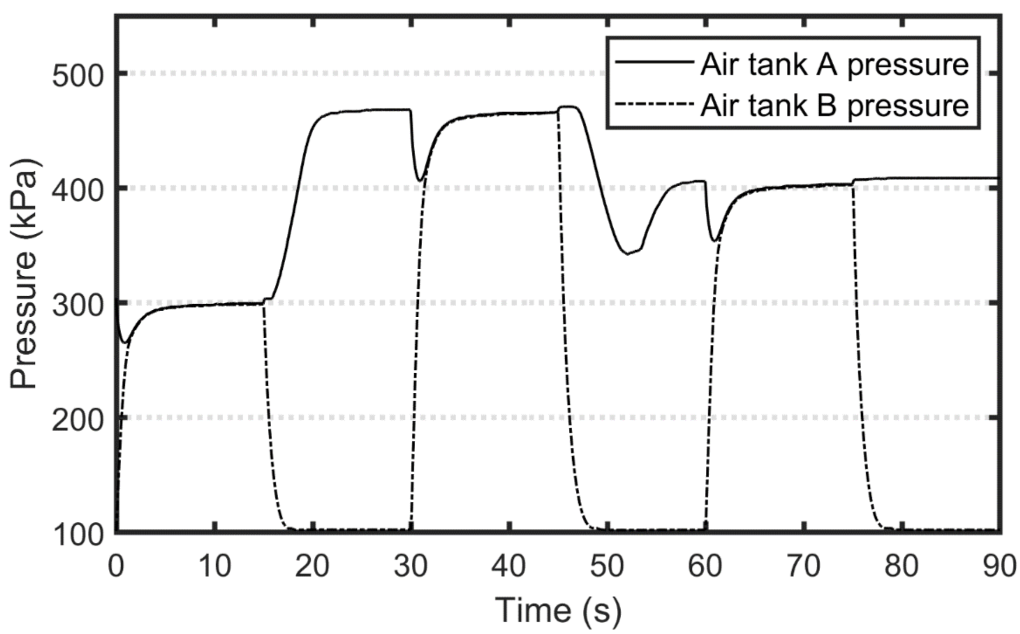

Figure 3.4.2 The charging-exhausting cycles used for the valve characterization test.

Two charge valves and two exhaust valves were characterized. The following fitting procedure was implemented in MATLAB:

1. Instead of assuming the theoretical *b* value of 0.54, candidate values for b are taken from the set (0.2, 0.21, … , 0.79, 0.8).
2. Select the first *b* value from the set.

3. Separate the data into choked and unchoked regions using the selected b value.
4. For this b value, and initial guesses of C_{choked} and $C_{unchoked}$, predict the tank pressures vs. time using (3.4.3) and (3.4.4).
5. Calculate the root mean square pressure error (RMSPE) between the measured and predicted pressures.
6. Use MATLAB's fminsearch optimization function with the RMSPE as the objective to be minimized to find the optimal values of C_{choked} and $C_{unchoked}$ for the selected b value.
7. Store the values of RMSPE, b, C_{choked} and $C_{unchoked}$.
8. If b = 0.8 then go to step 10.
9. Choose the next b value from the set, and repeat steps 3-8.
10. The fitted valve parameters are the stored values of b, C_{choked} and $C_{unchoked}$ that produced the smallest RMSPE.

The fitted valves' parameters are presented in Table 3.4.2. Comparisons of the experimental and simulated pressures for the validation data are plotted in Figures 3.4.3 - 3.4.6 for valves CV1, CV2, EV1 and EV2, respectively. Only minor errors may be observed between the predicted and measured pressures.

Table 3.4.2 Fitted valves' parameters.

	C_{choked} ($m^3/(s*Pa)$)	$C_{unchoked}$ ($m^3/(s*Pa)$)	b	RMSPE for training set (kPa)	RMSPE for validation set (kPa)
CV1	2.64×10^{-9}	2.34×10^{-9}	0.50	2.26	2.43
CV2	2.87×10^{-9}	2.57×10^{-9}	0.50	1.50	1.86
EV1	3.35×10^{-9}	2.00×10^{-9}	0.54	2.34	2.37
EV2	2.93×10^{-9}	1.77×10^{-9}	0.52	2.42	2.71

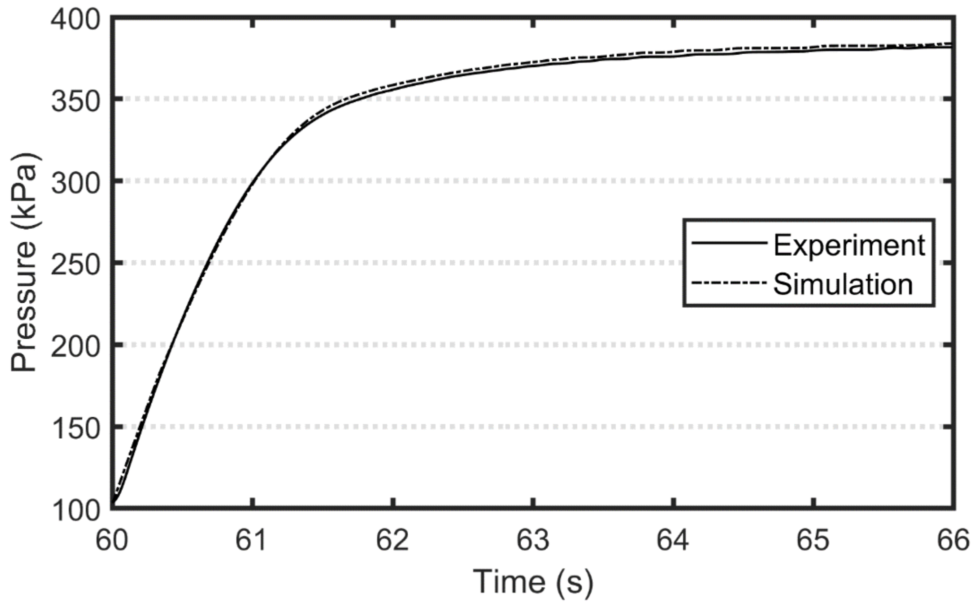

Figure 3.4.3 Comparison of CV1 experimental and simulated charging pressures for the validation data.

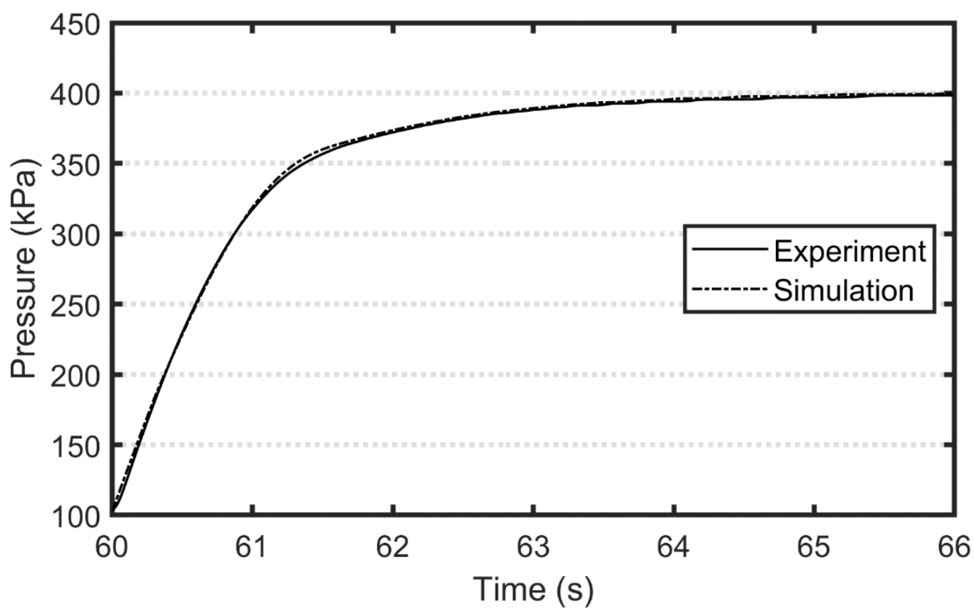

Figure 3.4.4 Comparison of CV2 experimental and simulated charging pressures for the validation data.

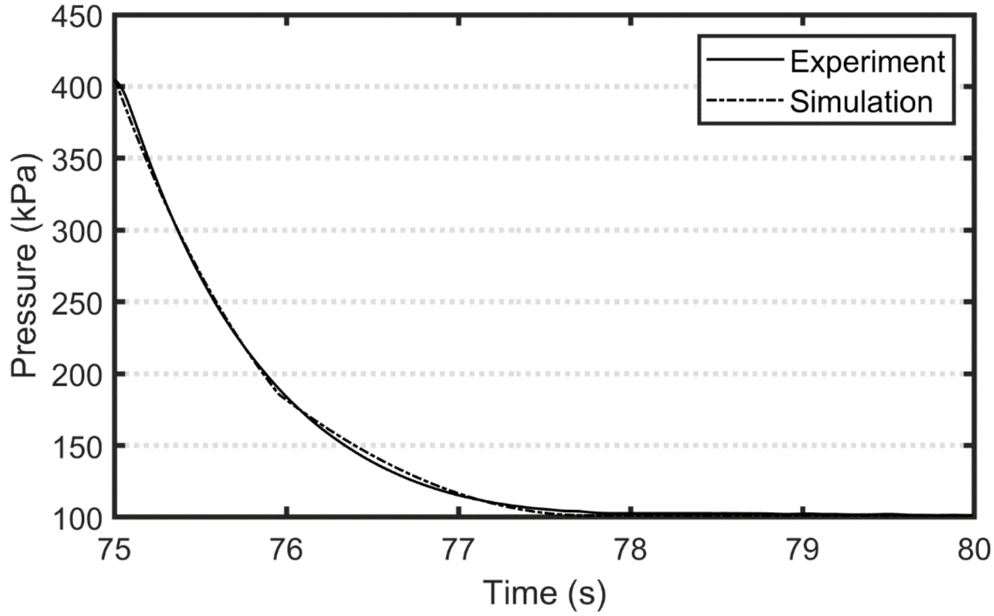

Figure 3.4.5 Comparison of EV1 experimental and simulated exhausting pressures for the validation data.

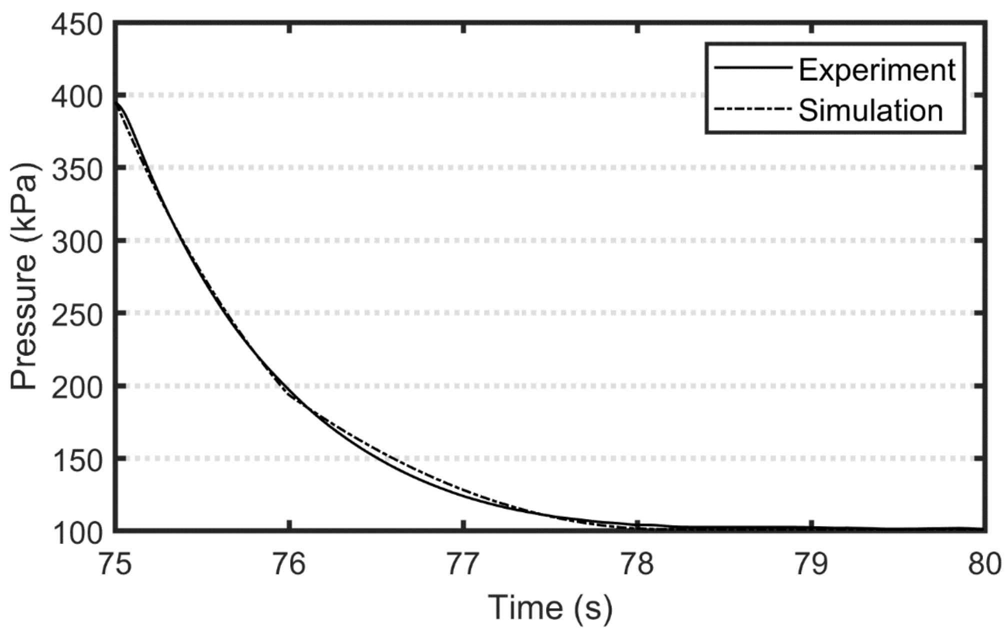

Figure 3.4.6 Comparison of EV2 experimental and simulated exhausting pressures for the validation data.

For valve energy consumption modeling, due to the effect of coil inductance, the real current does not change instantly when the voltage is applied to its coil, and its dynamics cannot be neglected. From valve step response testing, we found the time constant of the valve's current is about 30 ms. The corresponding first order difference equation (3.4.5) was used to simulate the real energy consumption. The power consumption for each valve measured at the steady state is listed at the Table 3.4.3.

Table 3.4.3 Solenoid valves' measured powers at steady state.

P_{cv1}	2.88 W
P_{cv2}	4.56 W
P_{ev1}	2.88 W
P_{ev2}	2.64 W

$$\hat{p}_i(t_k) = 0.72\ \hat{p}_i(t_k - T_s) + 0.28\ P_i(t_k),\ i \in \{\ cv1,\ cv2,\ ev1,\ ev2\ \} \tag{3.4.5}$$

where $\hat{p}_i$ is the estimated power consumption, P_i is solenoid valve's power rate at steady state, t_k is the current instant, and T_s is the sampling period.

The four valves were connected in parallel in the electrical circuit. A series of digital signals from the NI PCI-6221 were sent to the ODC5 output modules, thereby controlling the switching of each valve. A current sensor was employed to measure the consumed current in the circuit during the experiment. The energy consumptions of valves' circuit, E_v, and the energy consumption of charge valves, E_{cv}, for the kth sampling period can be approximated using Euler integration as follows:

$$E_v(t_k) = (\hat{p}_{cv1}(t_k) + \hat{p}_{cv2}(t_k) + \hat{p}_{ev1}(t_k) + \hat{p}_{ev2}(t_k)) \cdot T_s \tag{3.4.6}$$

$$E_{cv}(t_k) = (\hat{p}_{cv1}(t_k) + \hat{p}_{cv2}(t_k)) \cdot T_s \tag{3.4.7}$$

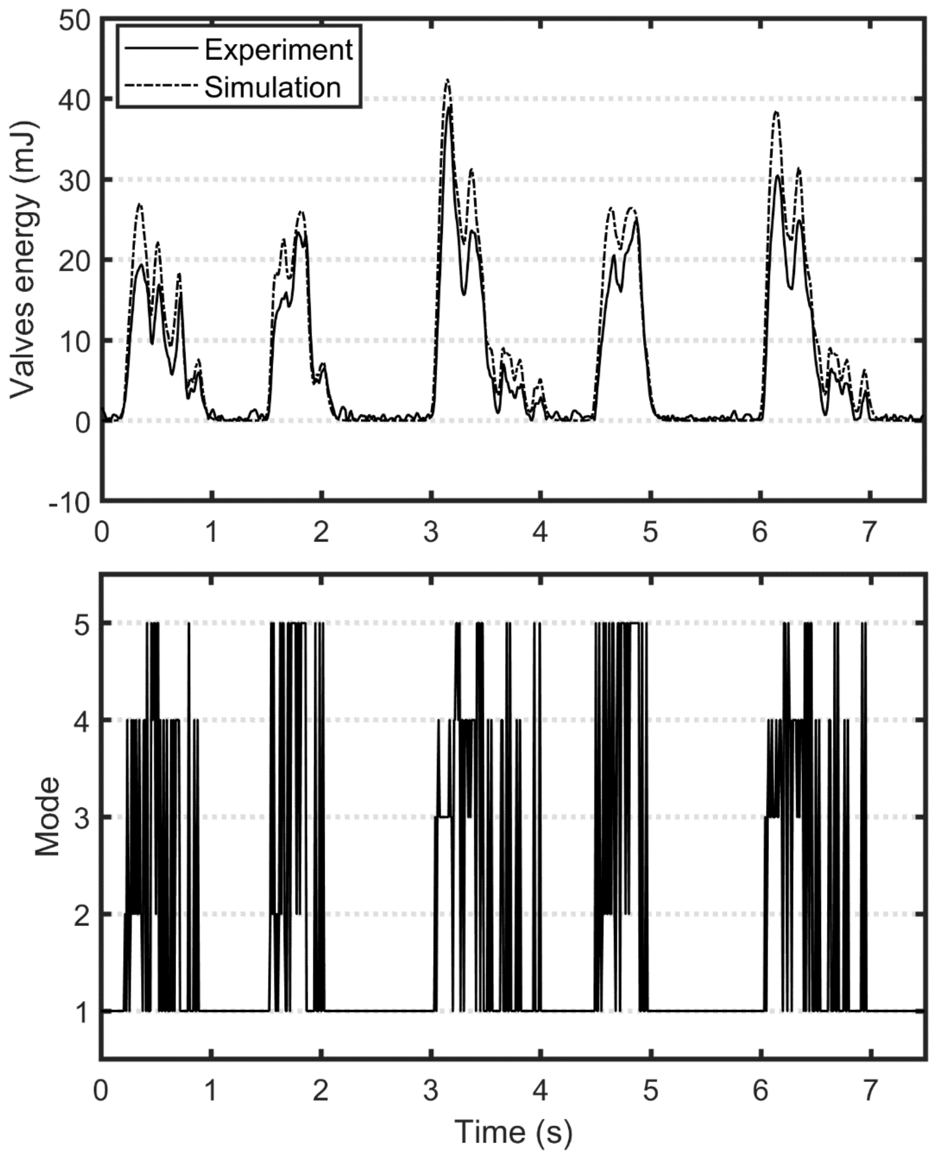

Figure 3.4.7 Comparison of the valves' experimental and simulated energy consumptions.

To validate the model, we use the actual control actions from the experiment as inputs to the simulation to simulate the valves' circuit energy consumption, and then compare it with the measured results. From Figure 3.4.7, the simulation results are close to the experimental data, and reflect the general trend well.

3.5 Pump model

3.5.1 Introduction

An air pump (also known as an "air compressor") converts low pressure input air into higher pressure output air. It mainly contains two parts, an electrical motor, and a mechanical air compression device. The VN-C4 positive-displacement air pump used for this research contains a brushed DC motor and a piston pump.

Figure 3.5.1 VN-C4 reciprocating piston air pump used in this research.

As previously stated, accurate position prediction relies on accurate mass flowrate prediction, so it is important to predict the exact mass flowrate produced by air pump in a variety of working conditions. The mass flowrate produced by air pump is determined by several factors in terms of mechanical compression principles: the dimension and stroke length of the piston, the leakage situation, the number of strokes per second (which is proportional to the motor speed), and the pump's outlet pressure. For a commercial product, the piston dimension and stroke have already been defined, which means the pump displacement value could be considered as a constant value. Considering the working principle of pump, the sealing on the piston plays an important role: the better sealing, the higher volumetric efficiency, however, it also brings larger friction. The main load on the motor is due to air pressure on the piston and the friction force of the piston seals, the larger friction will obviously degrade the pump performance under high pressure working condition, and it finally leads to motor stalling. Actually, the designers will usually consider setting a proper gap tolerance between piston sealing diameter and compression chamber tube inner diameter to keep a good balance between sealing and leakage. Because of the manufacturing tolerances, the leakage situation differs from pump to pump, which means the pump modeling should be based on the independent testing results. On the other hand, although when the outlet pressure is constant, the higher motor speed, the more compressed air, when the motor speed is constant, the mass flowrate doesn't show linear relationship with the outlet pressure, because the higher outlet pressure will also create greater leakage, i.e., lower volumetric efficiency. In view of the complexity of the leakage modeling, volumetric efficiency and mechanical efficiency calibration under different working conditions, it is easier to model the pump as a grey box, which calculates the mass flowrate as a function of motor speed and outlet pressure.

The RoboClaw 2x15A is the synchronous regenerative brushed DC motor controller used in this research. It can drive both pump motors at the same time, and is equipped with several control modes including RC control, analog control, standard serial control, and packet serial control used for different applications. Its analog control mode was used in the characterization tests to change the pump motors' speed setpoints. The input voltage for the speed setpoint signal ranges from 0 to 2V. A 1V setpoint signal means the desired speed is zero, and a 2V setpoint signal will push the motor to reach its maximum speed. Two sets of important RoboClaw parameters are its quadrature pulses per second (QPPS) and its speed control PID parameters. A QPPS of 80000 was defined to limit the max speed motor could reach, which is around 4700 RPM. However, during this research, it was found that the relationship between the 1-2 V speed setpoint signal and the resulting output motor speed is nonlinear. A fixed voltage of 1.5 V was used to drive the motor to keep it running at 4300 PRM. The PID parameters were manually tuned to: $K_p = 0.3$, $K_i = 0.2$, and $K_d = 0$. The pump characterization testing will be described in Section 3.6.2, and its sub-models (i.e., motor dynamics autoregressive exogenous input (ARX) model, pump mass flowrate model and pump energy consumption model) will be identified and validated using experimental data in Sections 3.6.3 to 3.6.5, respectively.

3.5.2 Pump characterization testing

The schematic of the pump characterization test setup and the actual hardware setup are shown in Figures 3.5.2 and 3.5.3, respectively. The two pumps were tested separately. The detailed components are listed in Table 3.5.1. The air pump was connected to a 2 L air tank, and the tank pressure was measured over the duration of the test. The same methodology as in Section 3.4.1 was used to transform the pressure derivative into mass flowrate data. During each test, a series of pseudo-random binary signals (PRBS) switching the motor's setpoint speed from 0 to 4300 RPM were sent to the RoboClaw to make the pump charge the tank intermittently. The maximum pulse length of 1.5 s was chosen to better capture the motor's dynamic response.

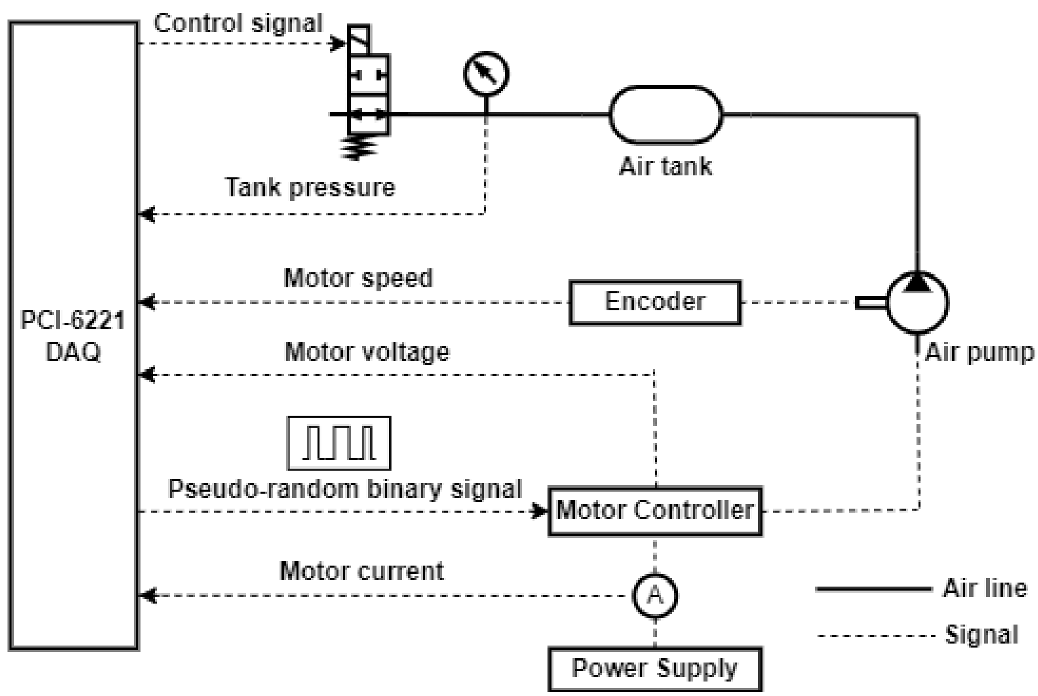

Figure 3.5.2 Schematic of the pump characterization test setup.

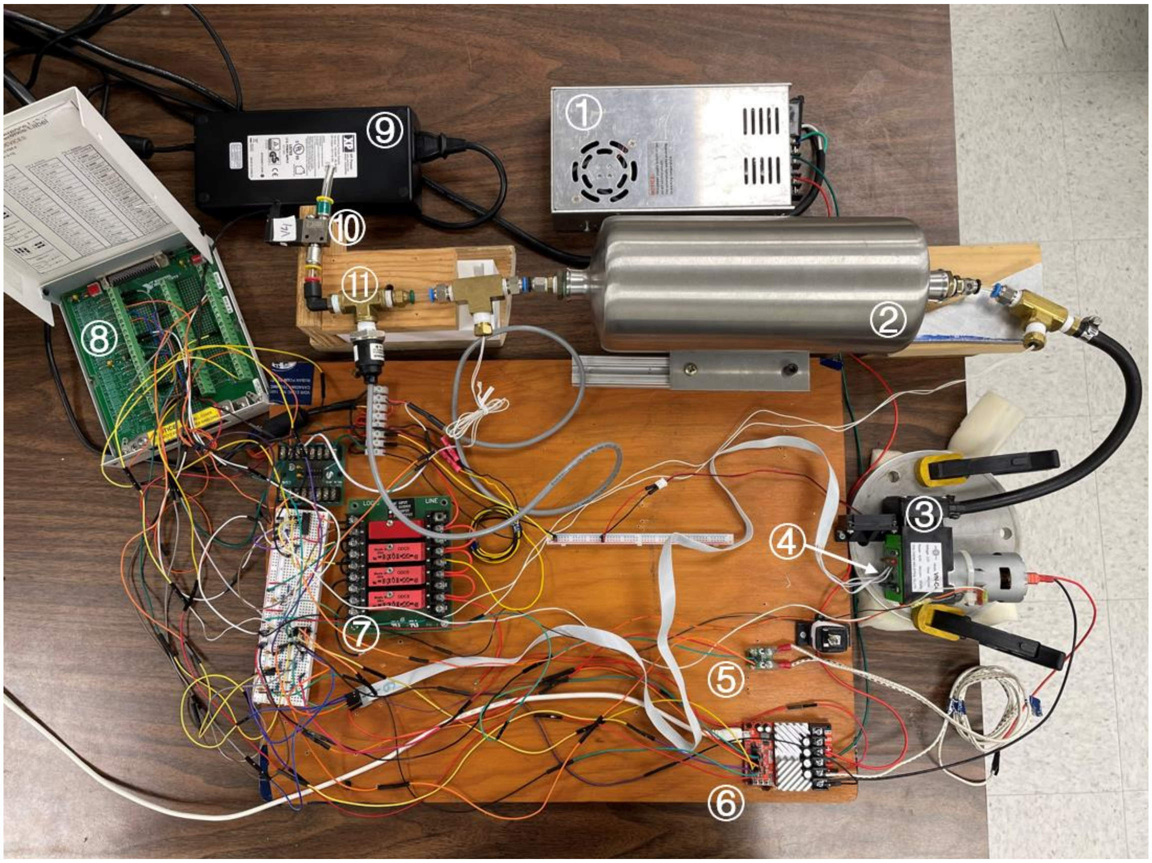

Figure 3.5.3 Pump characterization hardware setup.

Table 3.5.1 Hardware used for pump characterization.

①	24V power supply
②	Air tank
③	VN-C4 air pump
④	Magnetic rotary encoder
⑤	Current sensor
⑥	RoboClaw motor controller
⑦	DC output modules
⑧	DAQ device
⑨	24V power supply
⑩	Solenoid valve
⑪	Pressure sensor

Due to differences in the air pumps' manufacture, pump A took around 70 s to charge the tank to 450 kPa, while pump B took around 90 s to reach this pressure. It was also found that at around 100 s, motor stall happened at 530 kPa for pump A, and at 480 kPa for pump B. These pressures were regarded as the working limits of these air pumps. To avoid the stall condition, only the first 80 s of the pressure data were used to identify the models. The characterization test results for pumps A and B are plotted in Figures 3.5.4 and 3.5.5, respectively. The slower mass flowrate of pump B may be observed by comparing the two pressure plots.

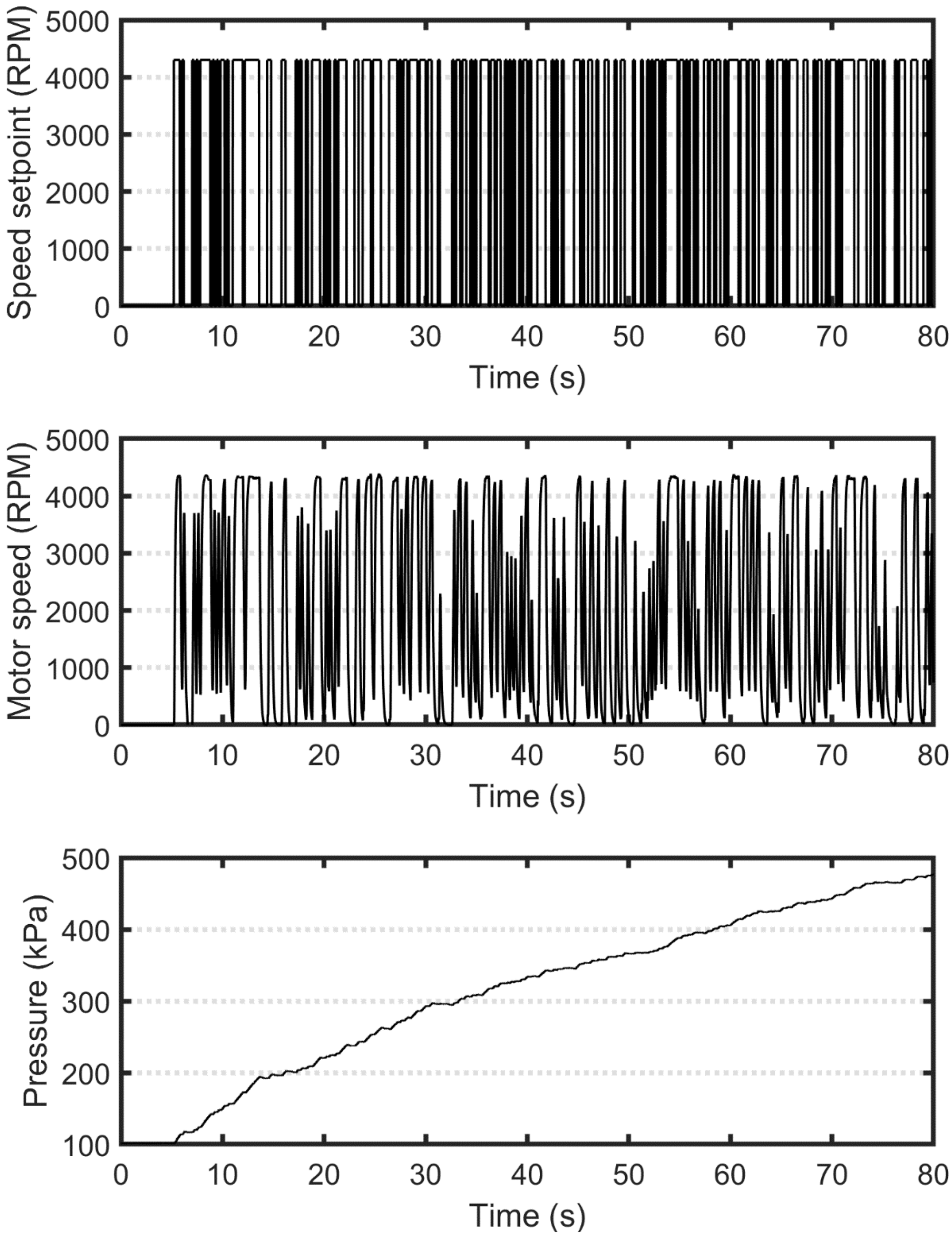

Figure 3.5.4 Characterization test results for pump A.

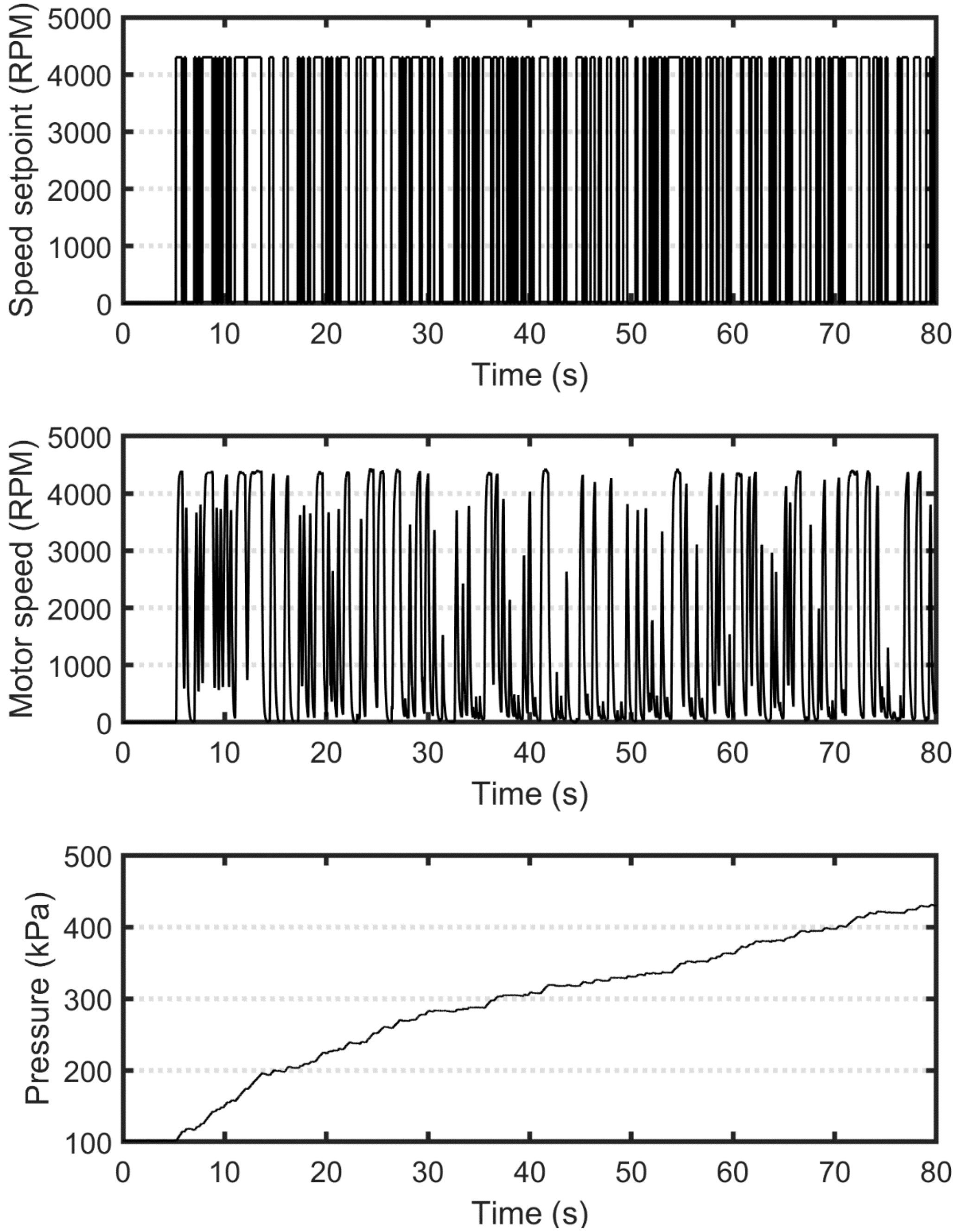

Figure 3.5.5 Characterization test results for pump B.

3.5.3 Motor dynamics ARX model

An autoregressive exogenous input (ARX) model is a combination of an autoregressive model and an exogenous input model. It is a linear representation of a dynamic system in discrete time and can be represented by the following equation:

$$y(t_k) = -a_1 y(t_k - T_s) - \ldots - a_n y(k - nT_s) + b_0 u(t_k - dT_s) + \ldots + b_m u(t_k - (d+m)T_s) \quad (3.5.1)$$

where $y(t_k)$ is the model output at the current sampling instant t_k; $y(t_k - T_s), \ldots y(t_k - nT_s)$ are the past values of the time series; and $u(t_k - dT_s) + \ldots + u(t_k - (d+m)T_s)$ are the exogenous input variables from before the delay period dT_s.

The motivation of the motor dynamics characterization is to model the motor's speed response to a known motor speed setpoint. This requires determining the model's structure (i.e., orders *n* and *m*; and delay *d*) and parameters (i.e., the values of the a's and b's in (3.5.1)). MATLAB's arx function was used to identify the models' structure and parameters. For both pumps, the best orders for autoregressive terms, exogenous signal terms and delay were determined to be 2, 1, and 2, respectively. The motor dynamics ARX model for pump A and pump B are given by:

$$\begin{aligned} n_a(t_k) &= f_{arxa}(n_a(t_k - T_s), n_a(t_k - 2T_s), u_a(t_k - 2T_s)) \\ &= 1.7770 n_a(t_k - T_s) - 0.7913 n_a(t_k - 2T_s) + 0.0143 u_a(t_k - 2T_s) \end{aligned} \quad (3.5.2)$$

$$\begin{aligned} n_b(t_k) &= f_{arxb}(n_b(t_k - T_s), n_b(t_k - 2T_s), u_b(t_k - 2T_s)) \\ &= 1.7790 n_b(t_k - T_s) - 0.7994 n_b(t_k - 2T_s) + 0.0204 u_b(t_k - 2T_s) \end{aligned} \quad (3.5.3)$$

$$u_a(t_k) = \begin{cases} 0 & if \;\; M(t_k) \in M_i, \;\forall\; i = 1,\ 3,\ 4,\ 5 \\ 4300 & if \;\; M(t_k) = M_2 \end{cases} \quad (3.5.4)$$

$$u_b(t_k) = \begin{cases} 0 & if \;\; M(t_k) \in M_i, \;\forall\; i = 1,\ 2,\ 4,\ 5 \\ 4300 & if \;\; M(t_k) = M_3 \end{cases} \quad (3.5.5)$$

where the n_a, and n_b are the pump A and pump B motor speeds in RPM, respectively; and u_a and u_b are the speed setpoints (in RPM) for their models. $M_1 \sim M_5$ are the five operating modes used by the MPC, which will be explained in detail in Chapter 4.

Equation 3.5.6 is often used to evaluate the fitting percentage (FP) of a model. The closer FP is to 100%, the better the fit. The measured motor speed from three pump control validation tests ("PTest3", "PTest5", and "PTest6" from Chapter 5) are used to compare with the model prediction values. The results are listed in Table 3.5.2. As the prediction horizon expands, FP decreases from 96.10% for a 1-step ahead prediction to 59.93% for a 9-step ahead prediction for pump A on average. With pump B, the corresponding FP values were similar (specifically 96.66% and 62.26%). It should be noted that a decrease in FP with increasing prediction horizon is a common occurrence. Plots comparing the experimental speed (from "PTest5") to the ARX model predictions for the 1-step, 6-step and 9-step horizons are shown in Figure 3.5.6. The prediction errors are imperceptible for the 1-step curve and small for 6-step curve. They become more prominent near the peaks of the 9-step prediction curve.

$$\mathrm{FP} = \left(1 - \frac{\|\mathbf{y} - \hat{\mathbf{y}}\|}{\|\mathbf{y} - \bar{y}\|}\right) \times 100\% \tag{3.5.6}$$

where FP is the fitting percentage, $\|\cdot\|$ is the Euclidean vector norm, $\mathbf{y}$ are the measured values, $\hat{\mathbf{y}}$ are the predicted values, and $\bar{y}$ is the mean of the measured values.

Table 3.5.2 Comparison of experimental results and ARX model prediction of different horizons

	Test	FP (1-step prediction)	FP (6-step prediction)	FP (9-step prediction)
Pump A	PTest3	95.98%	70.52%	59.31%
	PTest5	96.17%	72.39%	60.62%
	PTest6	96.16%	70.54%	59.86%
	Mean	96.10%	71.15%	59.93%
Pump B	PTest3	95.84%	69.25%	56.68%
	PTest5	97.04%	79.57%	57.22%
	PTest6	97.09%	79.72%	72.89%

	Mean	96.66%	76.18%	62.26%

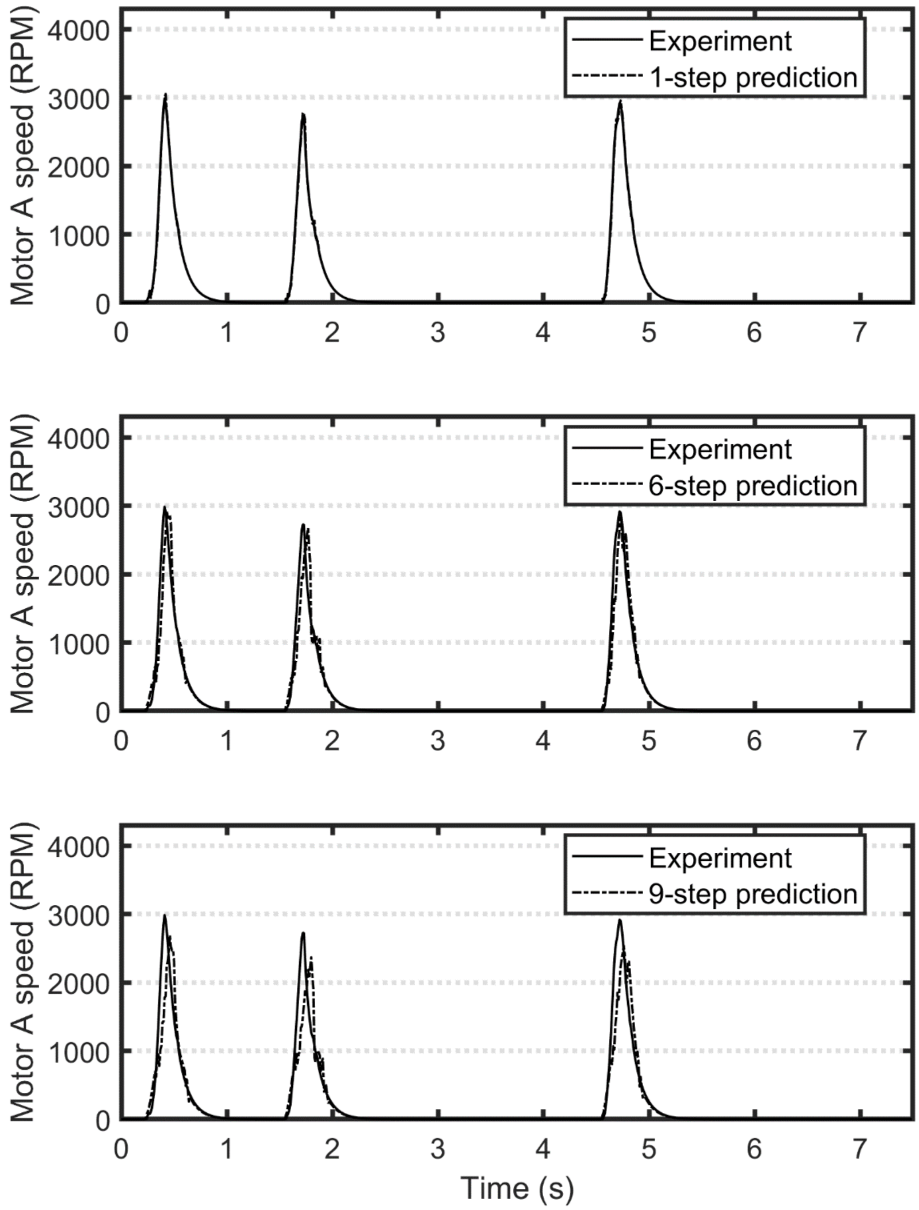

Figure 3.5.6 Comparison of experimental results and ARX model predictions of the motor speed for pump A for different prediction horizons.

3.5.4 Pump mass flowrate model

After collecting the tank pressure vs. time data, a low pass zero-phase Butterworth filter of order 10, and cutoff frequency of 5 Hz, was used to filter out the high frequency noise in the pressure data, then its numerical derivative was calculated, and finally (3.4.2) was used to calculate the pump's mass flowrate. So the results can be seen more clearly, only the 5 - 25 s of the data are presented in Figures 3.5.7 and 3.5.8. The positive correlation between the flowrate and motor speed can be observed in these plots. The plotted negative flowrate values were mainly caused by leakage accumulated from the pneumatic connections in the loop. These negative values were excluded from the model training set. For the better noise suppression, the following "binning strategy" was implemented for the mass flowrates: the motor speed and pressure data were normalized first using (3.5.7) – (3.5.10), then 10 bins were used with each one, to create a 10 x 10 grid of bins. The scaled mass flowrates were then placed into the appropriate bins. The mean values of the binned flowrates and the normalized motor speed and pressure data categorized in each bin formed the data points that were used for modeling the dependance of the mass flowrate on the motor speed and pressure.

$$n_a^*(t_k) = \frac{n_a(t_k) - n_{\min}}{n_{\max} - n_{\min}} \tag{3.5.7}$$

$$n_b^*(t_k) = \frac{n_b(t_k) - n_{\min}}{n_{\max} - n_{\min}} \tag{3.5.8}$$

$$P_a^*(t_k) = \frac{P_a(t_k) - P_{\min}}{P_{\max} - P_{\min}} \tag{3.5.9}$$

$$P_b^*(t_k) = \frac{P_b(t_k) - P_{\min}}{P_{\max} - P_{\min}} \tag{3.5.10}$$

Where n_a^* and n_b^* are the normalized motor speeds of pump A and pump B. $n_{\min}$ and $n_{\max}$ are the preset lower boundary and upper boundary for motor speed normalization. P_a^* and P_b^* are the normalized pressure of chamber A and chamber B. $P_{\min}$ and $P_{\max}$ are the preset lower boundary and upper boundary for pressure normalization.

The RMSE between the predicted mass flowrates from a 2nd order polynomial model and the processed mass flowrates was the optimization objective, with the additional constraint that the predicted mass flowrate should equal zero when the motor speed equals zero. MATLAB's fmincon function was used to solve the optimization problem. Finally, the pump mass flowrate models are given by:

$$\begin{aligned}\dot{m}_{pA}^{*}(t_k) = &-1.74\times10^{-22} + 2.34\times10^{-8} n_a^{*}(t_k) + 8.82\times10^{-8} n_a^{*}(t_k)^2 + \ldots \\ &1.04\times10^{-21} P_a^{*}(t_k) - 1.04\times10^{-21} P_a^{*}(t_k)^2 + 2.57\times10^{-8} n_a^{*}(t_k) P_a^{*}(t_k) + \ldots \\ &5.66\times10^{-9} n_a^{*}(t_k)^2 P_a^{*}(t_k) - 5.76\times10^{-8} n_a^{*}(t_k) P_a^{*}(t_k)^2 - 4.57\times10^{-8} n_a^{*}(t_k)^2 P_a^{*}(t_k)^2\end{aligned} \tag{3.5.11}$$

$$\begin{aligned}\dot{m}_{pB}^{*}(t_k) = &-4.06\times10^{-24} + 5.78\times10^{-8} n_b^{*}(t_k) + 5.00\times10^{-8} n_b^{*}(t_k)^2 + \ldots \\ &2.75\times10^{-23} P_b^{*}(t_k) - 3.10\times10^{-23} P_b^{*}(t_k)^2 - 8.80\times10^{-9} n_b^{*}(t_k) P_b^{*}(t_k) - \ldots \\ &5.77\times10^{-9} n_b^{*}(t_k)^2 P_b^{*}(t_k) - 2.25\times10^{-8} n_b^{*}(t_k) P_b^{*}(t_k)^2 - 1.52\times10^{-8} n_b^{*}(t_k)^2 P_b^{*}(t_k)^2\end{aligned} \tag{3.5.12}$$

$$\dot{m}_{pA}(t_k) = \frac{\dot{m}_{pA}^{*}(t_k) * (P_{\max} - P_{\min})}{100} \tag{3.5.13}$$

$$\dot{m}_{pB}(t_k) = \frac{\dot{m}_{pB}^{*}(t_k) * (P_{\max} - P_{\min})}{100} \tag{3.5.14}$$

where $\dot{m}_{pA}^{*}$ and $\dot{m}_{pB}^{*}$ are the scaled pump A and pump B's output mass flow rate. $\dot{m}_{pA}$ and $\dot{m}_{pB}$ are the pump A and pump B's output mass flow rate.

The surfaces produced by the models (3.5.11) and (3.5.12) after denormalization are compared with the processed mass flowrate data (plotted as discrete blue points) for pumps A and B in Figures 3.5.9 and Figure 3.5.10, respectively. For model validation, the 10-step ahead predictions were calculated for the 1000th, 2500th, and 4000th samples from a validation experiment. The measured motor speed and the initial pressure values at each point were set to be the model inputs, and the predicted pressures for the following 10 samples were compared with the measured pressures. These results are plotted in Figures

3.5.11 and 3.5.12 for pumps A and B, respectively. It can be observed that the predictions only diverge slightly from the measured future pressures over the 10-step horizon. To quantify the differences, the mean absolute value of the prediction error within the prediction horizon (MEANAE), and maximum absolute value of the prediction error within the prediction horizon (MAXAE) were calculated. These are listed in Table 3.5.3. These results show that the prediction errors with both pumps are similar. They also show that the overall maximum MAXAE equals 0.39 kPa which is only 0.26% of the pump's outlet pressure.

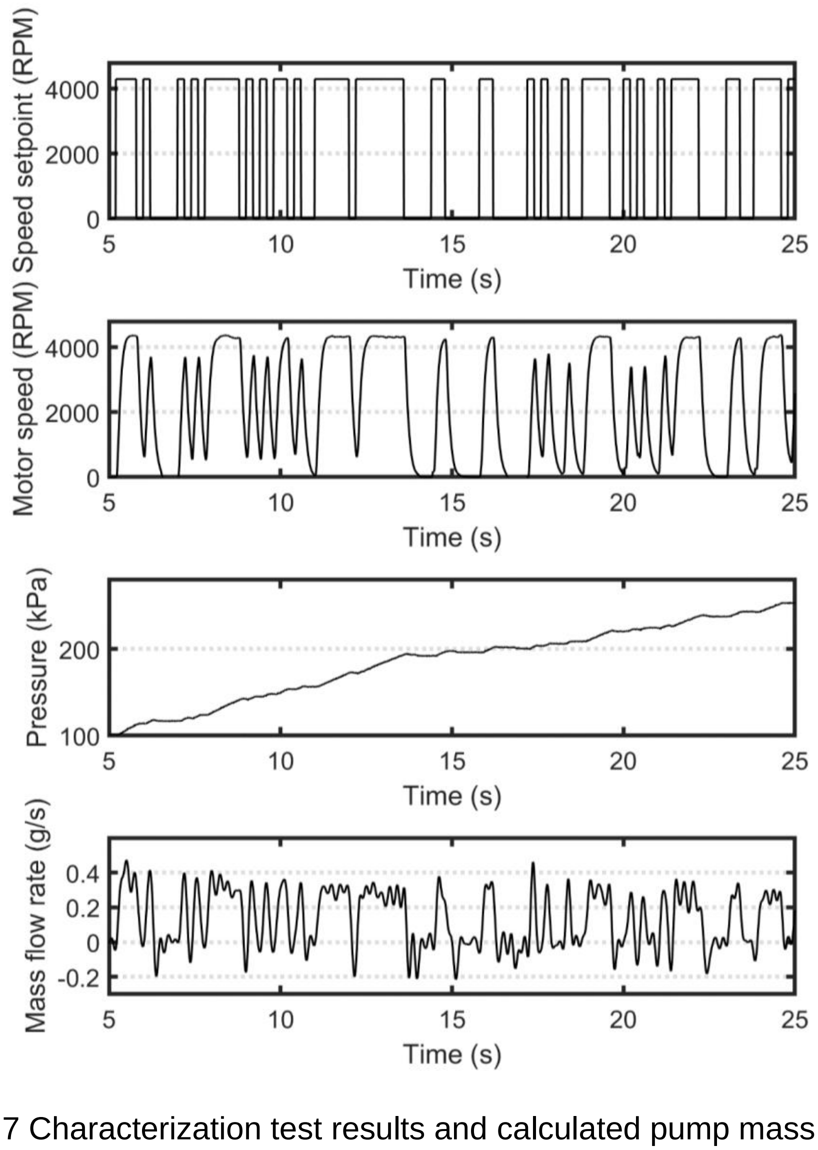

Figure 3.5.7 Characterization test results and calculated pump mass flowrates of pump A in 5 - 25 s of the 80 s test.

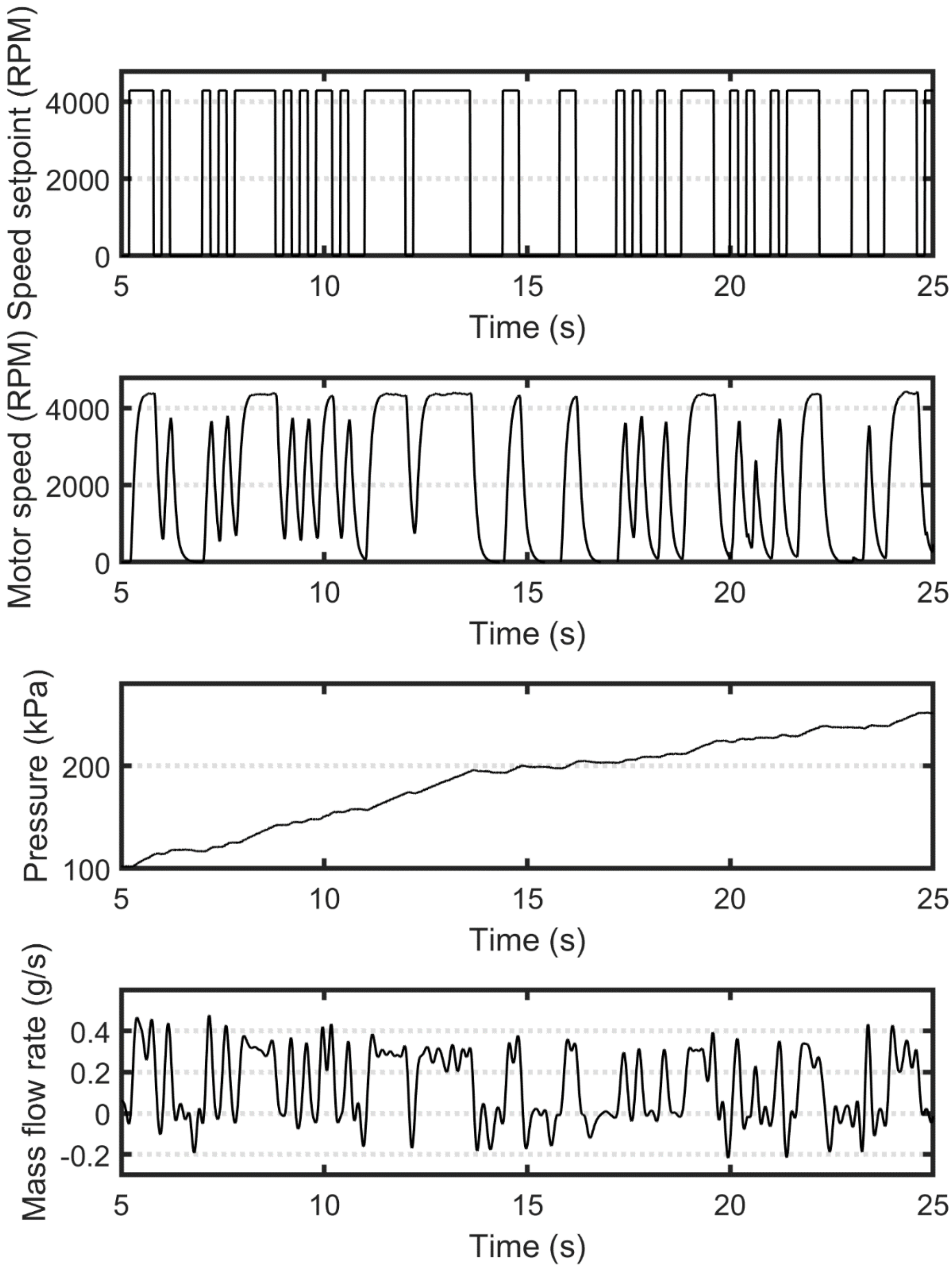

Figure 3.5.8 Characterization test results and calculated pump mass flowrates of pump B in 5 - 25 s of the 80 s test.

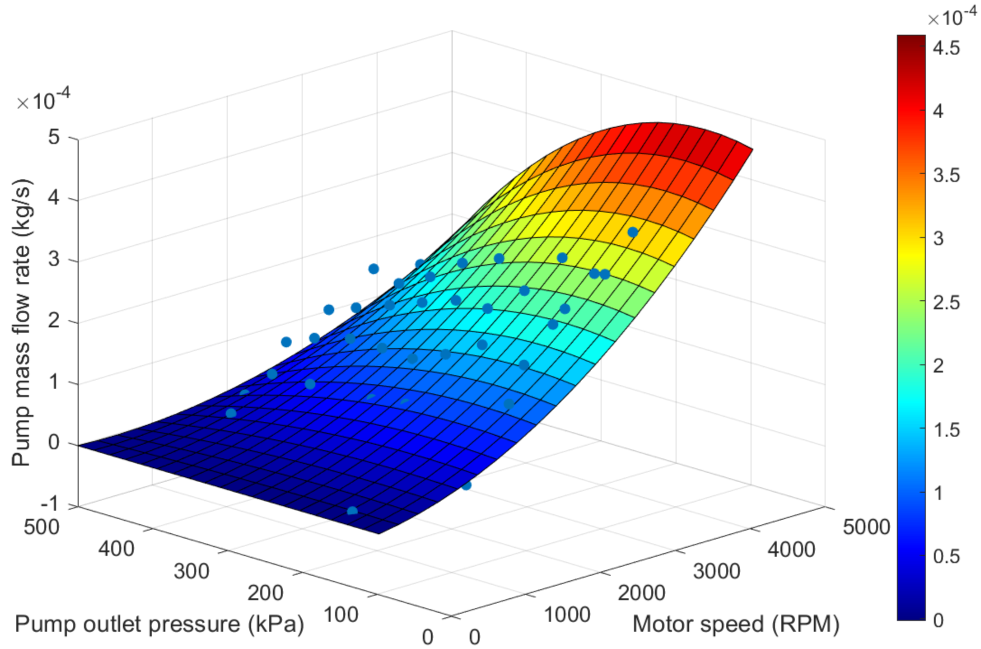

Figure 3.5.9 Processed mass flowrate data (shown as blue points) and the surface produced by the fitted polynomial model for pump A.

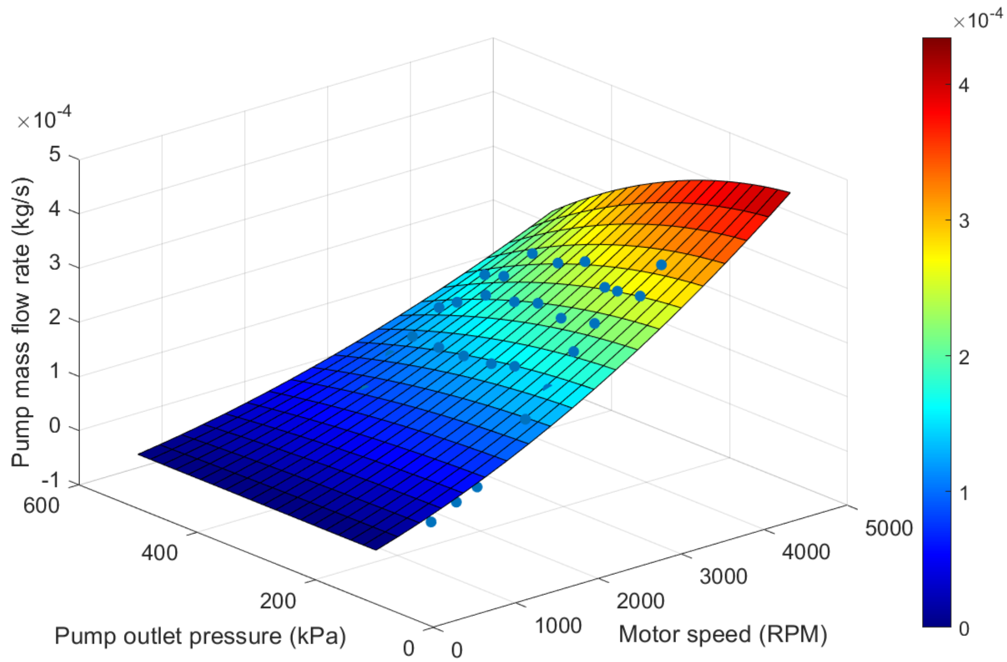

Figure 3.5.10 Processed mass flowrate data (shown as blue points) and the surface produced by the fitted polynomial model for pump B.

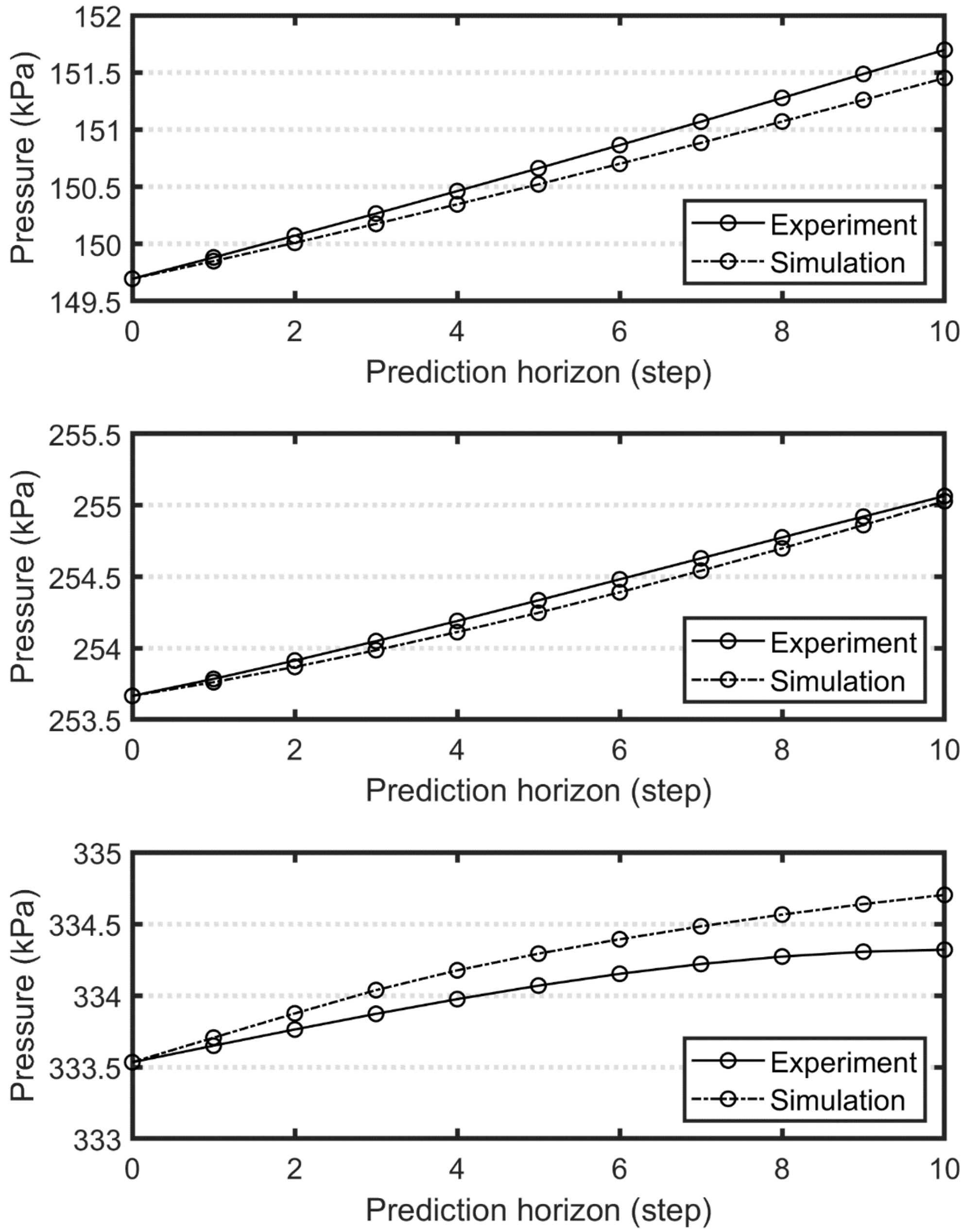

Figure 3.5.11 Comparison of the 10-step pressure prediction for pump A using its polynomial model to the measured pressure.

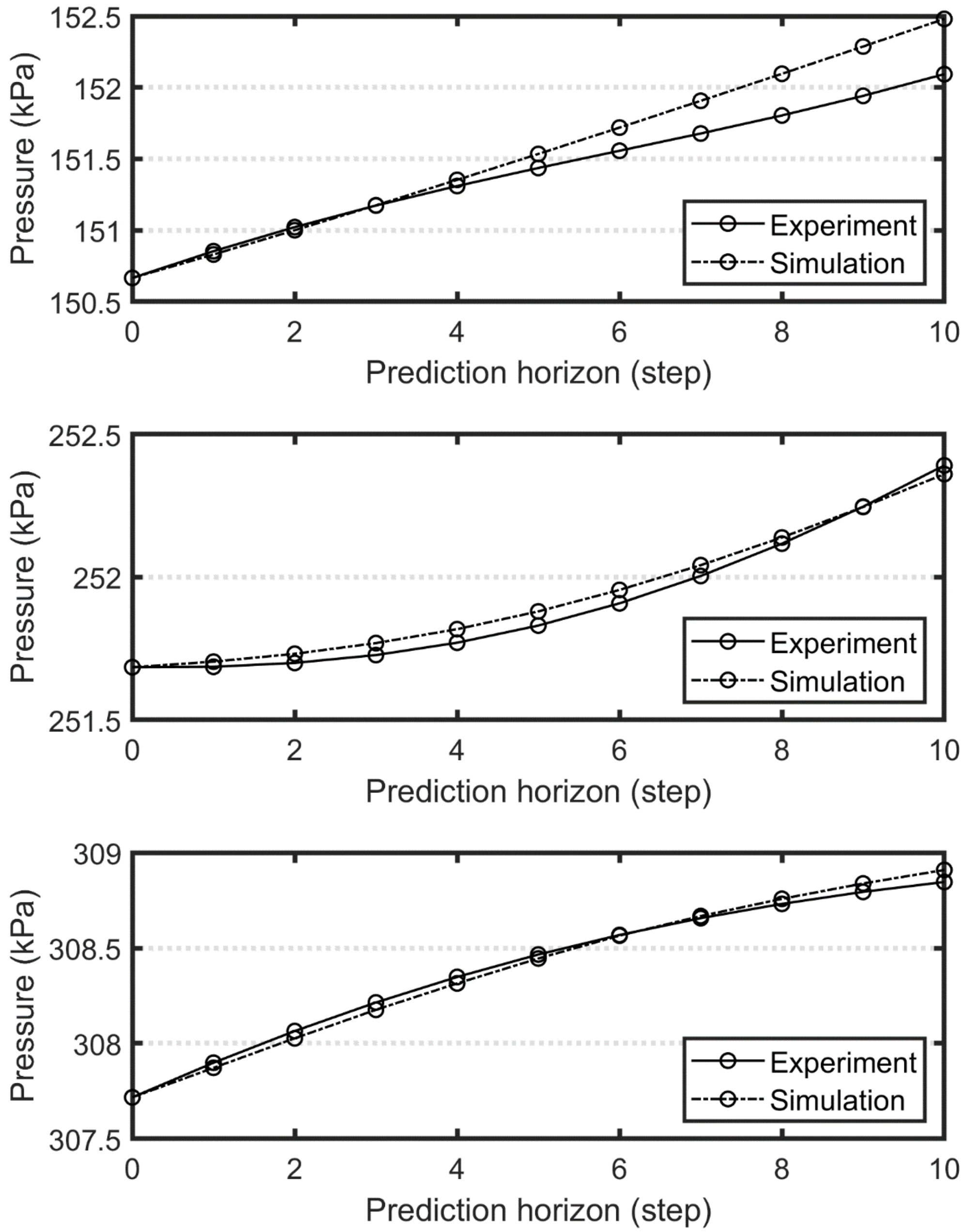

Figure 3.5.12 Comparison of the 10-step pressure prediction for pump B using its polynomial model to the measured pressure.

Table 3.5.3 The MEANAE and MAXAE values for the pump A and pump B mass flowrate polynomial models obtained from the validation data.

	Sample	MEANAE (kPa)	MAXAE (kPa)
Pump A	1000	0.13	0.25
	2500	0.06	0.09
	4000	0.21	0.38
Pump B	1000	0.15	0.39
	2500	0.03	0.05
	4000	0.03	0.06

3.5.5 Pump energy consumption model

A pump energy consumption model is required to help the MPC controller make better energy-saving decisions. Since the motor current and voltage signals have high noise levels, designing the model for predicting the energy consumption to use their online measurements as inputs was not pursued. Instead, similar to modeling the pump's mass flowrate, a polynomial function with motor speed and outlet pressure as independent variables will be used to model the pump's energy consumption.

To obtain the data to fit, the pump's power consumption at each sampling instant was first calculated by multiplying the measured values of the motor current and voltage. So the results can be seen more clearly, only the calculated results from the 5 - 25 s interval of the characterization tests for pumps A and B are plotted in Figures 3.5.13 and 3.5.14, respectively. It is clear that the power consumption grows when either the motor speed or pressure load increases. The peak consumption reached by pump A's motor was around 130 W, while for pump B's motor it was around 100 W.

The binning strategy employed in Section 3.5.4 was applied to the power data to get the mean power consumption in each bin. The fitting procedure described in Section 3.5.4 was then used to obtain the following power consumption models:

$$\begin{aligned} p_a^*(t_k) = &-1.77\times10^{-24} + 0.42n_a^*(t_k) - 0.11n_a^*(t_k)^2 + ... \\ &2.40\times10^{-23}P_a^*(t_k) + 5.96\times10^{-24}P_a^*(t_k)^2 + 1.86n_a^*(t_k)P_a^*(t_k) - ... \\ &0.48n_a^*(t_k)^2P_a^*(t_k) - 0.52n_a^*(t_k)P_a^*(t_k)^2 - 0.36n_a^*(t_k)^2P_a^*(t_k)^2 \end{aligned} \tag{3.5.15}$$

$$\begin{aligned} p_b^*(t_k) = &-5.88\times10^{-22} + 0.26n_b^*(t_k) + 0.07n_b^*(t_k)^2 + ... \\ &3.80\times10^{-21}P_b^*(t_k) - 1.43\times10^{-21}P_b^*(t_k)^2 + 2.52n_b^*(t_k)P_b^*(t_k) - ... \\ &1.61n_b^*(t_k)^2P_b^*(t_k) - 1.38n_b^*(t_k)P_b^*(t_k)^2 + 0.75n_b^*(t_k)^2P_b^*(t_k)^2 \end{aligned} \tag{3.5.16}$$

$$p_a(t_k) = p_a^*(t_k) * (p_{\max} - p_{\min}) + p_{\min} \tag{3.5.17}$$

$$p_b(t_k) = p_b^*(t_k) * (p_{\max} - p_{\min}) + p_{\min} \tag{3.5.18}$$

where p_a^* and p_b^* are the normalized pump A and pump B's power consumption. p_a and p_b are pump A and pump B's power consumption. $p_{\min}$ and $p_{\max}$ are the preset lower boundary and upper boundary for power consumption normalization.

Using the outputs of (3.5.17) and (3.5.18), the energy consumed by pumps, E_p, over the kth sampling period can be approximated using Euler integration as follows:

$$E_p(t_k) = (p_a(t_k) + p_b(t_k)) \cdot T_s \tag{3.5.19}$$

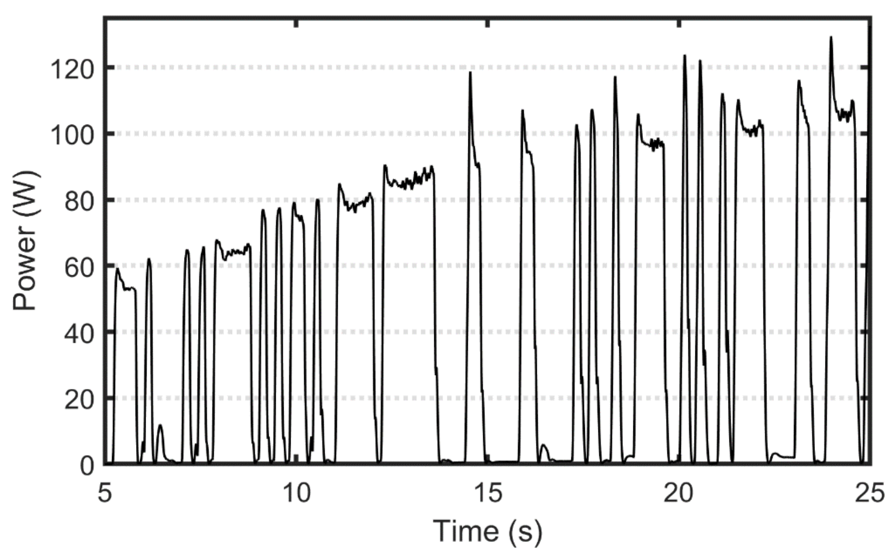

Figure 3.5.13 Calculated power consumption for pump A during the 5 - 25 s interval of its characterization test.

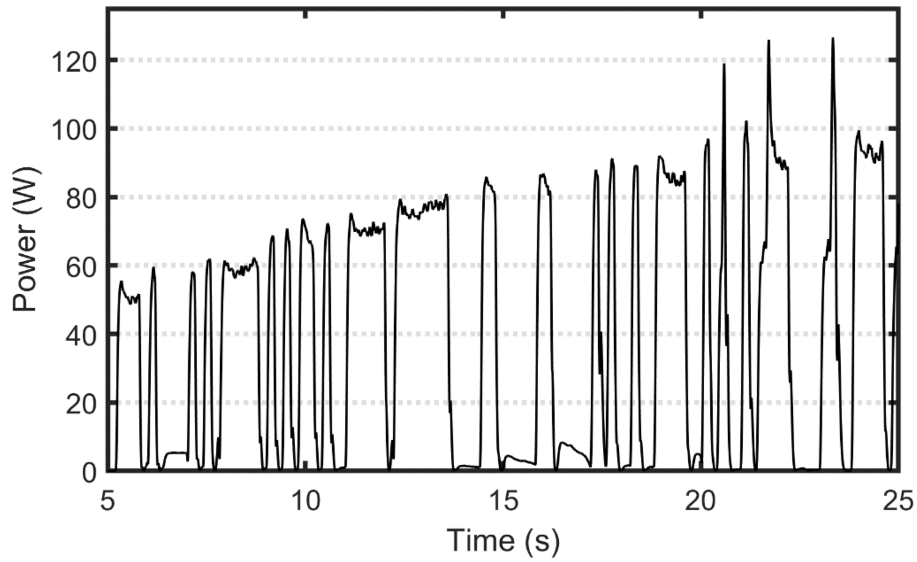

Figure 3.5.14 Calculated power consumption for pump B during the 5 - 25 s interval of its characterization test.

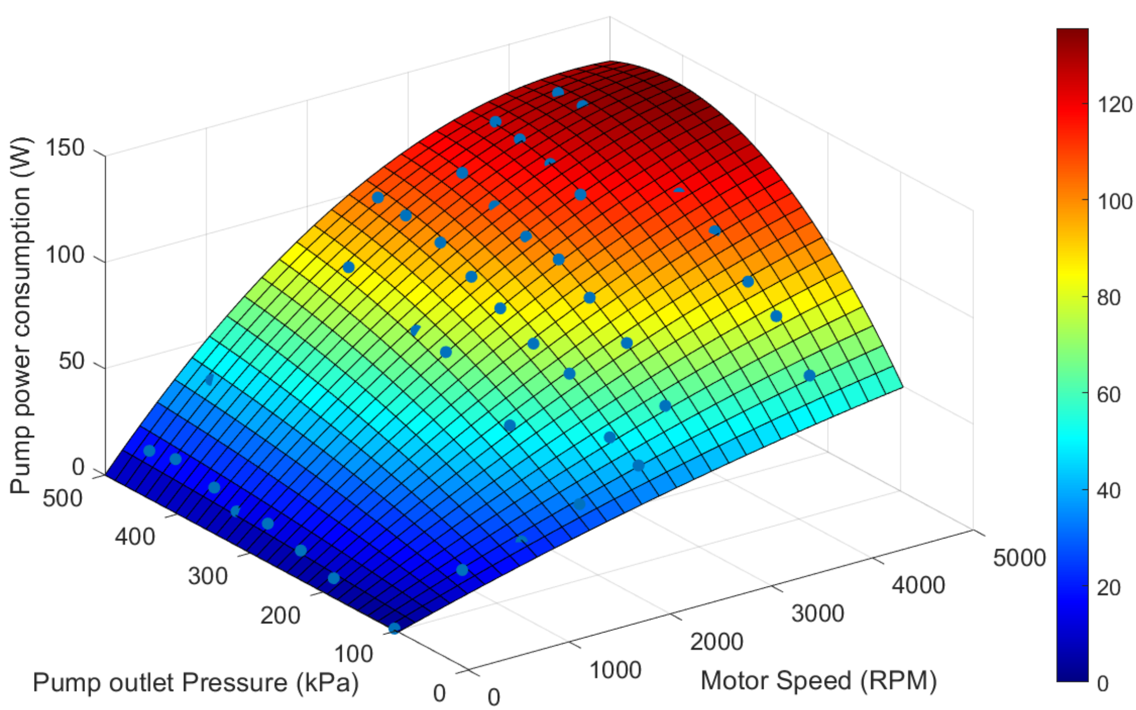

Figure 3.5.15 Processed power data (shown as blue points) and the surface produced by the fitted polynomial model for pump A.

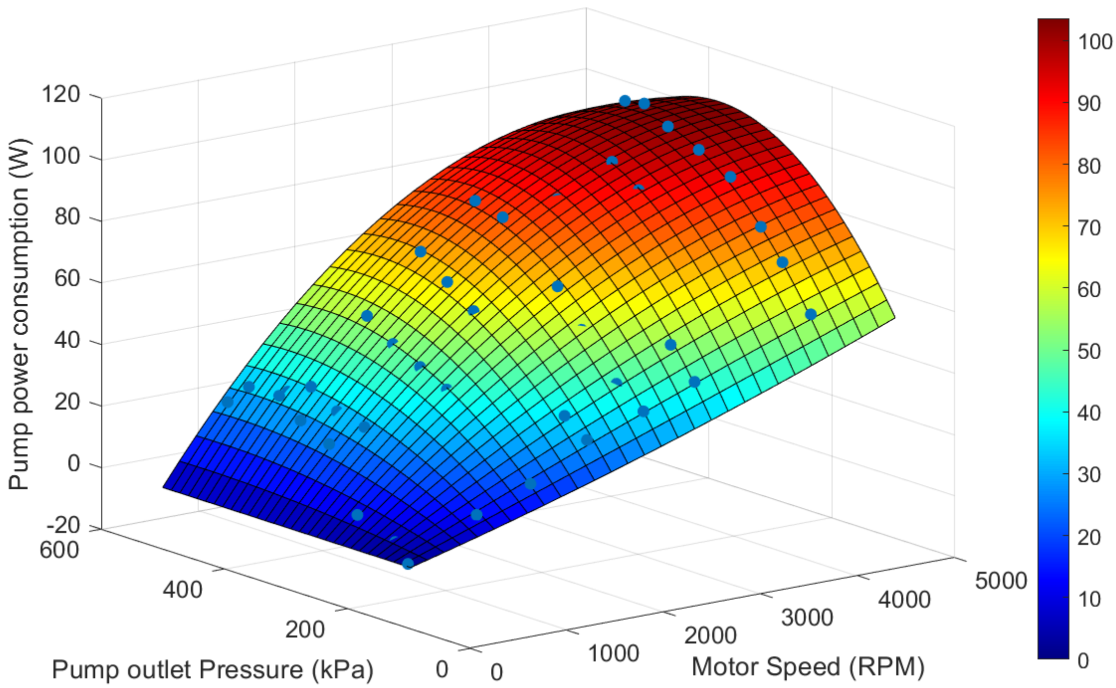

Figure 3.5.16 Processed power data (shown as blue points) and the surface produced by the fitted polynomial model for pump B.

The surfaces produced by (3.5.15) - (3.5.18) are compared with the processed power data (plotted as discrete blue points) for pumps A and B in Figures 3.5.15 and Figure 3.5.16, respectively. These figures show that the surfaces fit the data points well. The models were validated by first performing a validation experiment, then using the measured motor speeds and pump outlet pressures as inputs to the model equations (3.5.15) and (3.5.18), and finally comparing the predicted and experimentally measured energies (obtained from the power using Euler integration). The experimental and predicted energy consumptions of both pumps are compared in Figure 3.5.17. Unfortunately, the predictions shown in this figure are not very accurate. However, from the MPC perspective, the most important point is the predicted values only need to be accurate enough for the MPC to compare and properly choose from the five operating modes it uses. Then the MPC controller's weighting coefficient can be tuned based on the particular control performance requirements.

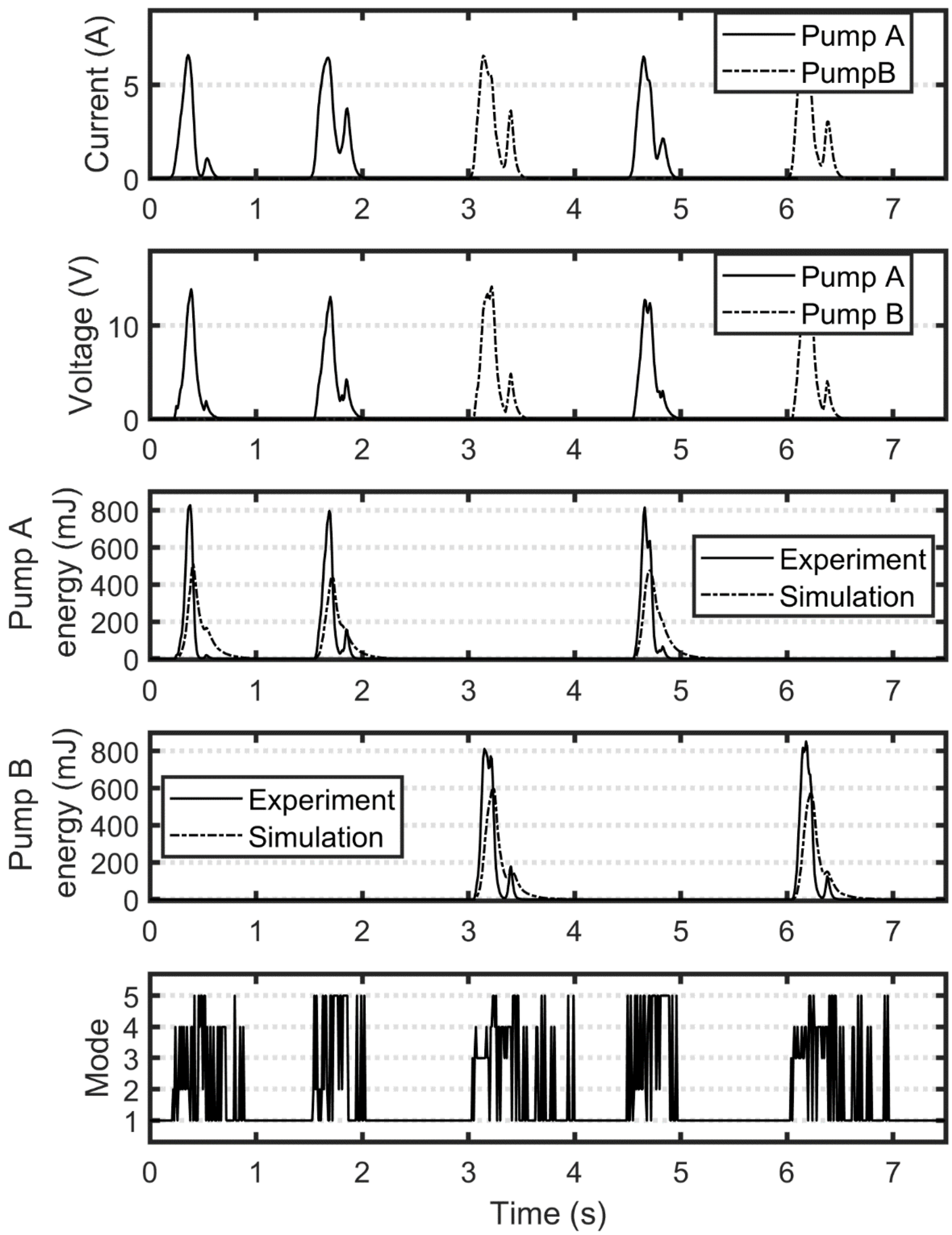

Figure 3.5.17 Comparison of experimental and predicted energy consumptions of pumps A and B for a sequence of operating modes.

3.6 Friction model

Based on (3.3.8), the friction force was estimated using:

$$\hat{F}_f = \hat{F}_p - M\hat{\ddot{y}} \tag{3.6.1}$$

$$\hat{F}_p = P_a A_a - P_b A_b - P_{atm} A_{rod} \tag{3.6.2}$$

where $\hat{F}_f$ is the estimated friction force; $\hat{\ddot{y}}$ is the approximate acceleration (calculated by taking the numerical second derivative of the measured displacement and low-pass filtering it with a 20 Hz cut off, 1st order, digital filter); and $\hat{F}_p$ is the approximate pneumatic force (calculated using the measured chamber pressures). A_{rod} is the cross-sectional area of the cylinder rod.

Based on preliminary experiments, the friction was found to be mainly dependent on the carriage velocity and the position of the carriage along the guide. Specifically, due to machining inaccuracy and assembly tolerances, the cylinder and guide were slightly misaligned. The misalignment caused the friction to increase as the rod extends and the position becomes more positive. The structure of the model is based on these observations. The static friction will be modelled as a function of the carriage position, while the dynamic friction will be modelled as a polynomial function of the position and velocity.

When post processing the measured data, it was discovered that the calculated friction force lagged behind the velocity. This was probably caused by the measured pressures used to calculate $\hat{F}_p$ lagging behind the actual pressures on the piston due to the effects of airflow dynamics. This lag was corrected by shifting the pressure data one sampling period ahead to make the velocity and friction force in phase.

Open-loop testing is the traditional approach used to collect the data required for characterizing friction. This could involve step changes in the valve input command (Ning & Bone, 2005) or generating the valve operating modes randomly from a uniform probability distribution. The latter method produces bidirectional movements, but the carriage's position is not controlled so it may not cover the full range of motion and may even collide with the guide ends (Zhang, 2015). These open-loop methods are not applicable to our research, since carriage position needs to be included in the friction model, and the movements should uniformly cover the full length of the guide as much as possible. Closed-loop testing is obviously a better option to control the start/stop of the carriage along the guide (without collisions) for static friction data collection.

In this research, a total of eight closed-loop experiments were performed using the MPC controller (presented in Chapter 4) with the VC circuit to collect the friction modeling data. Two setpoint trajectories, shown in Figure 3.6.1, were designed for these tests. To allow dynamic friction and static friction conditions to exist at a variety of locations covering the carriage's range of motion these setpoints consisted of a series of steps with different magnitudes as shown in the figure. Four tests were performed with each setpoint. For these tests, the MPC controller used the following very simplified friction model:

$$F_f = F_{f,temp}\,sign(\hat{\dot{y}}) \tag{3.6.3}$$

where $\hat{\dot{y}}$ is the velocity calculated by backward differencing the position measurements and $F_{f,temp}$ = 1 N.

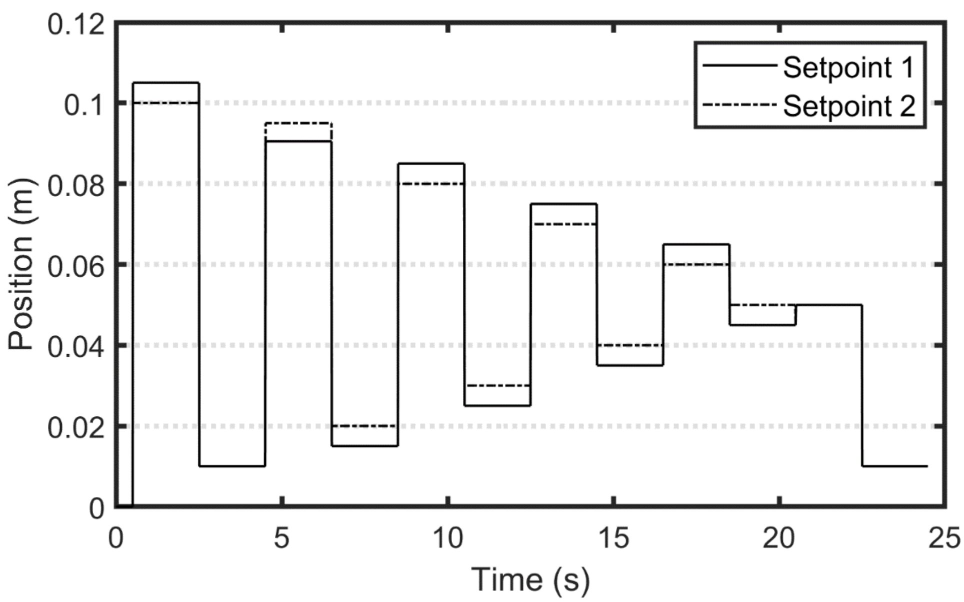

Figure 3.6.1 Position setpoints used for the friction characterization tests.

During each test, the carriage (plus its payload) stopped and then restarted its motion as the MPC controller made its position follow the step changes in the setpoint.

The friction values calculated using (3.6.1) when the sensed velocity was zero were saved to create the static friction modeling dataset. It was observed that the static friction magnitudes from motions in the positive and negative directions were similar, so the data was merged after calculating the absolute values. This produced a static friction dataset containing 7426 samples. These are plotted as blue circles in Figure 3.6.2. It is important for the model not to underestimate the static friction, since the MPC will have difficulty moving the carriage if the predicted static friction is underestimated. To make underestimation unlikely, the points were covered by the envelope line shown in Figure 3.6.2, which represents the max friction value at each position. The polynomial position-dependent static friction model was shown as follows:

$$F_s(y) = 394.11y^2 - 1.08y + 0.6 \tag{3.6.4}$$

where $F_s(y)$ is the static friction force in N, and y is the carriage position in m. The RSME of the fit is 0.24 N.

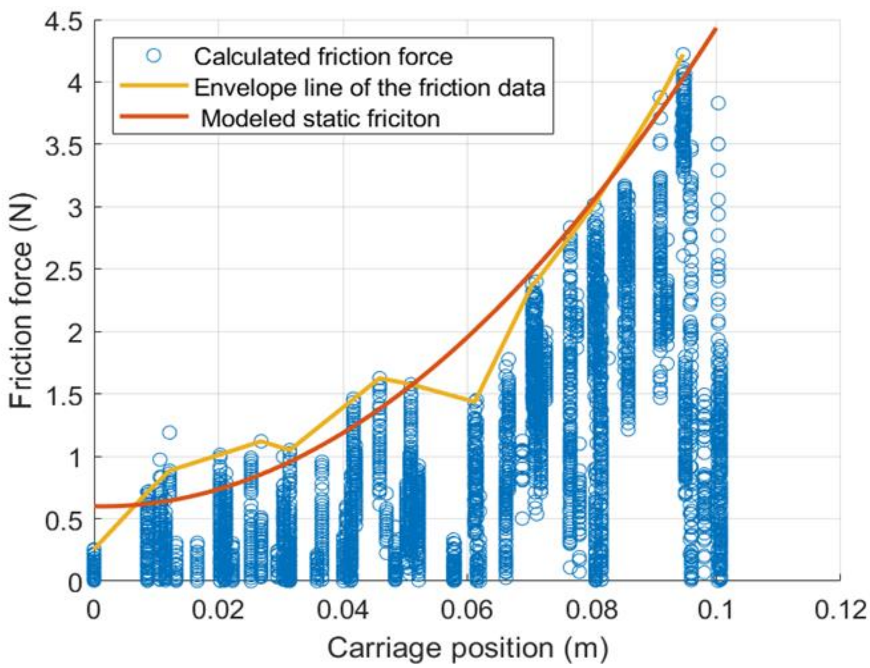

Figure 3.6.2 Static friction raw data and modeling.

The rest of the data with nonzero velocities were saved for identifying the dynamic friction model. Since the calculated values of the dynamic friction were different for the positive and negative velocities, and the values at the boundary with zero velocity are not continuous, the friction forces for the two directions were modeled separately. To suppress the noise of the raw data, a binning strategy similar to the one used in Section 3.5.4 was used. Thirty bins evenly covering the range 0 to 0.12 m were used with the position data, and another thirty bins covering the magnitude range 0 to 1.2 m/s were used with the velocity data to create a 30 x 30 grid of bins. The forces were then placed into the appropriate bins. The mean values of the binned forces and the mean values of the carriage position and velocity data categorized in each bin formed the data points that were used for modeling the dependance of the dynamic friction on the position and velocity.

The linearly interpolated surface model of this data is shown in Figure 3.6.3. Although this surface shows the trend of data variation well, computing the value of the dynamic friction from it would require significant computations. To simplify the model and make controller calculations faster, the following second order polynomial model of the position and velocity was fit to the dynamic friction along the positive direction, F_{dp}, using the method of Section (3.5.4):

$$F_{dp}(y,\dot{y}) = -26.60y + 18.83\dot{y} + 746.96y^2 - 1.96y\dot{y} + 1.92\dot{y}^2 + 0.50 \qquad (3.6.5)$$

The dynamic friction data and the polynomial surface model are shown in Figure 3.6.4. It can be observed that the surface fits the data quite well. The RMSE of the fit is 1.90 N.

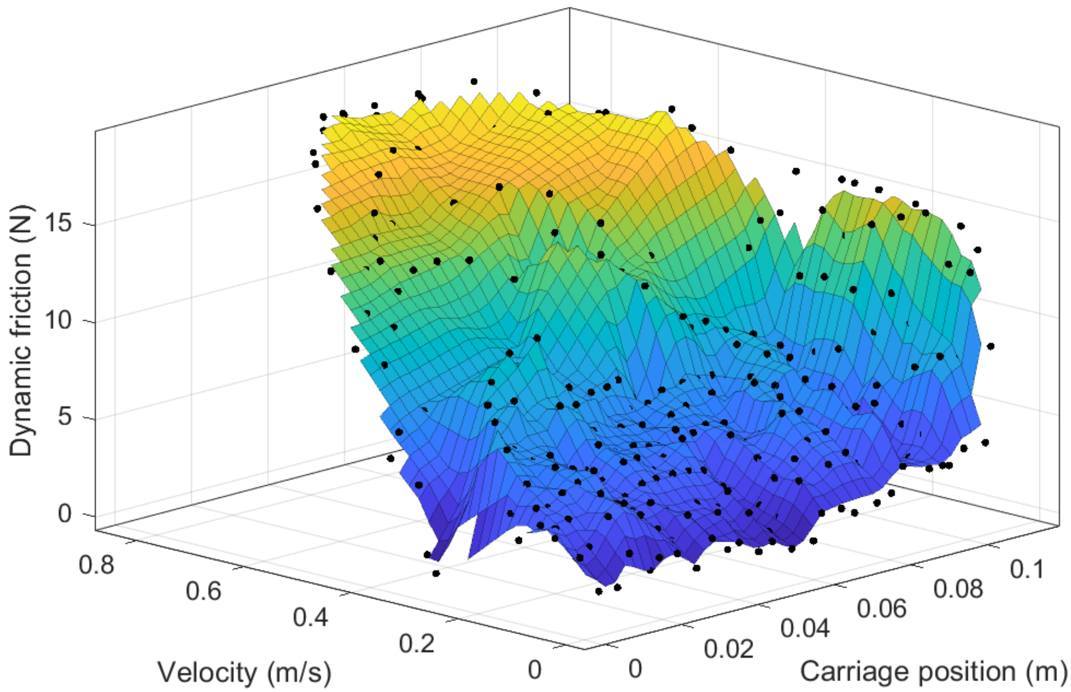

Figure 3.6.3 Linearly interpolated surface model of the dynamic friction in the positive direction.

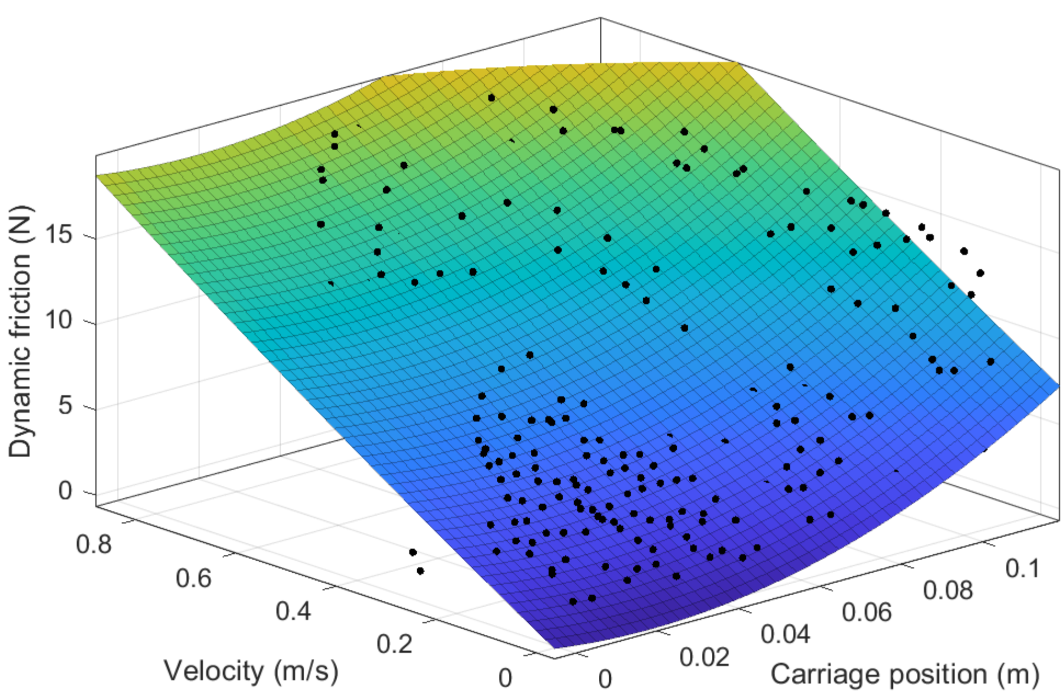

Figure 3.6.4 Polynomial surface model of the dynamic friction in the positive direction.

Similarly, the linearly interpolated surface model of the dynamic friction in the negative direction, F_{dn}, is shown in Figure 3.6.5, and its fitted polynomial model is as follows:

$$F_{dn}(y,\dot{y}) = -20.39y + 9.37\dot{y} - 68.62y^2 + 53.61y\dot{y} - 10.60\dot{y}^2 - 0.73 \tag{3.6.6}$$

The dynamic friction data and the polynomial surface model are shown in Figure 3.6.6. The fit is better than with the positive direction model, and its RMSE is only 1.06 N.

Finally, the complete friction force model is defined by:

$$F_f(y,\dot{y}) = \begin{cases} F_p & \text{if } \dot{y} = 0 \text{ and } \left|F_p\right| < F_s(y) \\ F_s(y) & \text{if } \dot{y} = 0 \text{ and } F_p > F_s(y) \\ -F_s(y) & \text{if } \dot{y} = 0 \text{ and } F_p < -F_s(y) \\ F_{dp}(y,\dot{y}) & \text{if } \dot{y} > 0 \\ F_{dn}(y,\dot{y}) & \text{if } \dot{y} < 0 \end{cases} \tag{3.6.7}$$

To validate the friction model, we first used the measured pressure data P_a and P_b from a validation test to predict the carriage acceleration $\hat{\ddot{y}}$ using the equation:

$$\hat{\ddot{y}} = (P_a A_a - P_b A_b - P_{atm} A_{rod} - \hat{F}_f) / M \tag{3.6.8}$$

Next, the velocity $\dot{y}$ and position y were integrated from $\hat{\ddot{y}}$ using the Verlet method as follows:

$$\hat{\dot{y}}(t_k + T_s) = \dot{y}(t_k) + \frac{\hat{\ddot{y}}(t_k) + \hat{\ddot{y}}(t_k + T_s)}{2} T_s \tag{3.6.9}$$

$$\hat{y}(t_k + T_s) = y(t_k) + \dot{y}(t_k) T_s + \frac{1}{2}\hat{\ddot{y}} T_s^{\,2} \tag{3.6.10}$$

A comparison of the experimental position vs. time results with the simulated position results obtained using (3.6.4) – (3.6.10) is shown in Figure 3.6.7. The agreement of the results, especially over the short prediction horizons (~100 ms) that will be used with the MPC controller, demonstrates the effectiveness of the developed friction model and Verlet integration method for this application.

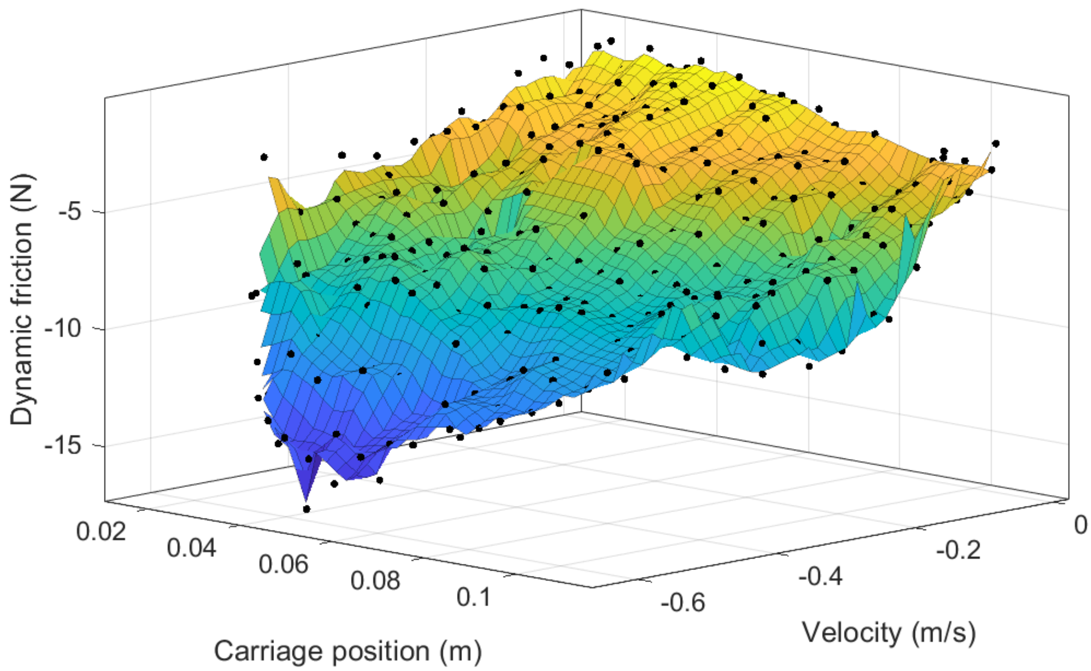

Figure 3.6.5 Linearly interpolated surface model of the dynamic friction in the negative direction.

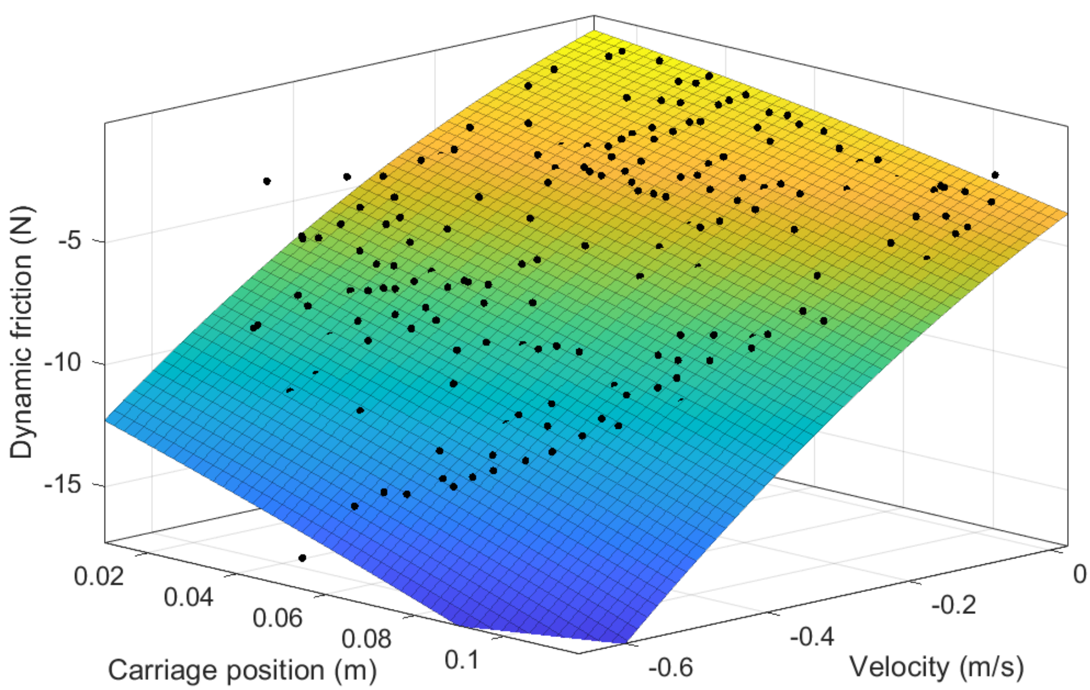

Figure 3.6.6 Polynomial surface model of the dynamic friction in the negative direction.

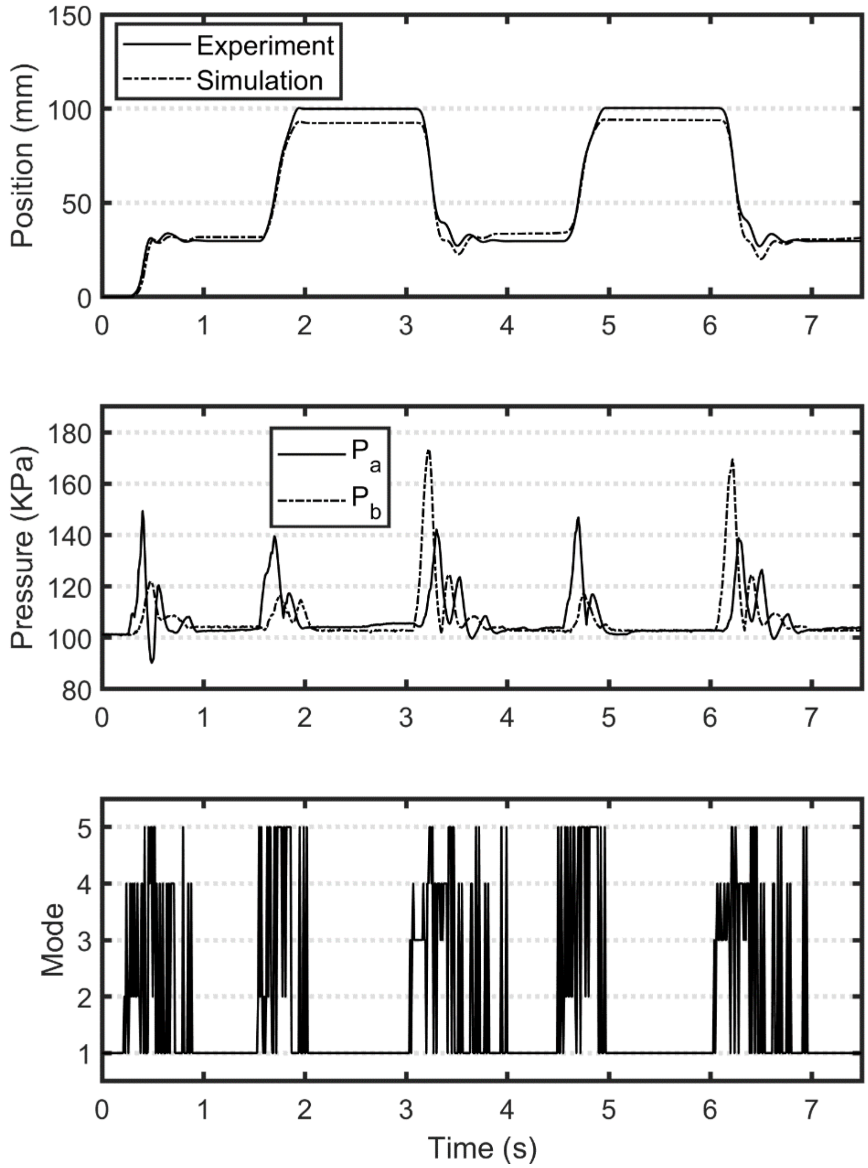

Figure 3.6.7 Comparison of experimental position vs. time results with simulation results obtained using the developed friction model.

Chapter 4 - Controller Design

4.1 Introduction

MPC is an advanced model-based control strategy in which the control action is obtained by repeatedly solving a finite horizon open-loop optimization problem in real-time. At each sampling period, the directly measured and/or estimated current system states are set as initial states for the following prediction. The optimization result depends on the designed cost function and the chosen constraints on the variables. Only the first element in the optimal sequence of control actions is applied to the system. The main advantage of MPC is it not only considers the information from the current and previous data samples, but also the future model-based predictions of the states and future values of the setpoint in the optimization problem.

There are three critical factors determining whether a real-time MPC strategy can be implemented successfully. The first one is the accuracy of the system model. If the model is not sufficiently accurate then the model-based predictions may cause the MPC controller to choose a non-optimal control action. The second one is the system model must be concise so it can be computed quickly. The third factor is the optimization algorithm must be capable of returning the optimal control action quickly enough that it can be applied to the system within the current sampling period, which is 10 ms in this research.

The duration of the optimization process can be reduced by tuning the MPC parameters to limit the potential sequences of control actions evaluated during the optimization, or by designing a faster optimization algorithm. Discrete-valued MPC (DVMPC) solves for a finite set of discrete-valued control actions, termed "operating modes", rather than the continuous-valued control actions used with traditional MPC. It was chosen for this research for the following reasons:

1. It can be used to directly switch each valve ON or OFF less often than PWM. The reduced number of switches prolongs the valve's life.
2. Using the nonlinear model developed in Chapter 3 requires the MPC to solve a nonlinear optimization problem. While other solutions for nonlinear MPC

problems exist, they often produce only locally optimal solutions, whereas DVMPC produces the globally optimal solution for the operating mode.

3. It is computationally simple enough to meet the real-time requirements using a typical PC.

In this chapter, improved versions of DVMPC designed specifically for the DPC and VC circuits are proposed. Following the naming convention from our lab's prior work (Bone & Chen, (2012), Bone et al., (2015), Qi et al., (2019)), they are named "DVMPC3P" and "DVMPC3V", respectively.

4.2 Design of DVMPC3P and DVMPC3V

4.2.1 Introduction

The first step when designing DVMPC is choosing the appropriate operating modes for the system. A small number of modes allows the optimal solution to be computed more quickly, but choosing too few modes is detrimental to the closed-loop performance. For the double-acting pneumatic cylinder used for this research, each chamber is required to realize charging and exhausting independently. That requires two operating modes per chamber. Another mode keeping the chambers closed was added since it is useful for saving energy, so there are totally five different operating modes. These modes are listed in Table 4.1.1 and Table 4.1.2 for the VC circuit and DPC circuit, respectively. In these tables, "1" means valve/pump is powered, while "0" means unpowered. Recall that all valves are NC.

Table 4.1.1 The five operating modes used for the VC circuit.

Mode	Description	CV1	CV2	EV1	EV2
M_1	All valves are closed	0	0	0	0
M_2	Chamber A charging	1	0	0	0
M_3	Chamber B charging	0	1	0	0
M_4	Chamber A exhausting	0	0	1	0

M_5	Chamber B exhausting	0	0	0	1

Table 4.1.2 The five operating modes used for the DPC circuit.

Mode	Description	CV1	Pump A	CV2	Pump B	EV1	EV2
M_1	All valves/pumps are closed	0	0	0	0	0	0
M_2	Chamber A charging	1	1	0	0	0	0
M_3	Chamber B charging	0	0	1	1	0	0
M_4	Chamber A exhausting	0	0	0	0	1	0
M_5	Chamber B exhausting	0	0	0	0	0	1

For the VC circuit, with mode M_1, all the solenoid valves are tuned off. With mode M_2, chamber A is charged, and chamber B is closed. With mode M_3, chamber B is charged, and chamber A is closed. With mode M_4, chamber A is exhausting, and chamber B is closed. With mode M_5, chamber B is exhausting, and chamber A is closed. For the DPC circuit, the working of valve A is synchronized with pump A under mode M_2 to realize the chamber A charging function, while valve B will be working with pump B to charge the chamber B in mode M_3.

In MPC, a change of the control action during the prediction horizon is termed a "move". The length of the prediction horizon of DVMPC is defined as:

$$N_p = N_m N_{delta} \tag{4.2.1}$$

where N_m is the number of moves, and N_{delta} is the number of prediction steps included within each move. This prediction horizon partitioning scheme is illustrated in Figure 4.2.1.

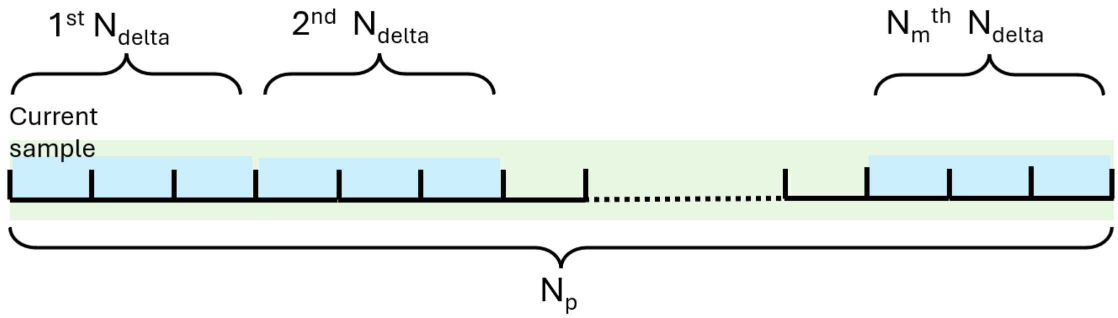

Figure 4.2.1 The prediction horizon partitioning scheme used with DVMPC3P and DVMPC3V.

With this scheme, when N_{delta} is fixed, the larger N_m, the longer the prediction horizon becomes. This can improve the optimality of the solution if the system model is sufficiently accurate within the prediction horizon, but it also leads to an exponential increase in computing cost. When N_m is fixed, the value of N_{delta} defines the temporal resolution of the control action. A small value of N_{delta} provides a finer resolution, but may also make the control overly aggressive and increase the frequency of mode switching which is detrimental for the valves and pump. Likewise, a larger value of N_{delta} tends to produce a more conservative control strategy with fewer mode switches, but may produce larger steady state errors. The DVMPC3P and DVMPC3V tuning strategies will be elaborated in Chapter 5.

While the scheme shown in Figure 4.2.1 is theoretically correct, it did not work well in practice because it was missing two time delays. The first delay was the time required for the software to read the sensor data, then compute the solution to the DVMPC's optimization problem and finally write the outputs according to the chosen operating mode. We termed this the "software delay". Using the hardware described in Section 3.2, the software delay equalled 1 sampling period (also termed a "1-step delay"). After including the software delay in the prediction, during preliminary testing we observed large oscillations between the position and its setpoint, which we concluded was caused by the delay between expected control actions and the actual ones due to the response times of ODC5 output modules and the solenoid valves. By adding another sampling period of "hardware delay" to the prediction, the oscillation was greatly suppressed in our preliminary experiments. The improved version of the prediction horizon partitioning scheme that includes these delays is shown in Figure 4.2.2.

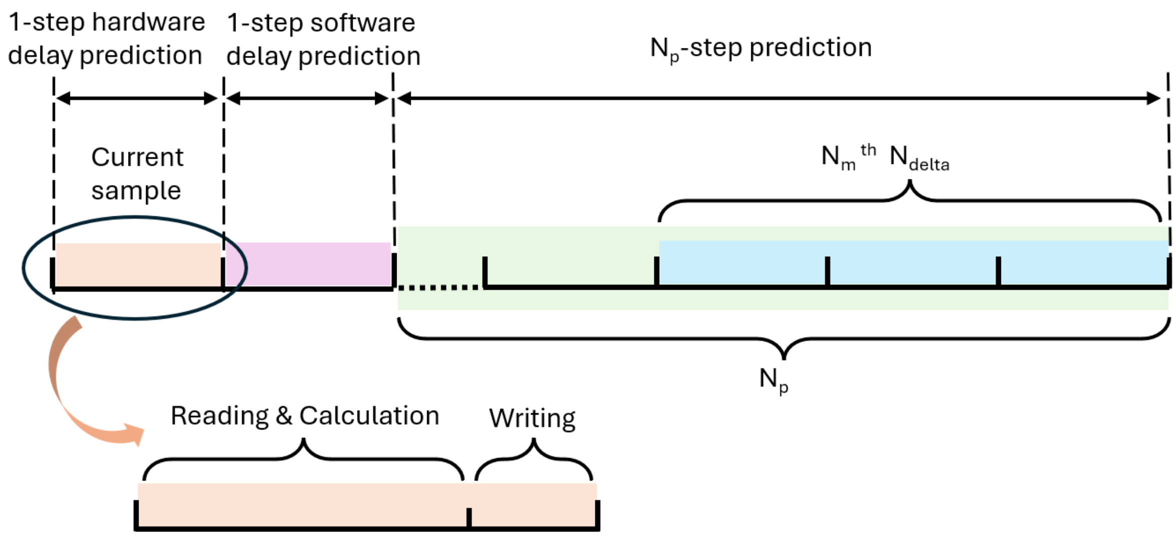

Figure 4.2.2 The improved prediction horizon partitioning scheme used with DVMPC3P and DVMPC3V.

4.2.2 Design of DVMPC3P for DPC

The objective of this control system is to provide energy savings without compromising actuator position tracking performance. This will be accomplished by including the energy consumptions predicted by the models in Section 3.4 and 3.5, along with two terms for reducing the position tracking errors, in DVMPC3P's cost function. Based on these considerations, the cost function designed for the DPC circuit is:

$$\begin{aligned} J &= \text{PTEC} + \text{BITAE} + \text{PVEC} + \text{PPEC} \\ &= \sum_{i=1}^{N_p} \left((\hat{y}(t_i) - y_d(t_i))^2 + \omega_{bi} \cdot (N_p - i + 1) \cdot T_s \cdot \left| \hat{y}(t_i) - y_d(t_i) \right| + \omega_v \cdot \hat{E}_v(t_i) + \omega_p \cdot \hat{E}_p(t_i) \right) \end{aligned} \tag{4.2.2}$$

where PTEC stands for position tracking error cost; BITAE stands for backward integral of time-weighted absolute error; PVEC stands for predicted valve energy consumption; PPEC stands for predicted pump energy consumption; t_k is the current sampling instant; T_s is the sampling period; $t_i = t_k + i \cdot T_s$ is the future sampling instant; $\hat{y}$ is the predicted position; y_d is the desired position; ω_{bi}, ω_p, and ω_v are weighting coefficients. ITAE is usually used to reduce the steady state error for an MPC controller by applying a larger weight to the predicted errors that are farther into the future. However, for the DPC circuit, the initial pump mass flowrate was found to be relatively large for small step sizes, like 30 mm. This caused the result calculated by DVMPC3P with only the PTEC term to choose mode M_1 (since it had the lowest cost) and the carriage failed to move. When ITAE was added to the cost, DVMPC3P planned to switch the pump ON near the end of the prediction horizon due to ITAE's integration feature, but DVMPC3P only implements the first element of the predicted modes, so a constant position error still occurred, until a larger setpoint change appeared. BITAE applies the larger weight at the start, which pushes the controller into making decisions that will change the current states faster. As a result, including BITAE was found to reduce the tracking errors much more than including ITAE did. PVEC is the energy cost of the four valves. Since all the modes except mode M_1 require the valves to be turned ON which consumes energy, PVEC helps save the energy by increasing the cost of those other modes. PPEC includes the energy cost of the pumps alone. Since the pump consumes more power than the valves, the DVMPC3P tends to choose valve exhausting instead of pump charging to move the carriage when the chambers are relatively high.

The following optimization problem is solved every sampling period:

$$U_{opt} = \arg \min_{U} J \tag{4.2.3}$$

subject to:

$$\hat{u} = \left[\hat{u}_1, \quad \hat{u}_2, \quad \hat{u}_3, \quad \hat{u}_4\right] \in M_i, \forall i = 1, 2, 3, 4, 5 \tag{4.2.4}$$

$$U = \left[\hat{u}(t_k), \quad \hat{u}(t_k + T_s), \quad \hat{u}(t_k + 2T_s), \quad \ldots \quad, \hat{u}(t_k + (N_p - 1)T_s)\right] \tag{4.2.5}$$

$$\left[\hat{y}(t_i+T_s),\ \hat{\dot{y}}(t_i+T_s),\ \hat{P}_a(t_i+T_s),\ \hat{P}_b(t_i+T_s),\ \hat{n}_a(t_i+T_s),\ \hat{n}_b(t_i+T_s)\right]=$$
$$f(\hat{u}(t_i),\ \hat{y}(t_i),\ \hat{\dot{y}}(t_i),\ \hat{P}_a(t_i),\ \hat{P}_b(t_i),\ \hat{n}_a(t_i),\ \hat{n}_a(t_i-T_s),\ \hat{u}_a(t_i-T_s),\ \hat{n}_b(t_i),\ \ldots \quad (4.2.6)$$
$$\hat{n}_b(t_i-T_s),\ \hat{u}_b(t_i-T_s))\quad \forall i=0,1,\ldots,N_p-1$$

where $\hat{u}_1,\ \hat{u}_2,\ \hat{u}_3,\ \hat{u}_4$ are the predicted control actions for CV2, EV2, CV1, and CV2. For DPC, the pump A and pump B control inputs are synchronized with $\hat{u}_3,\ \hat{u}_1$.

The calculations include position and velocity predictions using Verlet integration, cylinder chamber pressure predictions based on the mass flowrate model, motor speed predictions from the ARX model, and the predicted energy consumption for each prediction step. The optimal operating mode $u(t_k)$ is selected from the first element of U_{opt}. The prediction algorithm for DPC is as follows:

1) Set $i=0$.
2) Compute $t_i=t_k+i\cdot T_s$.
3) If $t_i=t_k$, then use:

$$\hat{P}_a(t_i)=P_a(t_k)$$
$$\hat{P}_b(t_i)=P_b(t_k)$$
$$\hat{n}_a(t_i)=n_a(t_k)$$
$$\hat{n}_b(t_i)=n_b(t_k)$$
$$\hat{y}(t_i)=y(t_k)$$
$$\hat{\dot{y}}(t_i)=(y(t_k)-y(t_k-T_s))/T_s$$

4) If $t_i=t_k+T_s$, then use:

$$\hat{P}_a(t_i)=\hat{P}_a(t_i-T_s)+T_s\hat{\dot{P}}_a(t_i-T_s)$$
$$\hat{P}_b(t_i)=\hat{P}_b(t_i-T_s)+T_s\hat{\dot{P}}_b(t_i-T_s)$$
$$\hat{y}(t_i)=\hat{y}(t_i-T_s)+T_s\hat{\dot{y}}(t_i-T_s)+\frac{1}{2}T_s^{\,2}\hat{\ddot{y}}(t_i-T_s)$$

If $t_i=t_k+T_s$, then use (3.5.2) and (3.5.3):

$$\hat{n}_a(t_i) = f_{arxa}(\hat{n}_a(t_i - T_s), \hat{n}_a(t_i - 2T_s), u_a(t_i - 2T_s))$$

$$\hat{n}_b(t_i) = f_{arxb}(\hat{n}_b(t_i - T_s), \hat{n}_b(t_i - 2T_s), u_b(t_i - 2T_s))$$

$$\hat{\dot{y}}(t_i) = \hat{\dot{y}}(t_i - T_s) + \frac{1}{2}T_s(\hat{\ddot{y}}(t_i - T_s) + \hat{\ddot{y}}(t_i - 2T_s))$$

If $t_i > t_k + T_s$, then use:

$$\hat{n}_a(t_i) = f_{arxa}(\hat{n}_a(t_i - T_s), \hat{n}_a(t_i - 2T_s), \hat{u}_a(t_i - 2T_s))$$

$$\hat{n}_b(t_i) = f_{arxb}(\hat{n}_b(t_i - T_s), \hat{n}_b(t_i - 2T_s), \hat{u}_b(t_i - 2T_s))$$

$$\hat{\dot{y}}(t_i) = \hat{\dot{y}}(t_i - T_s) + \frac{1}{2}T_s(\hat{\ddot{y}}(t_i - T_s) + \hat{\ddot{y}}(t_i - 2T_s))$$

5) Compute the predicted mass flowrates using (3.4.4), (3.5.13) and (3.5.14) as follows:

$$\hat{\dot{m}}_a(t_i) = \hat{\dot{m}}_{pA}(\hat{n}_a(t_i), \hat{P}_a(t_i)) - \hat{\dot{m}}_4(\hat{P}_a(t_i))$$

$$\hat{\dot{m}}_b(t_i) = \hat{\dot{m}}_{pB}(\hat{n}_b(t_i), \hat{P}_b(t_i)) - \hat{\dot{m}}_2(\hat{P}_b(t_i))$$

6) Compute the power and energy consumed by the pumps and valves using (3.4.5), (3.4.6), (3.5.17), (3.5.18), and (3.5.19) as follows:

$$p_p(t_i) = p_a(\hat{n}_a(t_i), \hat{P}_a(t_i)) + p_b(\hat{n}_b(t_i), \hat{P}_b(t_i))$$

$$p_v(t_i) = p_{iv1}(t_i) + p_{iv2}(t_i) + p_{ev1}(t_i) + p_{ev2}(t_i)$$

$$E_p(t_i) = p_p(t_i) * T_s$$

$$E_v(t_i) = p_v(t_i) * T_s$$

7) Compute the predicted pressure derivatives using (3.3.6) and (3.3.7) as follows:

$$\hat{\dot{P}}_a(t_i) = \frac{KRT\hat{\dot{m}}_a(t_i) - KA_a\hat{\dot{y}}(t_i)\hat{P}_a(t_i)}{A_a\hat{y}(t_i) + V_{a0}}$$

$$\hat{\dot{P}}_b(t_i) = \frac{KRT\hat{\dot{m}}_b(t_i) + KA_b\hat{\dot{y}}(t_i)\hat{P}_b(t_i)}{A_b(L - \hat{y}(t_i)) + V_{b0}}$$

8) Substitute $\hat{P}_a(t_i)$ and $\hat{P}_b(t_i)$ into (3.6.2) to obtain the predicted pneumatic force $\hat{F}_p(t_i)$.

9) Compute the predicted friction $\hat{F}_f(t_i)$ using (3.6.7).

10) Compute the predicted acceleration $\hat{\ddot{y}}(t_i)$ using (3.6.8).

11) Set $i = i + 1$.

12) If $i < N_p$, then go to Step 2.

13) Stop

4.2.3 Design of DVMPC3V for VC

Before the position tracking task starts, the air tank will be charged to 200 kPa by the pump, then DVMPC3V is used to choose the operating mode for switching the four valves to follow the setpoint. The cost function designed for the VC circuit is:

$$\begin{aligned} J &= \mathrm{PTEC} + \mathrm{ITAE} + \mathrm{PVEC} + \mathrm{PCVEC} \\ &= \sum_{i=1}^{N_p} \left((\hat{y}(t_i) - y_d(t_i))^2 + \omega_i \cdot i \cdot T_s \cdot \left| \hat{y}(t_i) - y_d(t_i) \right| + \omega_v \cdot E_v(t_i) + \omega_{cv} \cdot E_{cv}(t_i) \right) \end{aligned} \tag{4.2.7}$$

This cost function consists of four terms: two position cost terms and two energy cost terms. Including PTEC reduces the tracking errors, while ITAE helps reduce the steady state errors. ω_i and ω_{cv} are weighting coefficients for ITAE (Integral of Time-weighted Absolute Error) and PCVEC (Predicted Charge Valves Energy Cost) terms. The reason for including PCVEC in the cost function will now be explained. Compared to DPC, it is easier for VC to maintain the high chamber pressure level, because the charge valves connect the pressurized tank and chambers. In our hardware setup, the friction of the piston is small and the leakage of rod chamber side under high pressure is larger, so it is difficult for M_1 to hold the position constant in this situation, then the charging valves will have to be opened to compensate for the position error. Including PCVEC in the cost tends to limit the times of the charge valves opening and keeps the chambers at lower pressure levels, which also saves the energy.

The prediction equation for DVMCP3V is:

$$\begin{aligned} &\left[\hat{y}(t_i + T_s),\ \hat{\dot{y}}(t_i + T_s),\ \hat{P}_a(t_i + T_s),\ \hat{P}_b(t_i + T_s),\ \hat{P}_t(t_i + T_s),\ \hat{n}_a(t_i + T_s) \right] = \\ &f(\hat{u}(t_i),\ S_p(t_i),\ \hat{y}(t_i),\ \hat{\dot{y}}(t_i),\ \hat{P}_a(t_i),\ \hat{P}_b(t_i),\ \hat{P}_t(t_i), \ldots \\ &\quad \hat{n}_a(t_i),\ \hat{n}_a(t_i - T_s),\ \hat{u}_a(t_i - T_s)) \quad \forall i = 0,1,\ldots,N_p - 1 \end{aligned} \tag{4.2.8}$$

Compared with DVMPC3P, the main difference is for the long cycle tests, the algorithm should be capable to determine when to perform tank charging to avoid the tank pressure dropping too low. More importantly, the tank pressure during the charging should be well predicted so that the control performance could stay consistent during the charging period. Specifically, the VC takes the strategy to charge the air tank to 200 kPa first, then the DVMPC3V will determine the valves ON/OFF states to realize the position control task. A specific deadband is set to keep the air tank's pressure large enough to provide reliable tracking performance, and a binary switch, S_p, with initial value of 0, is used to monitor the tank pressure: when the tank pressure drops below 150 kPa, S_p is set to 1, and the pump starts working, while at the same time, the system is still expected to keep running with consistent high performance. The pump won't stop until the air tank pressure returns to 200 kPa, and S_p is changed back to 0. The prediction algorithm for the VC circuit is as follows:

1) Set $i = 0$.
2) Compute $t_i = t_k + i \cdot T_s$.
3) If $t_i = t_k$, then use:

$$\hat{P}_a(t_i) = P_a(t_k)$$

$$\hat{P}_b(t_i) = P_b(t_k)$$

$$\hat{y}(t_i) = y(t_k)$$

$$\hat{\dot{y}}(t_i) = (y(t_k) - y(t_k - T_s)) / T_s$$

If $S_p(t_i) = 1$, $\hat{n}_a(t_i) = n_a(t_k)$

4) If $t_i \geq t_k + T_s$, then use:

$$\hat{P}_a(t_i) = \hat{P}_a(t_i - T_s) + T_s \hat{\dot{P}}_a(t_i - T_s)$$

$$\hat{P}_b(t_i) = \hat{P}_b(t_i - T_s) + T_s \hat{\dot{P}}_b(t_i - T_s)$$

$$\hat{P}_t(t_i) = \hat{P}_t(t_i - T_s) + T_s \hat{\dot{P}}_t(t_i - T_s)$$

$$\hat{y}(t_i) = \hat{y}(t_i - T_s) + T_s \hat{\dot{y}}(t_i - T_s) + \frac{1}{2} T_s^2 \hat{\ddot{y}}(t_i - T_s)$$

If $t_i = t_k + T_s$, then use (3.5.2) for motor speed prediction when $S_p(t_i) = 1$:

$$\hat{\dot{y}}(t_i) = \hat{\dot{y}}(t_i - T_s) + \frac{1}{2} T_s (\hat{\ddot{y}}(t_i - T_s) + \ddot{y}(t_i - 2T_s))$$

$$\hat{n}_a(t_i) = f_{arxa}(\hat{n}_a(t_i - T_s), \hat{n}_a(t_i - 2T_s), u_a(t_i - 2T_s))$$

If $t_i > t_k + T_s$, then use (3.5.2) for motor speed prediction when $S_p(t_i) = 1$:

$$\hat{\dot{y}}(t_i) = \hat{\dot{y}}(t_i - T_s) + \frac{1}{2} T_s (\hat{\ddot{y}}(t_i - T_s) + \hat{\ddot{y}}(t_i - 2T_s))$$

$$\hat{n}_a(t_i) = f_{arxa}(\hat{n}_a(t_i - T_s), \hat{n}_a(t_i - 2T_s), \hat{u}_a(t_i - 2T_s))$$

5) Compute the predicted mass flowrate using (3.3.10), (3.4.4) and (3.6.7):

$$\hat{\dot{m}}_a(t_i) = \hat{\dot{m}}_3(\hat{P}_t(t_i), \hat{P}_a(t_i)) - \hat{\dot{m}}_4(\hat{P}_a(t_i))$$

$$\hat{\dot{m}}_b(t_i) = \hat{\dot{m}}_1(\hat{P}_t(t_i), \hat{P}_b(t_i)) - \hat{\dot{m}}_2(\hat{P}_b(t_i))$$

$$\hat{\dot{m}}_t(t_i) = \begin{cases} -(\hat{\dot{m}}_3(\hat{P}_t(t_i), \hat{P}_a(t_i)) + \hat{\dot{m}}_1(\hat{P}_t(t_i), \hat{P}_b(t_i))) & if \;\; W_{\dot{m}_t}(t_i) = 1 \\ \hat{\dot{m}}_{pA}(\hat{n}_a(t_i), \hat{P}_t(t_i)) - (\hat{\dot{m}}_3(\hat{P}_t(t_i), \hat{P}_a(t_i)) + \hat{\dot{m}}_1(\hat{P}_t(t_i), \hat{P}_b(t_i))) & if \;\; W_{\dot{m}_t}(t_i) = 2 \\ 0 & \text{else} \end{cases}$$

6) Compute the energy consumed by all the valves and charge valves using (3.4.5), (3.4.6) and (3.4.7):

$$p_v(t_i) = p_{iv1}(t_i) + p_{iv2}(t_i) + p_{ev1}(t_i) + p_{ev2}(t_i)$$

$$p_{cv}(t_i) = p_{cv1}(t_i) + p_{cv2}(t_i)$$

$$E_v(t_i) = p_v(t_i) * T_s$$

$$E_{cv}(t_i) = p_{cv}(t_i) * T_s$$

7) Compute the predicted pressure derivatives using (3.3.6), (3.3.7) and (3.3.9):

$$\hat{\dot{P}}_a(t_i) = \frac{KRT\hat{\dot{m}}_a(t_i) - KA_a\hat{\dot{y}}(t_i)\hat{P}_a(t_i)}{A_a\hat{y}(t_i) + V_{a0}}$$

$$\hat{\dot{P}}_b(t_i) = \frac{KRT\hat{\dot{m}}_b(t_i) + KA_b\hat{\dot{y}}(t_i)\hat{P}_b(t_i)}{A_b(L - \hat{y}(t_i)) + V_{b0}}$$

$$\hat{\dot{P}}_{\mathrm{t}}(t_i)=\begin{cases}\dfrac{KRT\hat{\dot{m}}_t(t_i)-KA_a\hat{\dot{y}}(t_i)\hat{P}_a(t_i)}{A_a\hat{y}(t_i)+V_{a0}+V_{\mathrm{t}}+V_{t0}} & \text{if } \mathrm{W}_{\dot{\mathrm{P}}_{\mathrm{t}}}(t_i)=1\\ \dfrac{KRT\hat{\dot{m}}_t(t_i)+KA_b\hat{\dot{y}}(t_i)\hat{P}_b(t_i)}{A_b(L-\hat{y}(t_i))+V_{b0}+V_{\mathrm{t}}+V_{t0}} & \text{if } \mathrm{W}_{\dot{\mathrm{P}}_{\mathrm{t}}}(t_i)=2\\ \dfrac{KRT\hat{\dot{m}}_t(t_i)}{V_{\mathrm{t}}+V_{t0}} & \text{if } \mathrm{W}_{\dot{\mathrm{P}}_{\mathrm{t}}}(t_i)=3\\ 0 & \text{else}\end{cases}$$

8) Substitute $\hat{P}_a(t_i)$ and $\hat{P}_b(t_i)$ into (3.6.2) to obtain the predicted pneumatic force $\hat{F}_p(t_i)$.

9) Compute the predicted friction $\hat{F}_f(t_i)$ using (3.6.7).

10) Compute the predicted acceleration $\hat{\ddot{y}}(t_i)$ using (3.6.8).

11) Set $i=i+1$.

12) If $i<N_p$, then go to Step 2.

13) Stop

4.3 Summary

In this chapter, the potential advantages of employing DVMPC algorithms for pneumatic systems and the feasibility of implementing real-time DVMPC were discussed first. Next, the selection of the operating modes and the partitioning method chosen for the prediction horizon were presented. Lastly, modified versions of DVMPC for the DPC and VC circuits, named DVMPC3P and DVMPC3V, respectively, were proposed. The DVMPC3P and DVMPC3V algorithms will be evaluated experimentally in the next chapter.

Chapter 5 - Experiments

5.1 Introduction

In this chapter, DVMPC3P and DVMPC3V are experimentally tested on the DPC and VC circuits, respectively. The designed setpoint trajectory for controller testing and the performance metrics used in this research are introduced first. Next, the effects of the controller parameters on the performances of DPC and VC circuits are discussed in Sections 5.3 and 5.4, respectively. Finally, long duration tests are performed to comprehensively compare how well the controllers balance the position control accuracy and energy saving objectives. The testing procedure, results and discussion are presented in Section 5.5. Conclusions are drawn in Section 5.6.

5.2 Experimental setting

The designed setpoint trajectory shown in Figure 5.2.1 which consists of a step change and two cycloidal curves is designed to test the controllers' performances under both dynamic and steady state conditions. The 30 mm step change occurs at 0.25 s, followed by a dwell that lasts 1.25 s. It is followed by a 70 mm cycloidal curve with a 2 Hz frequency. Next, the setpoint dwells at 100 mm for 1 s, before another 2 Hz cycloidal curve brings it back to the 30 mm position, were it dwells for another 1 s. This sequence of rising cycloidal curve, dwell, falling cycloidal curve, and 2nd dwell is named "cycloidal curve pattern". Next, the cycloidal curve pattern is repeated, to complete the trajectory. For the long duration test, the cycloidal curve pattern is repeated over a longer period, as further explained in Section 5.5.

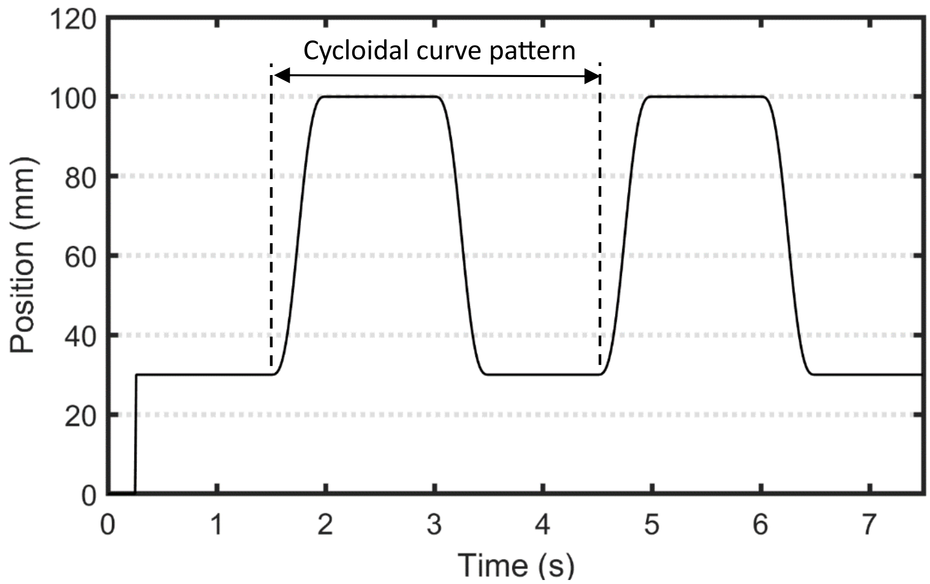

Figure 5.2.1 The designed setpoint trajectory that includes an initial step change, followed by a 1.25 s dwell, and two cycloidal curve patterns.

5.3 Performance metrics

The performance metrics used in this research to make quantitative comparisons are defined as follows:

Root Mean Square Error (RMSE) analyzes the error between the desired payload position and the actual position. It is given by:

$$RMSE = \sqrt{\frac{1}{n}\sum_{k=1}^{n}(y(t_k) - y_d(t_k))^2} \tag{5.3.1}$$

where n is the number of data points.

Mean Absolute Error (MAE) is also used to evaluate the error between the setpoint payload position and the actual position. MAE is less sensitive to large errors than RMSE.

$$MAE = \frac{1}{n}\sum_{i=1}^{n}\left|y(t_k) - y_d(t_k)\right| \tag{5.3.2}$$

Steady State Error (SSE) is defined as the difference between the setpoint's steady state position and the actual steady state position. As mentioned before, the pneumatic cylinder used for research features very low friction. Only a 10 kPa pressure difference between the chambers can produce a pneumatic force larger than the static friction along the guide. At the same time, the rod chamber (chamber B) has leaking issue due to the slip fit rod sealing. These factors might cause the problem, especially in the case when the chamber pressures are higher than atmospheric pressure, the pressure difference caused by leakage makes the payload move slightly during the 1 s dwell periods despite all the valves and pump being closed. Hence, five SSE data, named SSE1 to SSE5, were collected by integration from the time windows of 1.1 - 1.4 s, 2.6 - 2.9 s, 4.1 - 4.4 s, 5.6 - 5.9 s, and 7.1 - 7.4 s. If the mentioned leakage situation happens, and the data will be marked with " ** ". If it takes system longer time to reach steady state, then the integration time window will be narrowed to 1.3 - 1.4 s, 2.8 - 2.9 s, 4.3 - 4.4 s, 5.8 - 5.9 s, 7.3 - 7.4 s and the data are marked with " * ". Particularly, for these type data with leakage influence, the mark "+" will be used instead. Finally, for the situation where the system fails to reach steady state, it directly shows the sign " # ". The mean value of steady state errors (MSSE) of SSE1 to SSE5 will also be reported.

Overshoot (OS) is defined as the peak value relative to the steady state value of the position in the length unit of mm. OS1 to OS5 are the five values from the step response, and the responses to the four increasing/decreasing cycloidal curves. MOS is the mean absolute value of OS1 to OS5.

Standard deviation of the SSE (SDSSE): In this thesis, we use SDSSE to evaluate the repeatability of the steady state performances of DVMPC3P and DVMPC3V in the long duration experiments. It is given by:

$$SDSSE = \sqrt{\frac{1}{m}\sum_{i=1}^{m}(x_i - \bar{x})^2} \tag{5.3.3}$$

where x is the element in SSE array from the long duration experiments. $\bar{x}$ is the mean value of SSE array, and m is the number of SSE in the array.

Start time is defined as the moment when the control mode first switches from M_1 when it reaches to 30 mm step change. It is used to evaluate how fast the controller responses to the future setpoint.

Settling time is defined as the difference between the start time and the time when the measured position first stops changing after the 30 mm step change. This metric is used to assess how long it takes for the controller to bring the system to steady state. It should be noted that this is not the traditional definition of settling time.

Pump energy consumption is calculated by the numerically integrating the power consumption of the pump(s) (which equals the product of the measured current(s) and voltage(s)).

Valve energy consumption is calculated by the numerically integrating the power consumption of the valves (which equals the product of the measured current and voltage).

System energy consumption is the sum of the pump energy and valve energy consumptions for the test.

5.4 DPC with DVMPC3P

Totally six tests with the DPC circuit were conducted to study the effects of the controller parameters on the system's performance. Specifically, the first four tests only have position-related terms in the cost function. The value of N_p was equal to 6 in the PTest1 to Test3, while the values of N_m used were 1, 2 and 3, respectively. Based on the PTest3 result, the N_{delta} in PTest4 is extended from 2 to 3, which leads to a longer prediction horizon of 9 steps. PTest5 and PTest6 are the energy saving version of the PTest3 and PTest4, in which the ω_{bi} , ω_v , and ω_p were tuned correspondingly to attain the satisfactory control performance. The parameters used in the tests are listed in Table 5.4.1. The SSE results are shown in Table 5.4.2. The OS results are shown in Table 5.4.3. The RMSE, MAE, start time and settling time are shown in Table 5.4.4, and the energy consumption results are shown in Table 5.4.5. The complete experimental results are presented in Figures 5.4.1 to 5.4.6. The time responses of the payload position, position error, cylinder chamber pressure, motor speed and operating modes are plotted in each figure.

Table 5.4.1 The values of the DVMPC3P parameters used in the DPC tests.

Test name	N_p	N_m	N_{delta}	ω_{bi}	ω_v	ω_p
PTest1	6	1	6	1.0	0	0
PTest2	6	2	3	1.0	0	0
PTest3	6	3	2	0.7	0	0
PTest4	9	3	3	1.0	0	0
PTest5	6	3	2	0.45	1.7e-4	9.0e-5
PTest6	9	3	3	0.50	1.8e-3	1.3e-4

Table 5.4.2 Comparisons of SSE values (mm) from the DPC tests.

Test name	SSE1	SSE2	SSE3	SSE4	SSE5	MSSE
PTest1	-1.30	0.47	0	0.53	0.14	0.49
PTest2	0.22*	0.24**	0.14	1.02	-0.01	0.31
PTest3	0.01+	-0.10	0.12*	0.03*	0.28	0.11
PTest4	-0.01*	0.24	1.79**	1.30	-0.07*	0.68
PTest5	-0.28	-0.10	-0.35	0.33	-0.28	0.27
PTest6	-1.69	0.45	0.08	-1.57	1.23	1.00

Table 5.4.3 Comparisons of OS values (mm) from the DPC tests.

Test name	OS1	OS2	OS3	OS4	OS5	MOS
PTest1	2.08	0.02	2.09	4.41	3.26	2.37
PTest2	4.88	4.40	2.54	3.67	4.22	3.94
PTest3	8.10	11.20	3.37	7.97	7.46	7.62

PTest4	2.55	1.45	6.03	5.30	5.61	4.19
PTest5	4.06	0.41	2.40	0.03	2.75	1.93
PTest6	2.10	2.56	4.01	0.03	1.60	2.06

Table 5.4.4 Comparisons of position control performance metrics from the DPC tests.

Test name	RMSE (mm)	MAE (mm)	MSSE (mm)	MOS (mm)	Start time (s)	Settling time (s)
PTest1	5.24	2.08	0.49	2.37	0.22	0.64
PTest2	4.69	1.96	0.31	3.94	0.19	0.93
PTest3	6.84	2.80	0.11	7.62	0.18	1.12
PTest4	6.13	2.73	0.68	4.19	0.16	0.85
PTest5	4.22	1.56	0.27	1.93	0.22	0.84
PTest6	5.25	2.45	1.00	2.06	0.22	0.74

Table 5.4.5 Comparisons of energy consumption from the DPC tests.

Test name	Pump energy consumption(J)	Valve energy consumption(J)	System energy consumption(J)
PTest1	51.90	11.23	63.13
PTest2	91.14	12.16	103.30
PTest3	149.88	11.04	160.92
PTest4	125.38	16.38	141.76
PTest5	47.57	4.67	52.24
PTest6	45.85	3.86	49.71

From the PTest1 ~ Ptest3, it is found that with the same length of prediction horizon (N_p = 6), a smaller N_{delta} contributes to a more aggressive controller (i.e., one that switches modes frequently), while a larger N_{delta} will make the control strategy become conservative. In PTest1, the SSE1 for the step response is -1.30 mm, and the averaged SSE, 0.49 mm, is also the peak value among the three tests. As a contrast, the averaged SSE in PTest3 is only 0.11 mm. This is because N_{delta} basically represents the temporal resolution of control action in each move. For example, under mode M_2, the pump is kept ON for the following 6 prediction steps (at a minimum) in PTest1 since N_{delta} = 6, while it will only be ON for 2 steps (at a minimum) in PTest3 since it used N_{delta} = 2. If the predictions tell DVMPC3P that the cost of moving the payload is larger than not moving it, then a large SSE will be produced, like it was with PTest1.

However, the positive aspect of a larger N_{delta} is since the system is less sensitive to the SSE, it is less likely to make fine adjustments, and this reduces the mode switching frequency dramatically. For example, although the system has the capability to attain the minimum MSSE due to N_{delta}=2 in PTest3, with ω_{bi} decreased from 1 to 0.7 to suppress the error integration action, both RMSE and MAE are still the largest among the 3 tests because of the evident overshoots and small oscillation during the test. In contrast, the OS results from PTest1 are generally lower than PTest2 and PTest3's. The average OS is 2.37 mm, around 69% lower than the result from PTest3. The operating mode transition subplots in Figure 5.4.1 - Figure 5.4.3 also clearly show that the modes change more frequently in PTest3.

Based on the above findings, if N_p is a fixed value, larger N_{delta} will reduce the oscillations and MOS, while smaller N_{delta} will produce smaller MSSE. A compromise option is to choose the moderate N_{delta} value between the two extremes, as PTest2 did, to achieve a balance among those control performance metrics.

PTest4 was designed to be compared with PTest2 and PTest3. In theory, with the proper N_{delta}, if all the involved models are accurate enough and computational power is not a concern, then the larger N_m helps to extend the prediction horizon, which might improve the optimality of the control solution. However, both MSSE and MOS from the PTest4 are larger than those from PTest2. Since all the tests were able to run in real-time, it is assumed that it is the limited modeling accuracy when predicting farther into the future that constrains the control performance instead of the computation time in our research, so the system doesn't necessarily have better position control performance with a larger prediction horizon. It is also interesting that, unlike the other DPC tests, the chamber pressures in PTest4 during 3.5 - 4.5 s are kept at a relatively high level, over 260 kPa. Although there is apparent position error in the following increasing cycloidal curve, the system could still reach the steady state quickly after 5.41s.

It can also be observed that as we extended the prediction horizon, the system started to respond to the approaching step change earlier. With $N_p = 9$ in PTest4, the recorded moment for the first mode change is 0.16 s and the leading mode is M_3 that allows the chamber B charging. This is because M_3 keeps the position error equal to zero during the initial section of the prediction horizon, and also provides a preload pneumatic force to prevent the large OS in the latter portion of the horizon. By adding the predicted energy consumption to the cost function, the control actions of PTest5 and PTest6 both transition to M_2 at 0.22 s and the controller tends to switch between M_2 and M_4 to moderate the chamber pressures and avoid OS. As the results in Table 5.4.4 show, there was no clear relationship between the settling time and the DVMPC3P parameters.

Regarding the energy consumption, PTest3 consumed totally 160.92 J energy (93.14% by the pumps, and 6.86% by the valves), while 141.76 J was used in PTest4 (88.45% by the pump, and 11.55% by the valves). After adding the energy consumption terms to the cost function (by setting $\omega_{bi} = 0.45$, $\omega_v = 1.7 \times 10^{-4}$, $\omega_p = 9.0 \times 10^{-5}$), the energy consumption was reduced by ~68%. Specifically, 52.24 J energy was consumed in PTest5. Moreover, compared with the aggressive controller behaviors observed in PTest3, apart from the slight derating of the SSE performance, the RMSE and MAE were improved by 2.62 mm and 1.24 mm. The MOS is 1.93 mm, only ~1/4 of the result from PTest3. The system also reached steady state 0.28 s faster than before. Similar improvement trends could be observed in PTest6, compared with PTest4. Although PTest6 saved 4.84% more energy, its position control performance is inferior to PTest5, so the parameter values used in PTest5 produced the best performance for DPC among the 6 tests, and these parameters will be used for long duration test presented in Section 5.6.

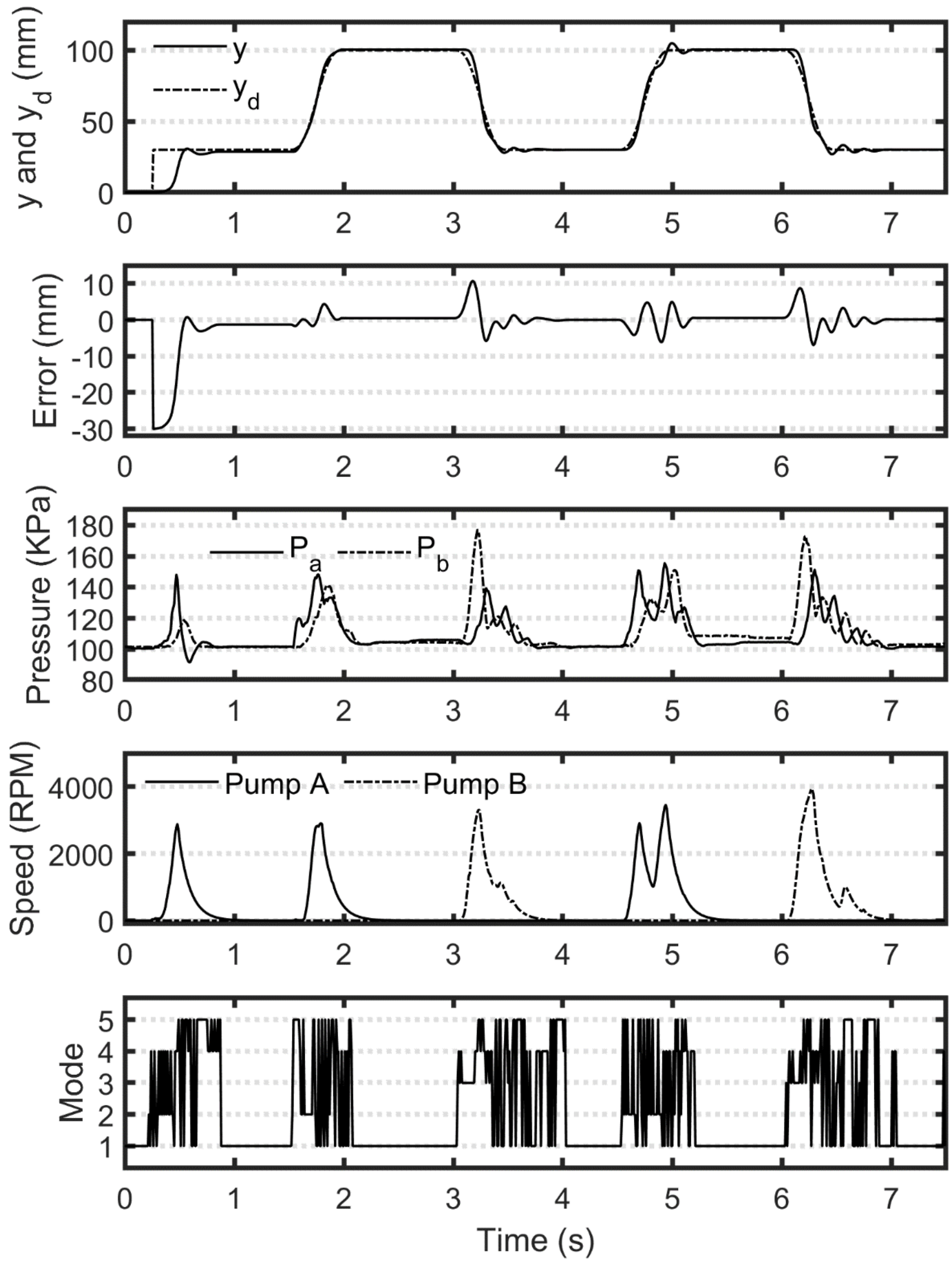

Figure 5.4.1 DPC experimental results with

$N_p = 6,\ N_m = 1,\ N_{delta} = 6,\ \omega_{bi} = 1.0,\ \omega_v = 0,\ \omega_p = 0.$

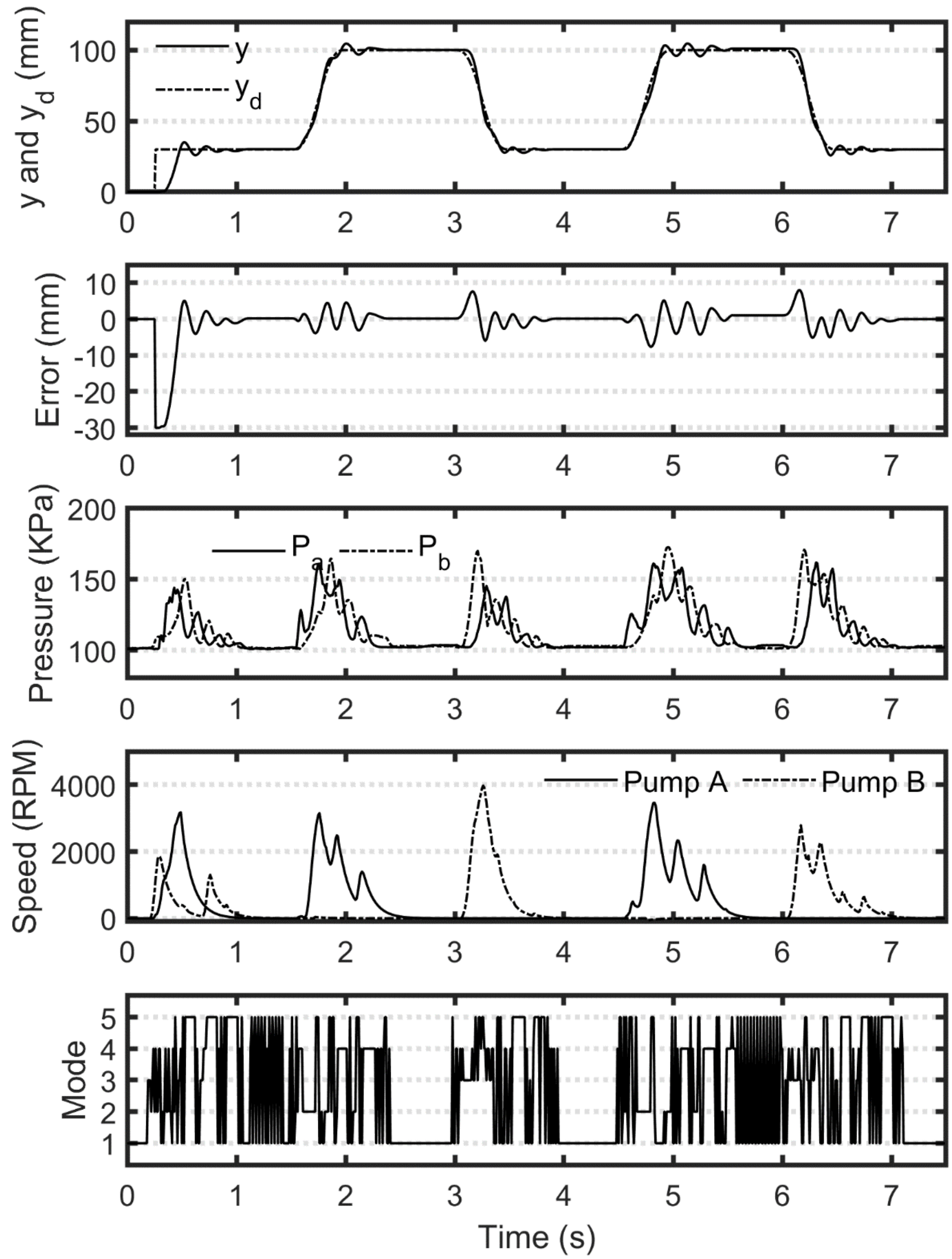

Figure 5.4.2 DPC experimental results with
$N_p = 6,\ N_m = 2,\ N_{delta} = 3,\ \omega_{bi} = 1.0,\ \omega_v = 0,\ \omega_p = 0$.

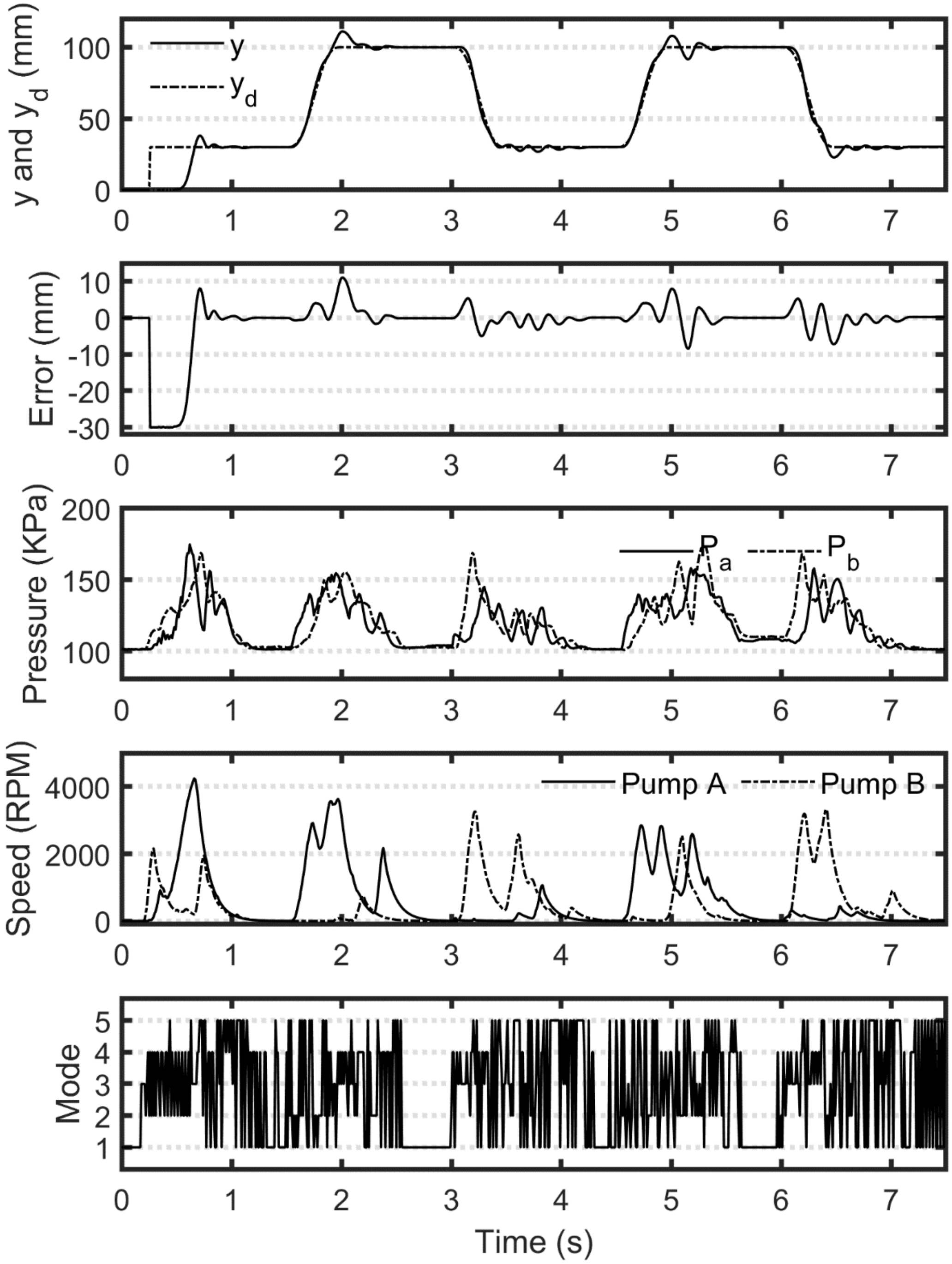

Figure 5.4.3 DPC experimental results with

$N_p = 6,\ N_m = 3,\ N_{delta} = 2,\ \omega_{bi} = 0.7,\ \omega_v = 0,\ \omega_p = 0$.

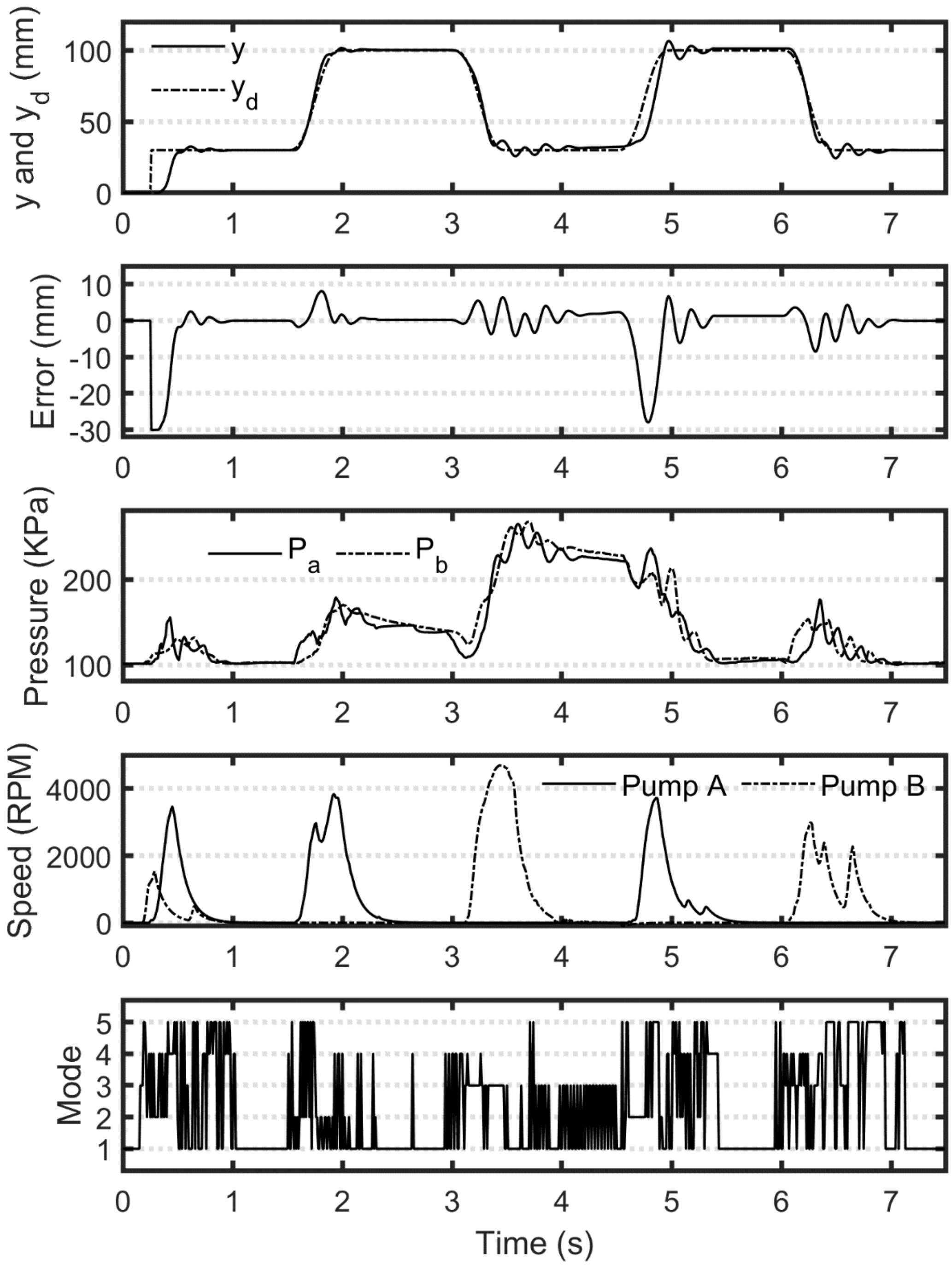

Figure 5.4.4 DPC experimental results with

$N_p = 9,\ N_m = 3,\ N_{delta} = 3,\ \omega_{bi} = 1.0,\ \omega_v = 0,\ \omega_p = 0$.

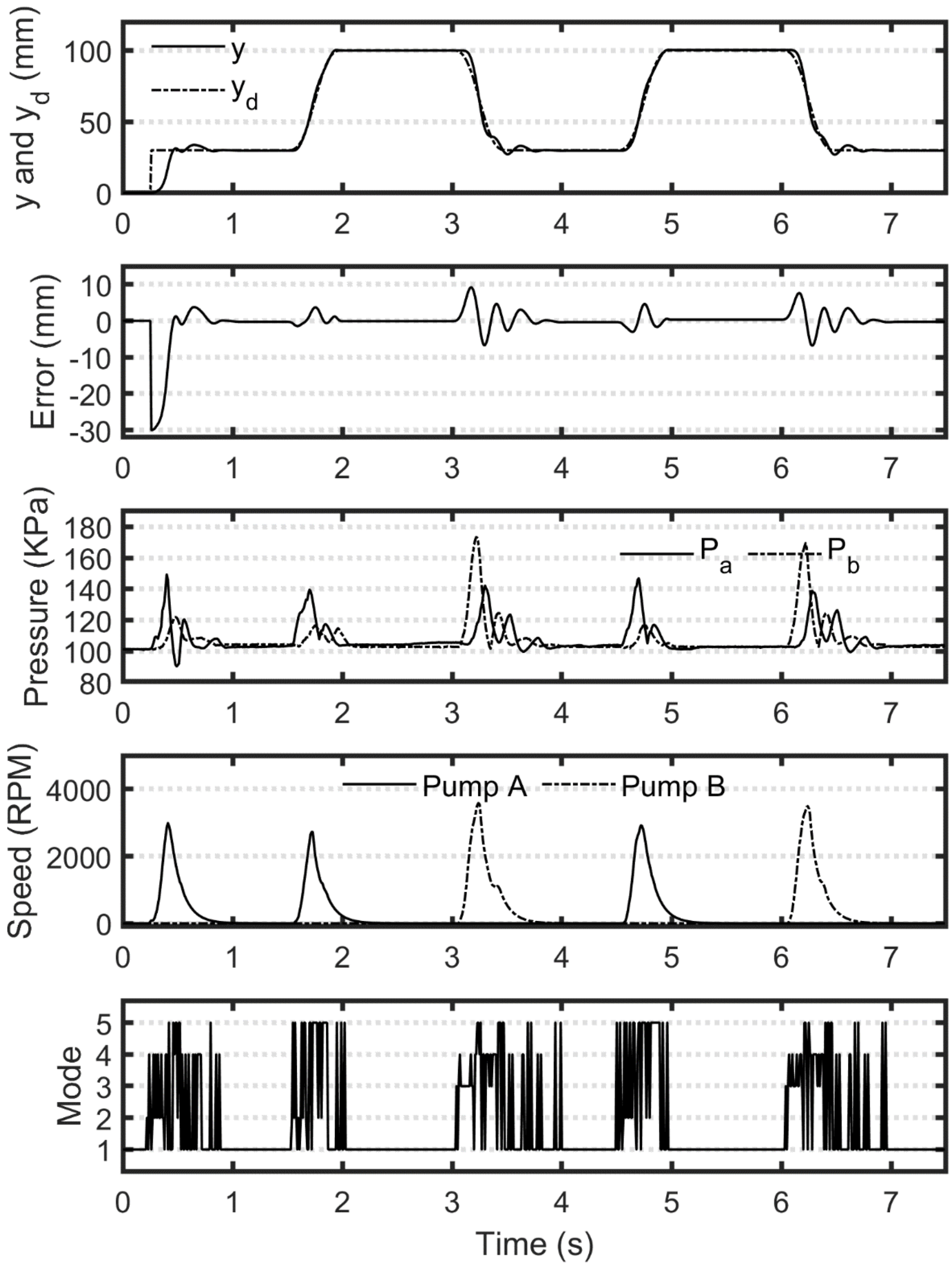

Figure 5.4.5 DPC experimental results with

$N_p = 6,\ N_m = 3,\ N_{delta} = 2,\ \omega_{bi} = 0.45,\ \omega_v = 1.7\times10^{-4},\ \omega_p = 9.0\times10^{-5}$.

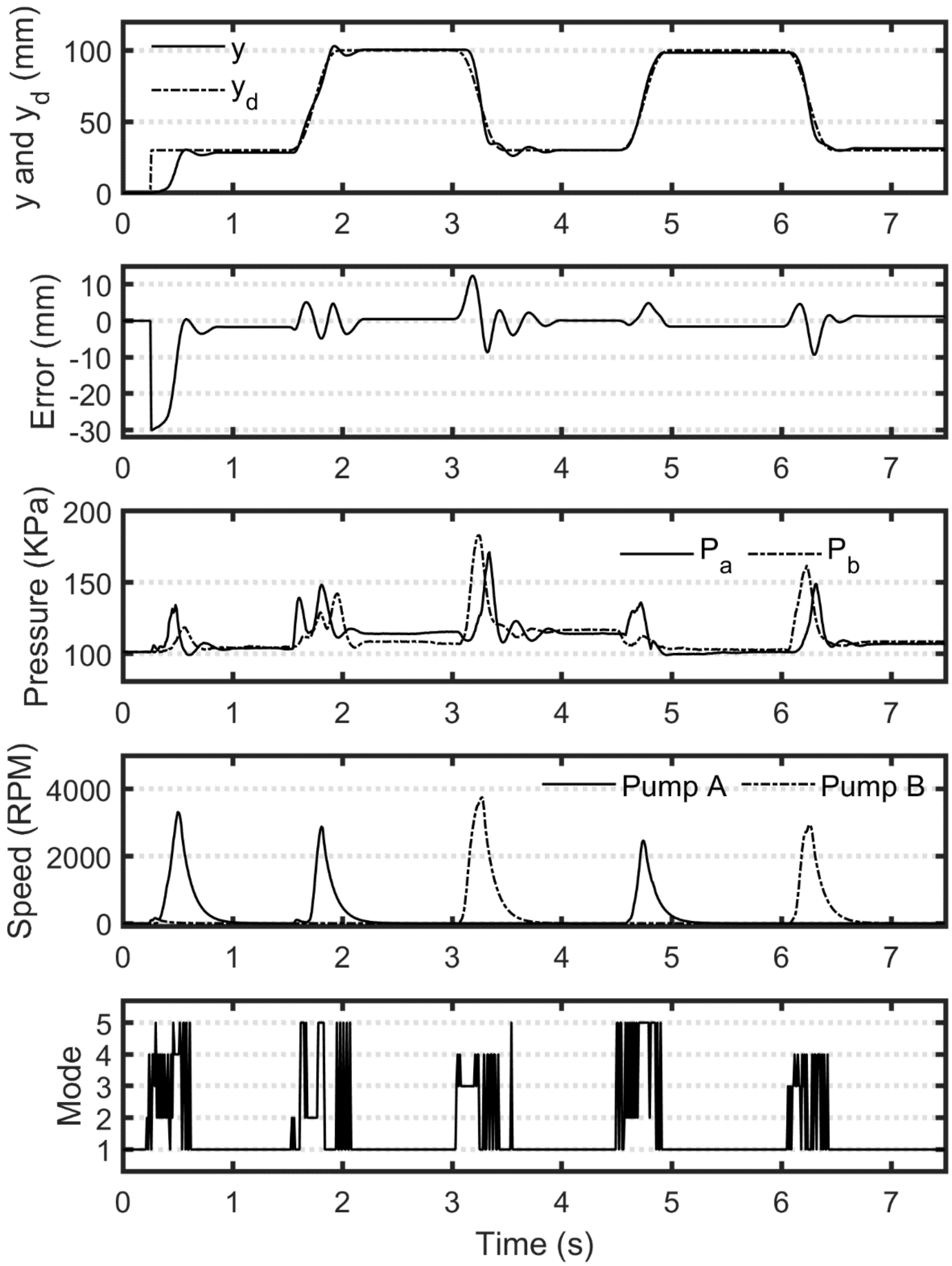

Figure 5.4.6 DPC experimental results with

$N_p = 9,\ N_m = 3,\ N_{delta} = 3,\ \omega_{bi} = 0.50,\ \omega_v = 1.8\times10^{-3},\ \omega_p = 1.3\times10^{-4}$.

5.5 VC with DVMPC3V

As in Section 5.4, six tests were conducted with the VC circuit to study the effects of the controller parameters on the system's performance. The first four tests were implemented with only the position-related terms in the cost function. PTest5 and PTest6 are the energy saving versions of PTest3 and PTest4, in which the energy consumption weight coefficients ω_v and ω_{cv} were tuned to save energy while attaining satisfactory control performance. The values of the parameters used in the tests are listed in Table 5.5.1. The SSE results are shown in Table 5.5.2. The OS results are shown in Table 5.5.3. The RMSE, MAE, start time and settling time are shown in Table 5.5.4, and the energy consumption results are shown in Table 5.5.5. The complete experimental results are presented from Figures 5.5.1 to Figure 5.5.6. The time responses of the payload position, position error, cylinder chamber pressure, air tank pressure and operating modes are plotted in each figure.

Table 5.5.1 The values of the DVMPC3V parameters used in the VC tests.

Test name	N_p	N_m	N_{delta}	ω_i	ω_v	ω_{cv}
VTest1	6	1	6	1.0	0	0
VTest2	6	2	3	1.0	0	0
VTest3	6	3	2	1.0	0	0
VTest4	9	3	3	1.0	0	0
VTest5	6	3	2	1.0	1.0e-12	4.0e-3
VTest6	9	3	3	1.0	0	1.5e-3

Table 5.5.2 Comparisons of SSE values (mm) from the VC tests.

Test name	SSE1	SSE2	SSE3	SSE4	SSE5	MSSE
VTest1	-0.59	0.48	2.97	0.49	0.67	1.04
VTest2	0.54**	-0.08	-0.26	-0.07	-0.27	0.24

VTest3	#	0**	#	0.27	#	0.14
VTest4	-0.16	0.38	-0.10	0.63	-0.26	0.31
VTest5	-0.20	-0.13	-0.16	-0.40	-0.24	0.23
VTest6	0.37	-0.56	0.37	0.73	-0.18**	0.44

Table 5.5.3 Comparisons of OS values (mm) from the VC tests.

Test name	OS1	OS2	OS3	OS4	OS5	MOS
VTest1	2.58	0.02	0.29	0.15	2.27	1.06
VTest2	0.55	1.59	1.39	0.95	2.92	1.48
VTest3	#	2.33	#	0.01	#	1.17
VTest4	1.64	0.00	2.01	0.03	1.85	1.11
VTest5	2.71	0.61	1.60	0.48	1.20	1.32
VTest6	1.52	0.02	1.48	0.03	0.44	0.70

Table 5.5.4 Comparisons of position control performance metrics from the VC tests.

Test name	RMSE (mm)	MAE (mm)	MSSE (mm)	MOS (mm)	Start time (s)	Settling time (s)
VTest1	2.17	1.48	1.04	1.06	0.19	0.53
VTest2	1.83	1.04	0.24	1.48	0.19	0.77
VTest3	1.82	1.14	0.14	1.17	0.19	#
VTest4	2.36	1.22	0.31	1.11	0.17	0.83
VTest5	1.61	0.83	0.23	1.32	0.19	0.64
VTest6	2.50	1.32	0.44	0.70	0.17	0.32

Table 5.5.5 Comparisons of energy consumption from the VC tests.

Test name	Pump energy consumption(J)	Valve energy consumption(J)	System energy consumption(J)
VTest1	408	8.89	416.89
VTest2	401.06	8.56	409.62
VTest3	416.50	13.02	429.52
VTest4	423.96	6.24	430.20
VTest5	409.26	5.90	415.16
VTest6	411.88	5.79	417.67

In VTest1 ~ VTest3, VTest1 had the largest MSSE of 1.04 mm. The chamber B leakage issue is more obvious with these VC results since their chamber pressures are higher than with DPC. For example, in Figure 5.5.1, during the 2 – 3 s interval, when the chamber B pressure drops slowly, the controller opened EV1 briefly four times to reduce chamber A pressure to keep the carriage at the desired position. Similar behaviors can be observed at the following dwell sections. However, the controller doesn't compensate for the steady state error well, for example, large SSE3 of 2.97 mm is recoded in VTest1. The situation improved for smaller N_{delta} values. When it was decreased from 6 to 3 and 2, the averaged SSE of VTest2 and VTest3 were reduced by 76.92% and 86.54% compared with VTest1.

It is noticeable that VTest3 failed to reach the steady state at all three 30 mm setpoint dwells. The mode switching was very frequent and both chamber A and chamber B pressure oscillated a lot, which caused the carriage position to chatter. That is the reason why corresponding SSE and OS data are absent from Tables 5.5.2 and 5.5.3. This proves again that using $N_{delta} = 2$ is too aggressive for application, unless other constraints are being applied. Regarding the OS, none of the values exceeded 3 mm from these three tests, and the MOS are all below 1.5 mm.

Comparing VTest4 and VTest2 results, increasing N_{delta} from 2 to 3 caused the position response to become less oscillatory. The MOS of VTest4 is 1.11 mm, around 25% less than that of VTest2. The other performance metrics, RMSE, MAE and MSSE are slightly better with VTest2 than with VTest4.

Since the direct air source for the VC circuit is air tank, the change of tank pressure could also reflect the air consumption to a certain extent. The tank pressure drop in VTest3 was the largest, reaching 45 kPa, which is nearly 3 times the value of the other tests. This was mainly caused by frequent mode switching that occurred with VTest3 to compensate for the steady state error.

In all of the VC tests, the carriage started moving before the setpoint step change occurred at 0.25 s which is typical for MPC. The start time of VTest1 ~ VTest3 are 0.19 s, and VTest4 and VTest6 have the earliest start times of 0.17 s, which is attributed to them using longest prediction horizon of 9 steps. It takes VTest6 0.32 s to reach the steady state, followed by the second place, 0.53 s from VTest1. For the rest of tests that reached steady state, the settling times were all less than 0.85 s.

With the energy consumption terms included in the cost function, 7.12 J of valve energy consumption was saved in VTest5, which is around 54.69% lower than that of VTest3. Comparing VTest6 and VTest4, VTest6 consumes 7.21% less valve energy than VTest4. The negative consequence is the RMSE, MAE, MSSE are 5.93%, 8.20%, 41.94% larger than those in VTest4.

The system energy consumptions with the VC tests were much larger than with the DPC tests. The reason is the large amount of energy consumed to charge the pump initially, before the carriage can begin moving with the VC circuit. However, with the VC circuit, each tank charging could support multiple repetitions of the carriage being controlled to follow the cycloidal curve pattern before the pump must be used to replenish the tank, so the results from these 7.5 s duration experiments are insufficient to compare the energy consumptions of the DPC and VC circuits. For this reason, long duration experiments, that include several tank pressure replenishments, will be conducted to compare the system energy consumption and position control performance with the DPC circuit in a fairer manner. The procedure, results and discussion of the long duration tests will be presented in Section 5.6.

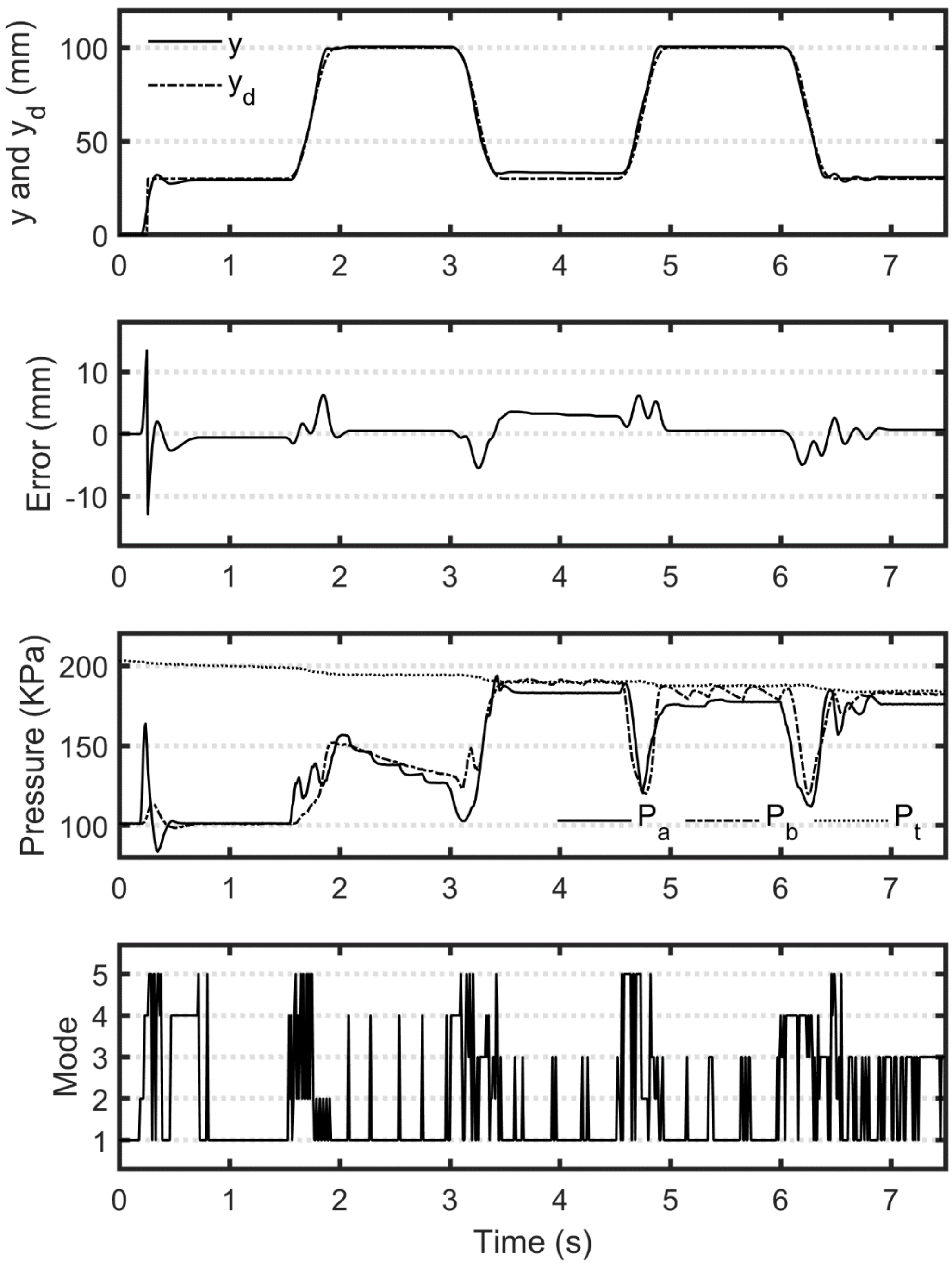

Figure 5.5.1 VC experimental results with

$N_p = 6,\ N_m = 1,\ N_{delta} = 6,\ \omega_i = 1.0,\ \omega_v = 0,\ \omega_{cv} = 0$.

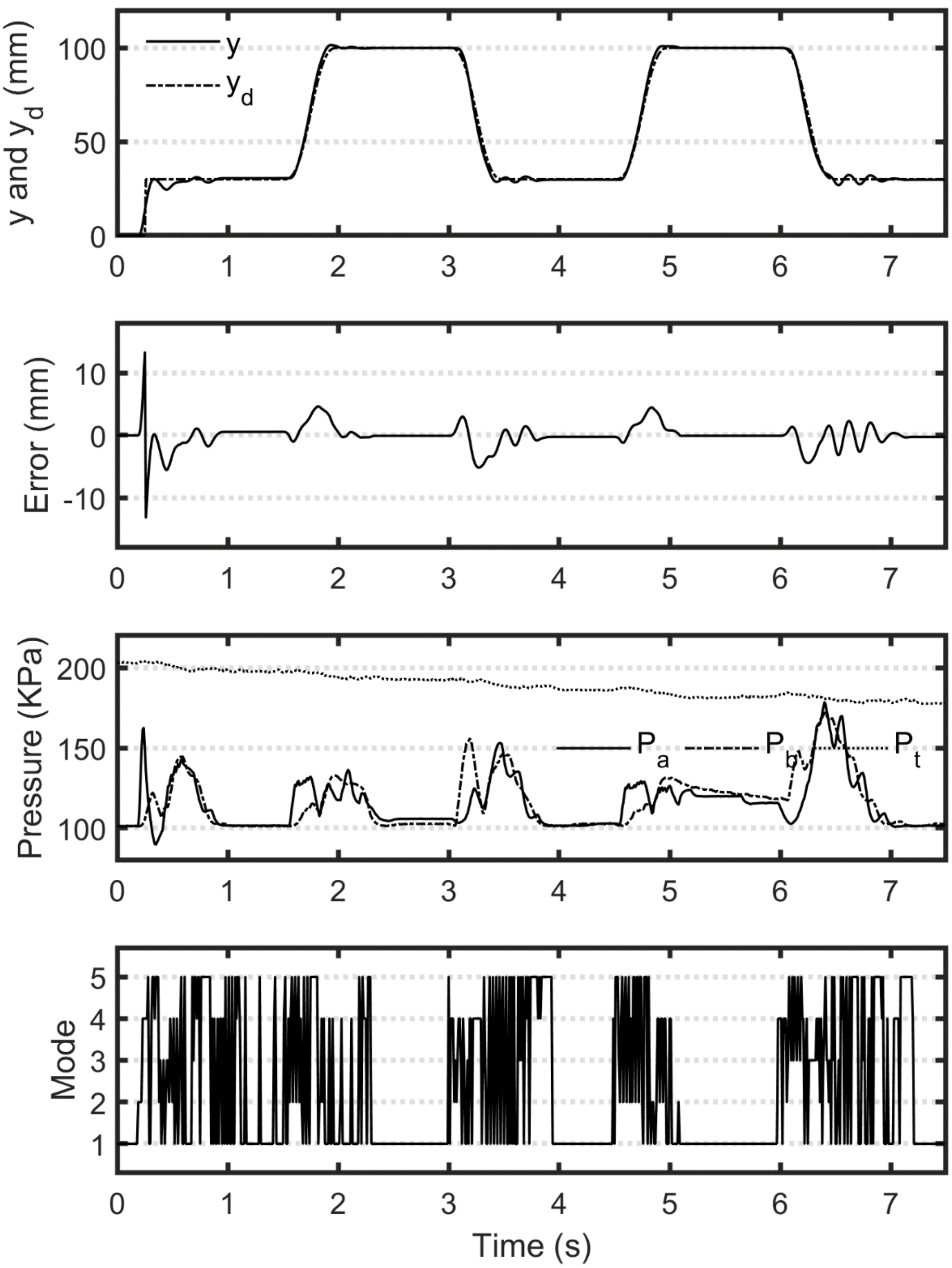

Figure 5.5.2 VC experimental results with

$N_p = 6,\ N_m = 2,\ N_{delta} = 3,\ \omega_i = 1.0,\ \omega_v = 0,\ \omega_{cv} = 0$.

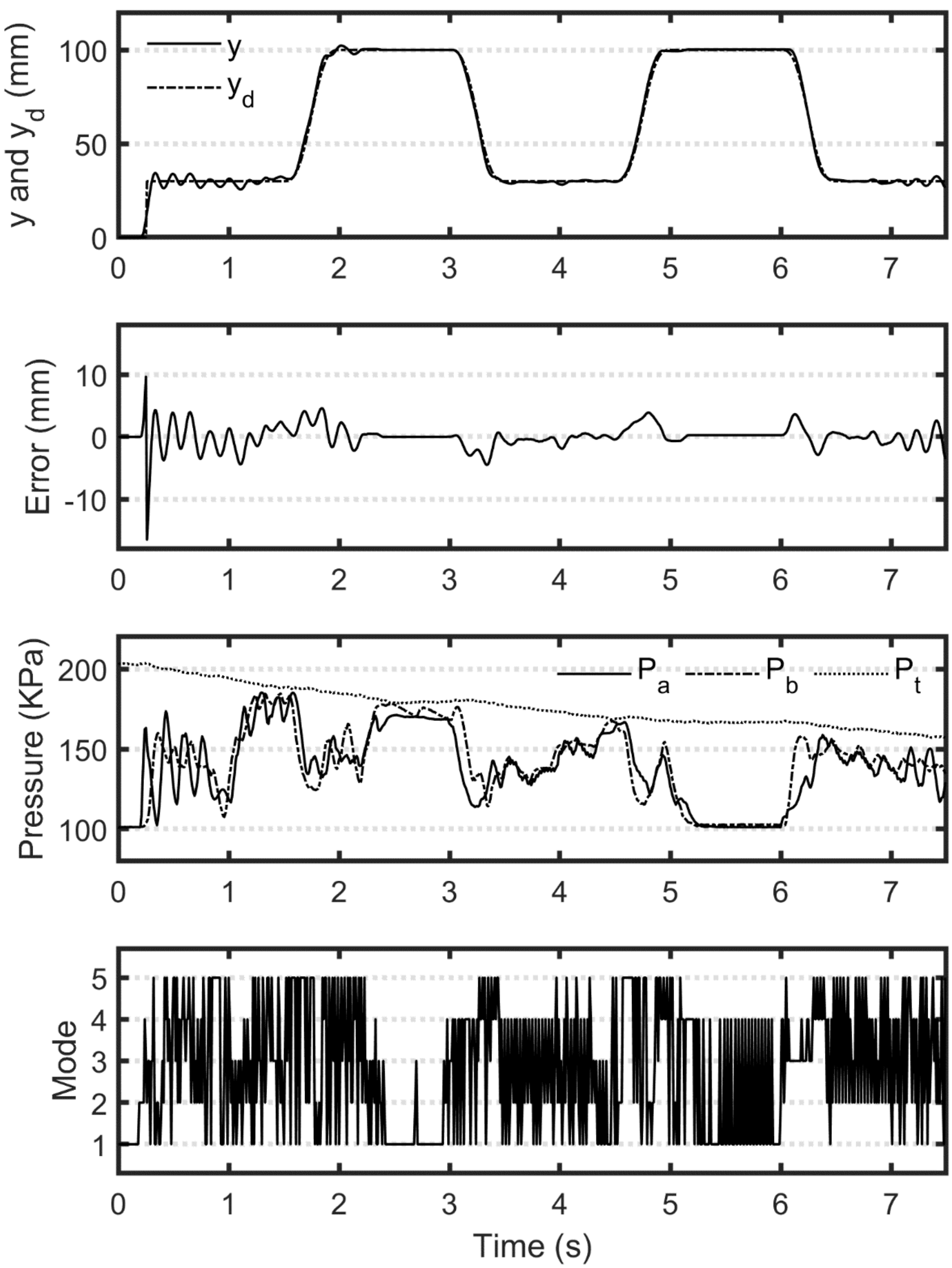

Figure 5.5.3 VC experimental results with

$N_p = 6,\ N_m = 3,\ N_{delta} = 2,\ \omega_i = 1.0,\ \omega_v = 0,\ \omega_{cv} = 0$.

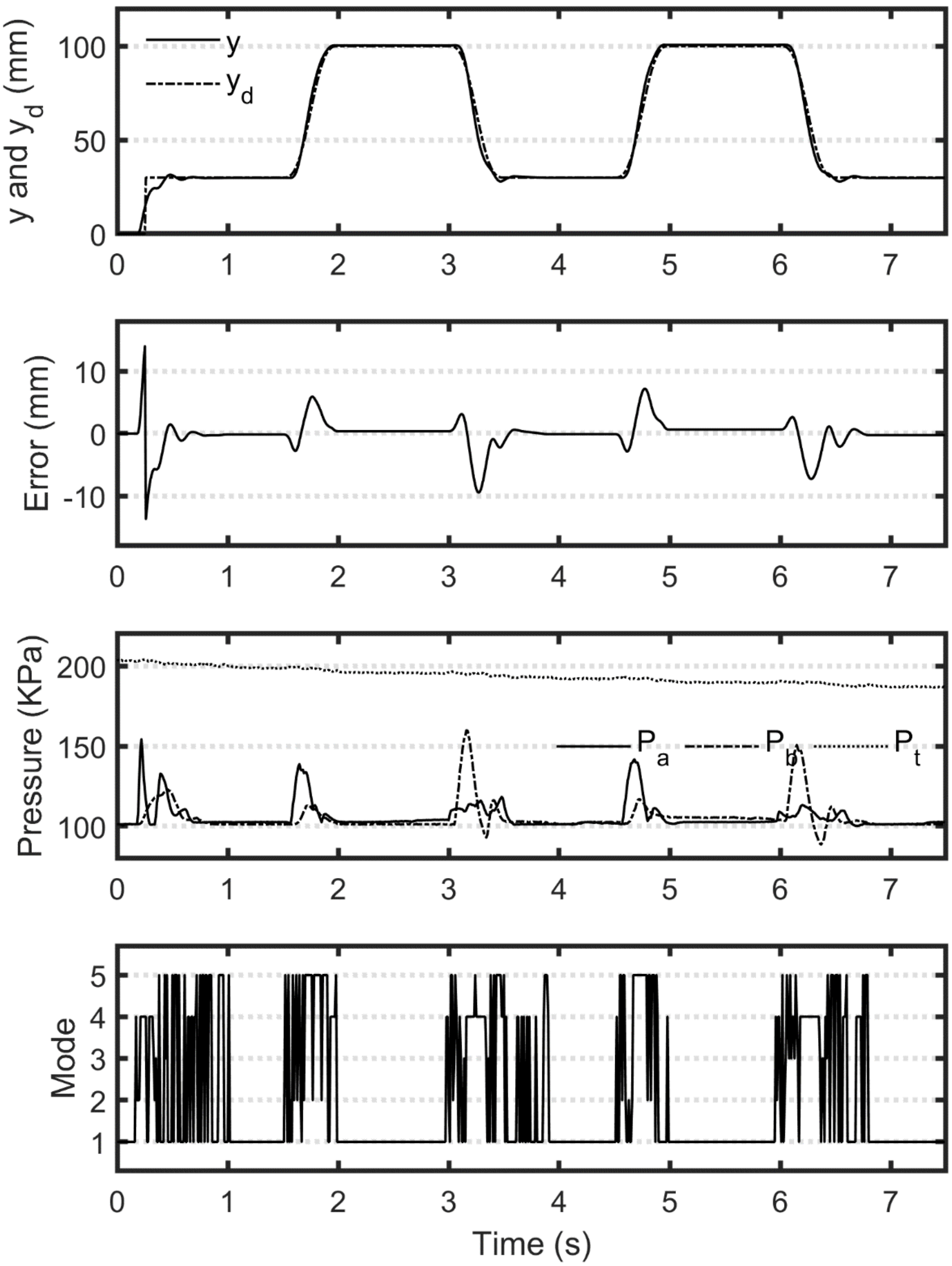

Figure 5.5.4 VC experimental results with

$N_p = 9,\ N_m = 3,\ N_{delta} = 3,\ \omega_i = 1.0,\ \omega_v = 0,\ \omega_{cv} = 0$.

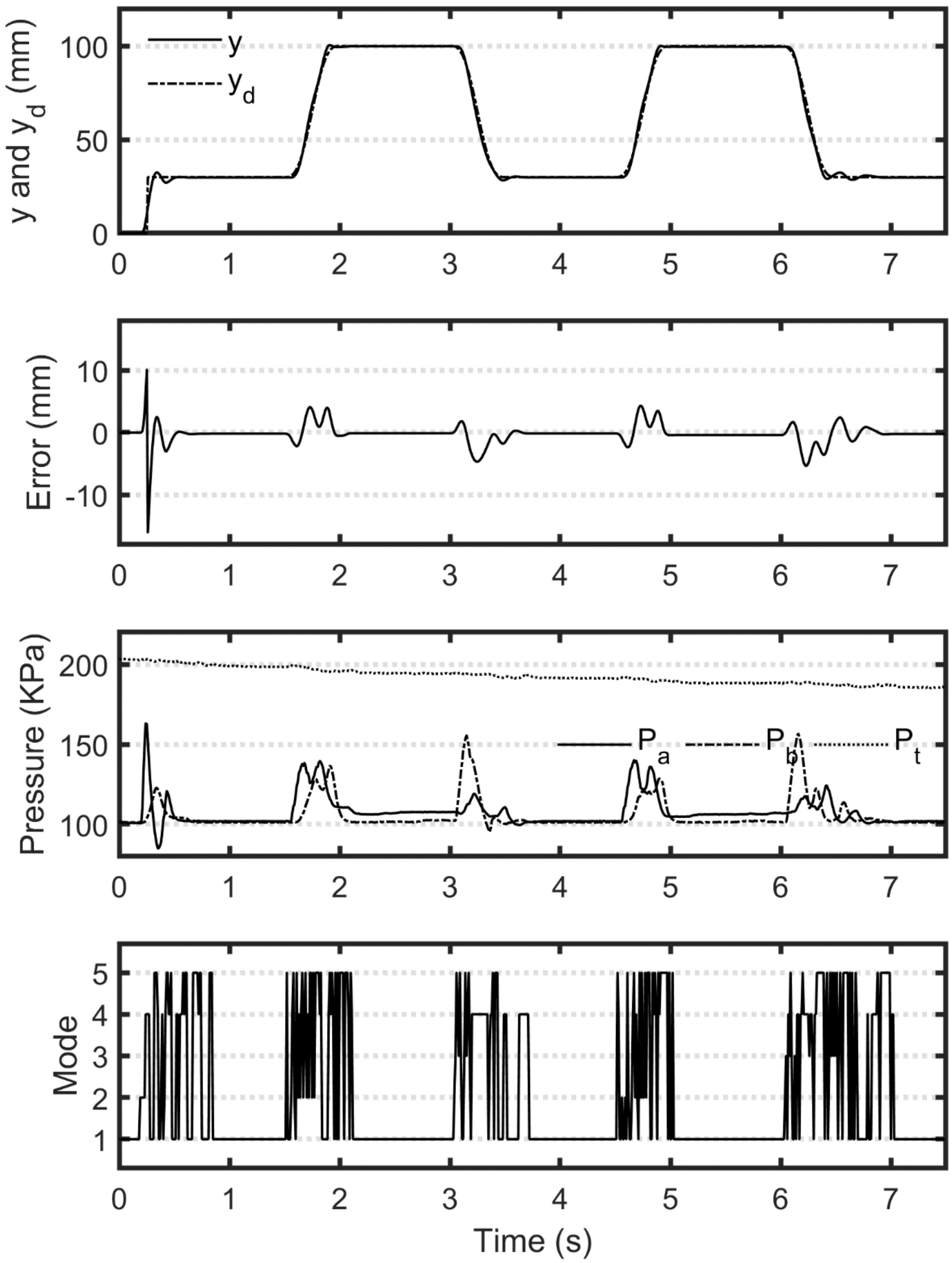

Figure 5.5.5 VC experimental results with

$N_p = 6,\ N_m = 3,\ N_{delta} = 2,\ \omega_i = 1.0,\ \omega_v = 1.0\times10^{-12},\ \omega_{cv} = 4.0\times10^{-3}$.

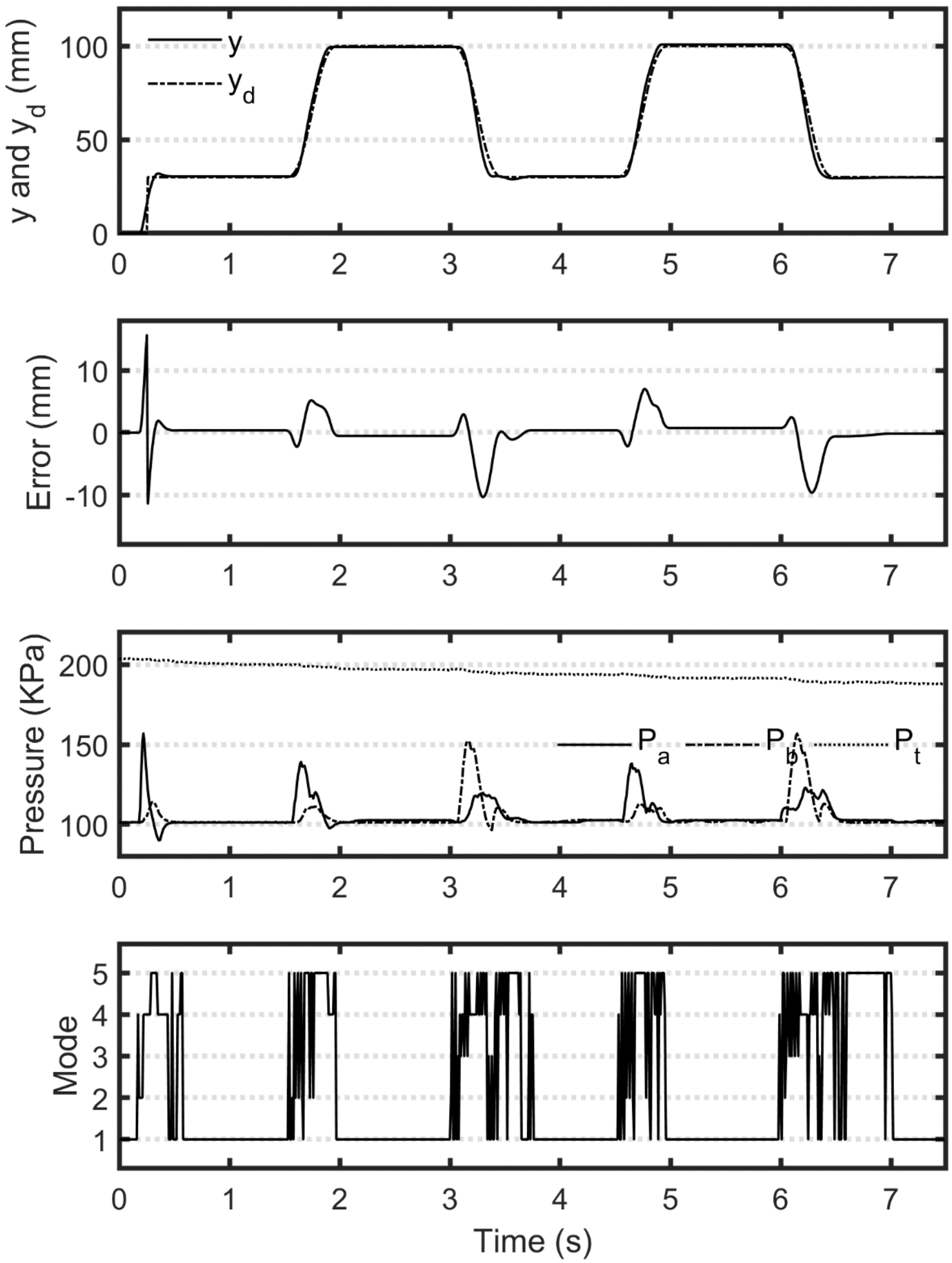

Figure 5.5.6 VC experimental results with

$N_p = 9,\ N_m = 3,\ N_{delta} = 3,\ \omega_i = 1.0,\ \omega_v = 0,\ \omega_{cv} = 1.5 \times 10^{-3}$.

5.6 Long duration experiments

Totally 29 cycloidal curve patterns were included in the setpoint trajectory for the long duration DPC test. The DVMPC3P parameters used were: $N_p = 6$, $N_m = 3$, $N_{delta} = 2$, $\omega_{bi} = 0.45$, $\omega_v = 1.7 \times 10^{-4}$, and $\omega_p = 9.0 \times 10^{-5}$. The position control performance is shown in Figure 5.6.1, and the energy consumption results are shown in Figure 5.6.2. In this 88.5 s test, the system energy consumption reached 618.70 J, with 548.18 J of energy consumed by the pumps, and 70.52 J of energy consumed by the valves.

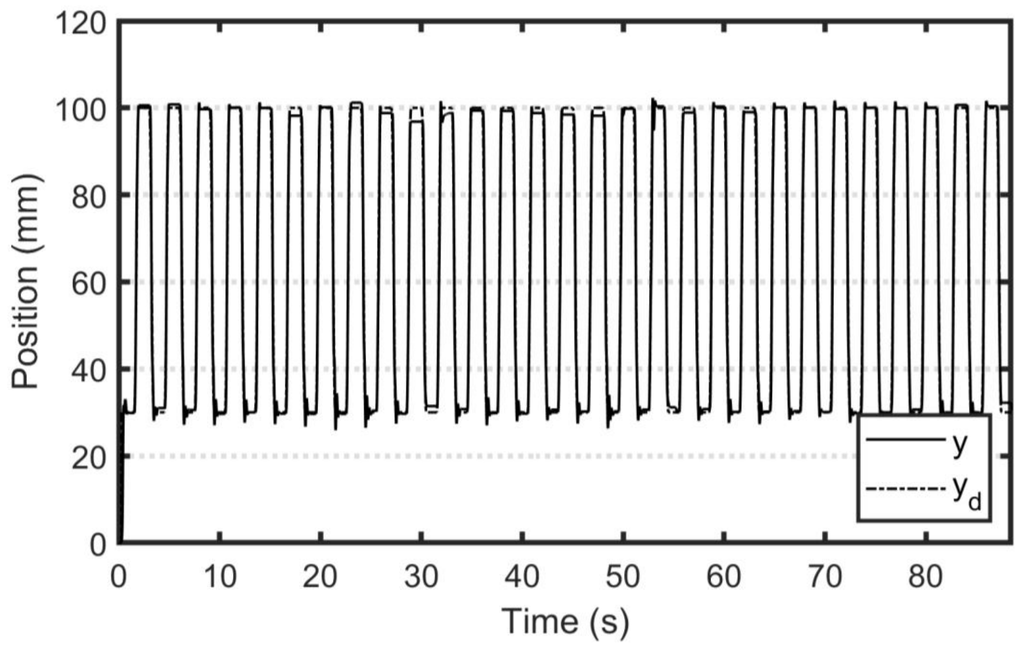

Figure 5.6.1 Position control performance in the long duration DPC experiment.

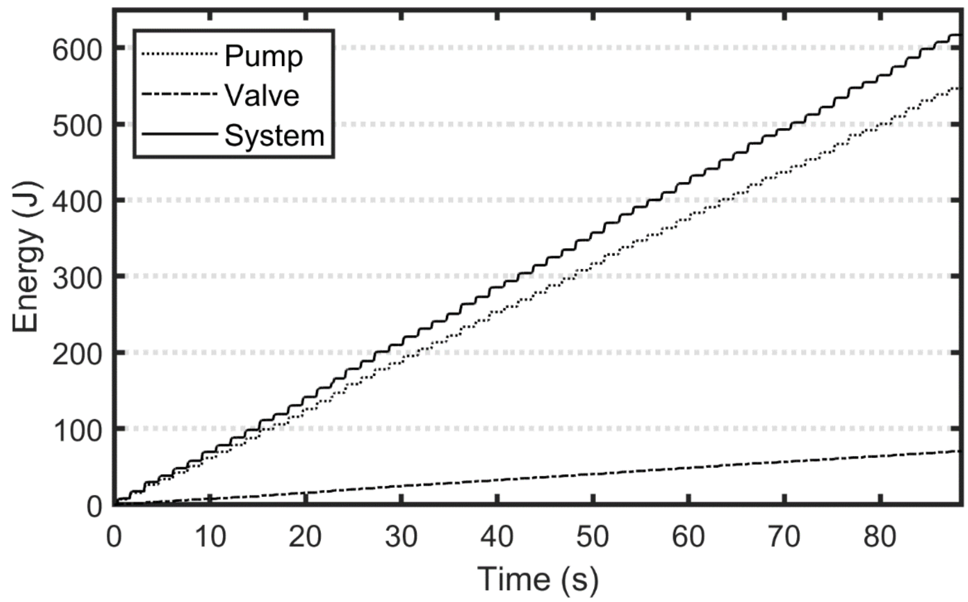

Figure 5.6.2 Energy consumption in the long duration DPC experiment.

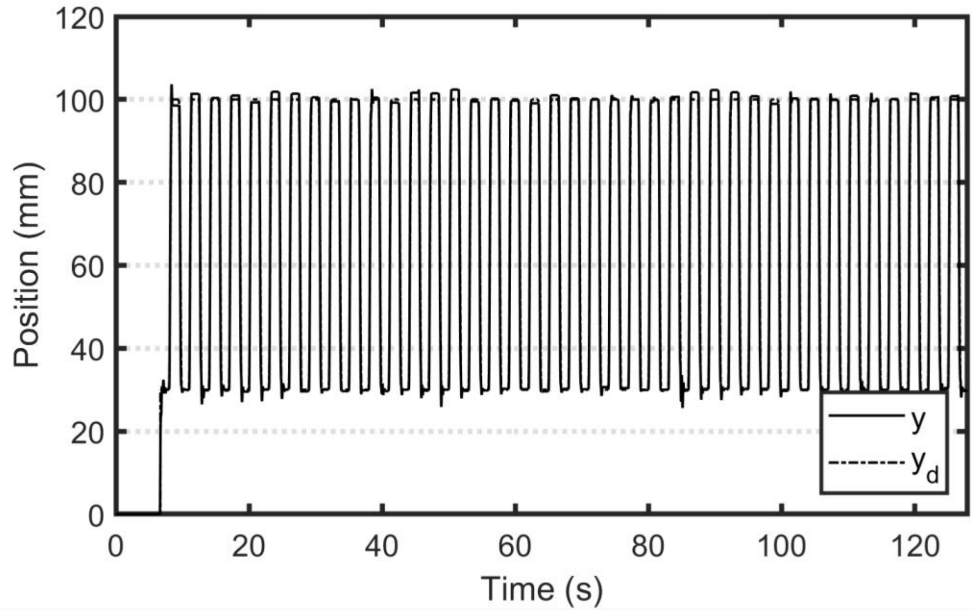

Figure 5.6.3 Position control performance in the long duration VC experiment.

For the long duration VC experiment, the DVMPC3V parameters used were: $N_p = 9$, $N_m = 3$, $N_{delta} = 3$, $\omega_i = 1$, $\omega_v = 0$, and $\omega_{cv} = 1.5\times10^{-3}$. The whole test lasted for 128 s, and the position control performance is shown in Figure 5.6.3. The tank was initially charged to 200 kPa in 6.43 s, then the system began tracking the setpoint trajectory containing 40 cycloidal curve patterns. More patterns were used in this experiment to allow the energy consumption trend to be observed more easily. There were three occurrences of the pump being turned ON to replenish the tank pressure from 150 kPa to 200 kPa. In these replenishments the pump consumed 249.63 J, 233.85 J, and 244.78 J in 3.41 s, 3.24 s, and 3.38 s respectively. Each replenishment supported 12 repetitions of position tracking the cycloidal pattern curve, on average. The tank pressure and pump state during the test are presented in Figure 5.6.4. Pump state = 1 means the pump is ON, while state = 0 means the pump is OFF.

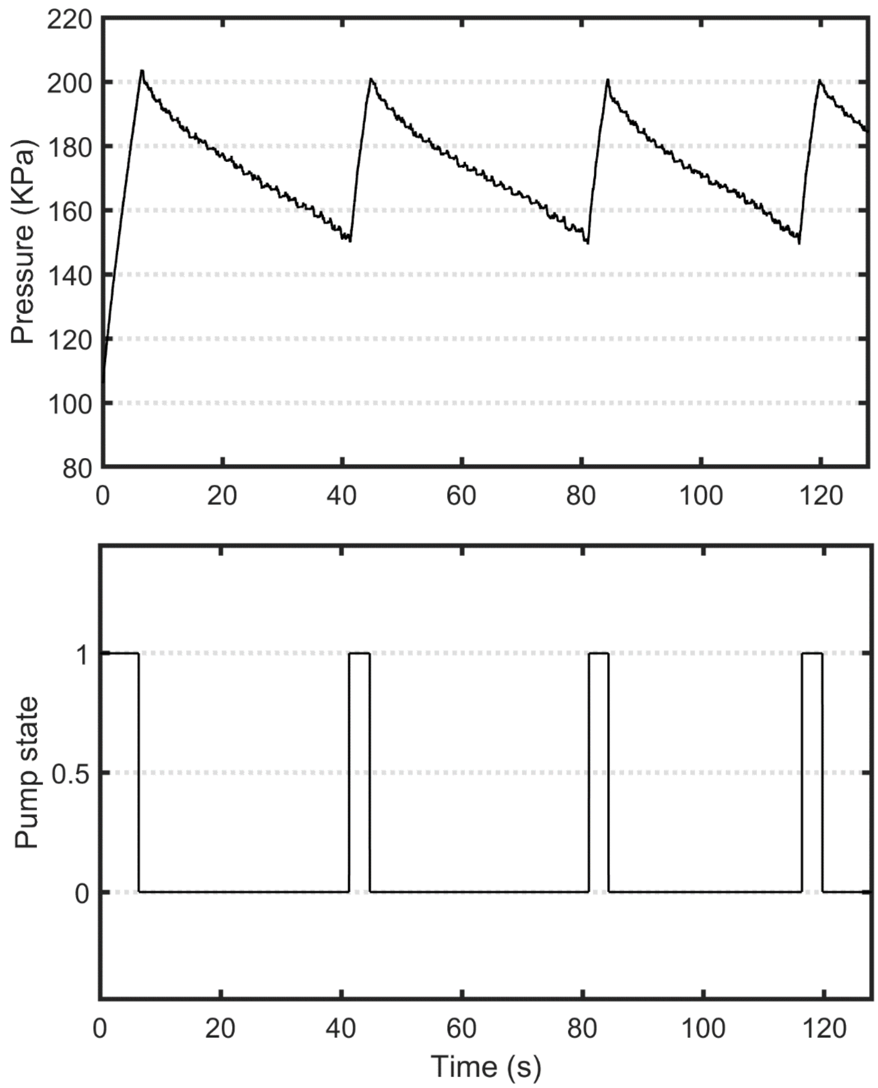

Figure 5.6.4 Tank pressure and pump state in the long duration VC experiment.

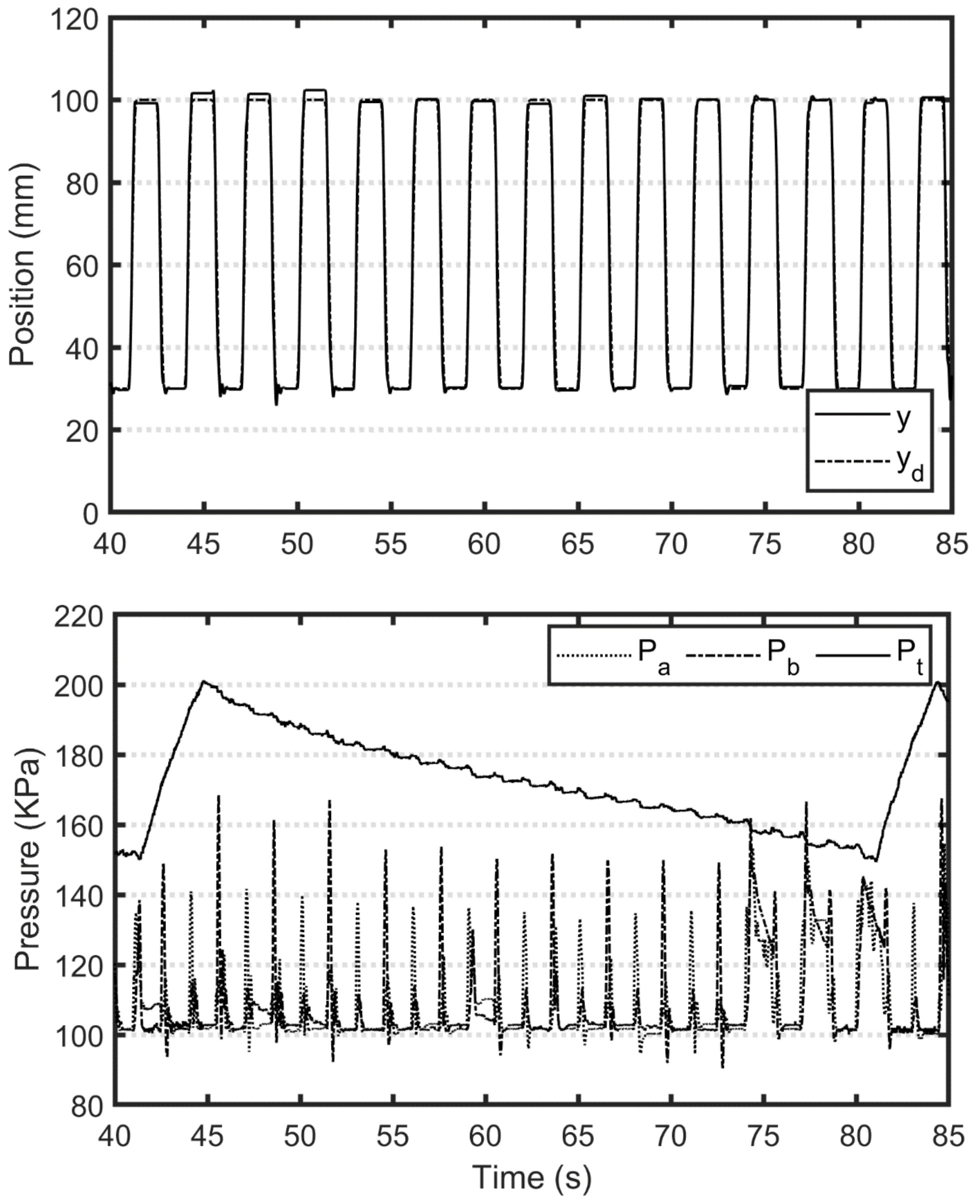

Figure 5.6.5 Position control performance and pressure information in the 40-85 s interval from the long duration VC experiment.

During the tank pressure replenishments, the DVMPC3V algorithm included both the air tank inlet mass flowrate (from the pump) and the tank outlet mass flowrate (to the cylinder) in its predictions. Figure 5.6.5 shows an interval from the experiment where the tank pressure replenished from 150 kPa to 200 kPa, then dropped gradually as the air was consumed to power the motion of the carriage and payload, until it reached the deadband's

150 kPa lower limit and the next replenishment began. The results shown in Figures 5.6.3 and 5.6.5 demonstrate the consistency of the position control during these tank pressure variations. As the tank pressure was raised back to 200 kPa, the system was able to reach the steady state and no excessive OS or oscillation were observed. When the tank pressure was decreasing, the payload still followed the setpoint trajectory well during the transients, although during the 7 s after each replenishment finished larger SSE values (up to ~2 mm) were observed.

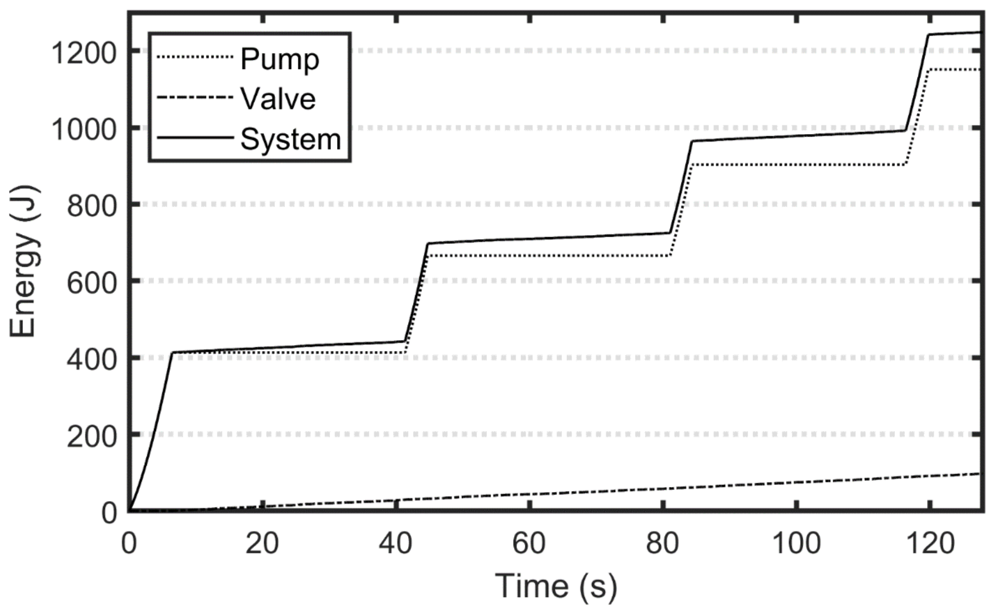

Figure 5.6.6 Energy consumption in the long duration VC experiment.

The energy consumption result of the VC circuit is shown in Figure 5.6.6. The energy of 412.73 J was used for the initial tank pressure charging. This was followed by a repeating pattern of energy consumption caused by the need to periodically replenish the tank. The system energy consumption comparison by working cycles (where 1 cycle refers to the system tracking the setpoint cycloidal curve pattern once) is shown in Figure 5.6.7 and the calculated energy saving proportion is presented in Table 5.6.1. It is obvious that if only a few consecutive working cycles are demanded for the chosen application, DPC is definitely the energy consumption winner. For example, it saved 92.84% of the energy compared with VC when only one working cycle was completed. This ratio steadily declines to 45.44% until the start of the tank pressure being replenished for the first time.

However, 59.17% of the energy could be saved by using DPC for a task involving 13 consecutive working cycles. Similarly, the saving proportions during the second tank replenishment are 29.19% and 42.53% at the 24th and 26th cycles. It can be observed that the energy consumption difference between DPC and VC diminishes as the number of consecutive cycles increases. However, unless there is zero leakage in the system and the tank is perfectly insulated, any time gap between cycles will negatively impact the energy consumption of VC, but not alter the energy consumption of DPC.

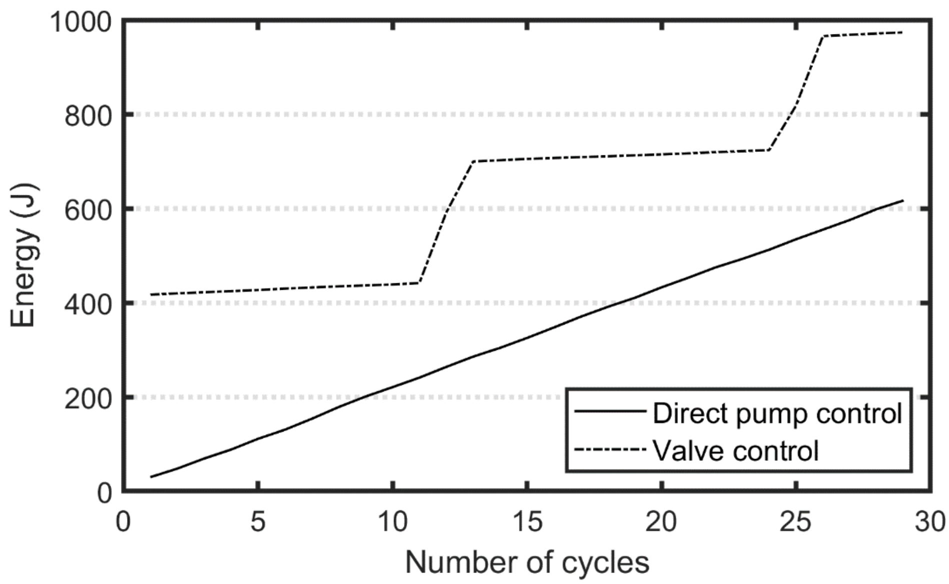

Figure 5.6.7 System energy consumption comparison in the first 29 working cycles.

Table 5.6.1 Comparison of energy consumption of the two circuits by number of cycles.

	1	11	13	24	26	29
Energy consumption of DPC (J)	29.86	240.94	285.57	512.34	554.96	616.84
Energy consumption of VC (J)	417.09	441.62	699.50	723.55	965.62	973.53
Saving proportion	92.84%	45.44%	59.17%	29.19%	42.53%	36.64%

To make a quantitative comparison of the position control performance, we also calculated the RMSE, MAE, MSSE, and MOS based on the first 29 working cycles. These results are presented in Table 5.6.2.

Table 5.6.2 Comprehensive performance comparison between the two circuits.

	RMSE (mm)	MAE (mm)	MSSE (mm)	MOS (mm)	SDSSE (mm)	Initial energy consumption (J)	Initialization time (s)
DPC	2.07	1.29	0.59	1.62	0.62	0	0
VC	2.58	1.49	0.54	0.97	0.61	412.73	6.44

5.7 Conclusions

The following conclusions can be made based on the collected data and related information:

1. The results in Table 5.6.2 show that the position control performances of the two circuits are quite similar. Specifically, for DPC, the RMSE and MAE are 19.77% and 13.42% lower than those of VC. However, the MSSE is 0.59 mm, and the MOS is 1.62 mm, which are 9.26% and 67.01% higher than VC's results. This means the VC has better steady state precision, while the DPC is superior at tracking the setpoint trajectory transients of the cycloidal curves. Regarding the comparison of SSE repeatability, the calculated SDSSE results are very close, with 0.62 mm for DPC and 0.61 mm for VC.
2. Based on the results in Table 5.6.1, 92.84% of the system energy was saved using DPC with one working cycle, and 36.64% was saved when the number of working cycles was increased to 29.
3. VC requires the air tank to be charged before performing position control. Unlike VC, DPC can respond to the setpoint trajectory at any time, and the circuit can have more compact design, since an air tank is unnecessary. Also, if the cycles are performed intermittently, then leakage losses and thermal loses will increase

the energy consumption of VC in comparison to DPC. In addition, VC's pressurized tank is a potential safety hazard, especially in wearable robotics applications.

Chapter 6 – Conclusions

6.1 Summary

In this research, the energy saving position control of VC and DPC pneumatic circuits was presented. For each circuit, a DVMPC controller was developed for the position control task, and, to further reduce the energy consumption, terms predicting the pump and valve energy consumptions were included in the cost function. A novel air pump subsystem model and a novel position-dependant friction model of the cylinder subsystem were proposed to help the DVMPC controllers make more accurate predictions. All of the models were validated by comparing simulation and experimental results. Finally, the designed pneumatic circuits with corresponding controllers were tested and compared.

6.2 Achievements

The main achievements of this thesis are summarized as follows.

(1) This research studied the two energy saving position control schemes for pneumatic actuators: DPC and VC. Their system performances on position control and energy consumptions were comprehensively compared based on the experimental results. The concept and implementation of pneumatic DPC with model-predictive control is original, providing a new perspective on the design and implementation of energy saving pneumatic system for position control application.

(2) A novel air pump subsystem model was developed to predict the air pump performance over a wide range of working conditions. The subsystem includes the motor dynamics described by the ARX model; mass flow rate model built as a polynomial function of motor speed and outlet pressure; and the pump energy consumption model built as a polynomial function of motor speed and outlet pressure. The modeling accuracy within the prediction horizon were validated by comparing simulation and experimental results.

(3) A novel model of the friction of the cylinder subsystem and a novel characterization method were proposed. The characterization method processed the data from closed-loop tests, rather than the tradition open-loop approach. The processed data showed the position dependence of the friction force. As a result, the static friction

was modeled as a function of carriage position, and dynamic friction was modeled as a second order polynomial function of carriage position and velocity. A comparison of simulation and experimental results showed that the model predicts the friction well over the duration of the DVMPC's prediction horizon.

(4) Model predictive controllers (DVMPC3P and DVMPC3V) with inner air pump motor speed PID control loops were designed and implemented for DPC and VC.

(5) The effects of the DVMPC parameters on the position control performance and energy consumption were investigated.

(6) The long duration experiments demonstrated that the position control performances of DPC and VC were similar. For DPC, the MSSE was 0.59 mm, and the MOS was 1.62 mm, which are 9.26% and 67.01% higher than VC's results. However, the RMSE and MAE of DPC are lower than those of VC, which means DPC was superior at tracking the setpoint trajectory transients of the cycloidal curves and VC had better steady state precision. On the other hand, DPC was proven to be a more energy efficient scheme: 92.84% of the system energy was saved using DPC with one working cycle, and 36.64% was saved when the number of working cycles was increased to 29.

6.3 Recommendations for future work

Since the work presented in this thesis is the first step to push the idea of position controlling a pneumatic DPC circuit into practice, there many avenues for future research. These two are recommended to be explored first:

(1) A few other controllers like SMC and conventional MPC should be implemented for the two circuits. A comparison of the position control performance and energy consumptions with these controllers with those of the proposed DVMPC controllers should clearly demonstrate the benefits of the proposed controllers.

(2) Experiments should be conducted to test the robustness of the designed controllers. This could be realized by increasing and decreasing the mass of payload and studying their effects on the performance metrics.

References

Al-Dakkan, K. A., Barth, E. J., & Goldfarb, M. (2006). Dynamic constraint-based energy-saving control of pneumatic servo systems. *Journal of Dynamic Systems, Measurement and Control, Transactions of the ASME*, *128*(3), 655–662. https://doi.org/10.1115/1.2232688

Azzi, A., Maoui, A., Fatu, A., Fily, S., & Souchet, D. (2019). Experimental study of friction in pneumatic seals. *Tribology International*, *135*, 432–443. https://doi.org/10.1016/j.triboint.2019.03.018

Bone, G., & Chen, X. (2012). Position Control of Hybrid Pneumatic-Electric Actuators. *American Control Conference*, 1793–1799.

Bone, G. M., & Ning, S. (2007). Experimental comparison of position tracking control algorithms for pneumatic cylinder actuators. *IEEE/ASME Transactions on Mechatronics*, *12*(5), 557–561. https://doi.org/10.1109/TMECH.2007.905718

Bone, G. M., Xue, M., & Flett, J. (2015). Position control of hybrid pneumatic-electric actuators using discrete-valued model-predictive control. *Mechatronics*, *25*, 1–10. https://doi.org/10.1016/j.mechatronics.2014.10.009

Doll, M., Neumann, R., & Sawodny, O. (2015). Dimensioning of pneumatic cylinders for motion tasks. *International Journal of Fluid Power*, *16*(1), 11–24. https://doi.org/10.1080/14399776.2015.1012437

Du, H., Xiong, W., Jiang, Z., Li, Q., & Wang, L. (2018). Energy efficiency control of pneumatic actuator systems through nonlinear dynamic optimization. *Journal of Cleaner Production*, *184*, 511–519. https://doi.org/10.1016/j.jclepro.2018.02.117

Du, H., Xiong, W., Xu, C., & Jiang, Z. (2017). Research on the controllability and energy saving of the pneumatic direct drive system. *International Journal of Heat and Technology*, *35*(4), 997–1004. https://doi.org/10.18280/ijht.350436

Falcão Carneiro, J., & De Almeida, F. G. (2006). Reduced-order thermodynamic models for servo-pneumatic actuator chambers. In *Proceedings of the Institution of Mechanical Engineers. Part I: Journal of Systems and Control Engineering* (Vol. 220, Issue 4, pp. 301–314). https://doi.org/10.1243/09596518JSCE203

Falcão Carneiro, J., & De Almeida, F. G. (2012). A neural network based nonlinear model of a servopneumatic system. *Journal of Dynamic Systems, Measurement and Control, Transactions of the ASME*, *134*(2). https://doi.org/10.1115/1.4005360

Han, J., & Toshiro, N. (2003). Pneumatic position control system directly driven by a miniature air compressor. *Chinese Journal of Mechanical Engineering*, *39*(6).

Harris, P. G., O'Donnell, G. E., & Whelan, T. (2012). Modelling and identification of industrial pneumatic drive system. *International Journal of Advanced Manufacturing Technology*, *58*(9–12), 1075–1086. https://doi.org/10.1007/s00170-011-3447-7

Hepke, J., & Weber, J. (2013). *Energy saving measures on pneumatic drive systems*.

Hu, J., Yang, L., Shao, L. L., & Zhang, C. L. (2014). Generic network modeling of reciprocating compressors. *Energy Economics*, *45*, 107–119. https://doi.org/10.1016/j.ijrefrig.2014.06.007

Jiménez, M., Kurmyshev, E., & Castañeda, C. E. (2020). Experimental Study of Double-Acting Pneumatic Cylinder. *Experimental Techniques*, *44*(3), 355–367. https://doi.org/10.1007/s40799-020-00359-8

Lyu, L., Chen, Z., & Yao, B. (2019a). Energy Saving Motion Control of Independent Metering Valves and Pump Combined Hydraulic System. *IEEE/ASME Transactions on Mechatronics*, *24*(5), 1909–1920. https://doi.org/10.1109/TMECH.2019.2930276

Meng, D., Tao, G., Chen, J., & Ban, W. (2011). Modeling of a pneumatic system for high-accuracy position control. *Proceedings of 2011 International Conference on Fluid Power and Mechatronics, FPM 2011*, 505–510. https://doi.org/10.1109/FPM.2011.6045817

Merkelbach, S. (2015). *EXERGY BASED ANALYSIS OF PNEUMATIC AIR SAVING MEASURES*. http://asmedigitalcollection.asme.org/FPST/proceedings-pdf/FPMC2015/57236/V001T01A007/4455384/v001t01a007-fpmc2015-9513.pdf

Ning, Shu., & Bone, Gary. (2005). *Development of a Nonlinear Dynamic Model for a Servo Pneumatic Positioning System*.

Pérez-Segarra, C. D., Rigola, J., & Oliva, A. (2003). *Modeling and Numerical Simulation of the Thermal and Fluid Dynamic Behavior of Hermetic Reciprocating Compressors-Part 1: Theoretical Basis*.

Qi, H., Bone, G. M., & Zhang, Y. (2019a). Position control of pneumatic actuators using three-mode discrete-valued model predictive control. *Actuators*, *8*(3). https://doi.org/10.3390/ACT8030056

Rad, C. R., & Hancu, O. (2017). An improved nonlinear modelling and identification methodology of a servo-pneumatic actuating system with complex internal design for high-accuracy motion control applications. *Simulation Modelling Practice and Theory*, *75*, 29–47. https://doi.org/10.1016/j.simpat.2017.03.008

Rao, Z., & Bone, G. M. (2008a). Nonlinear modeling and control of servo pneumatic actuators. *IEEE Transactions on Control Systems Technology*, *16*(3), 562–569. https://doi.org/10.1109/TCST.2007.912127

Rigola, J., Pérez-Segarra, C. D., & Oliva, A. (2003). *Modeling and Numerical Simulation of the Thermal and Fluid Dynamic Behavior of Hermetic Reciprocating Compressors-Part 2: Experimental Investigation*.

Rouzbeh, B., & Bone, G. M. (2020). Optimal force allocation and position control of hybrid pneumatic-electric linear actuators. *Actuators*, *9*(3). https://doi.org/10.3390/act9030086

Tanveer, M. M., & Bradshaw, C. R. (2020). Quantitative and qualitative evaluation of various positive-displacement compressor modeling platforms. *International Journal of Refrigeration*, *119*, 48–63. https://doi.org/10.1016/j.ijrefrig.2020.07.009

Valdiero, A. C., Ritter, C. S., Rios, C. F., & Rafikov, M. (2011). Nonlinear mathematical modeling in pneumatic servo position applications. *Mathematical Problems in Engineering*, *2011*. https://doi.org/10.1155/2011/472903

Vittorini, D., & Cipollone, R. (2016). Energy saving potential in existing industrial compressors. In *Energy* (Vol. 102, pp. 502–515). Elsevier Ltd. https://doi.org/10.1016/j.energy.2016.02.115

Wehner, M., Tolley, M. T., Mengüç, Y., Park, Y. L., Mozeika, A., Ding, Y., Onal, C., Shepherd, R. F., Whitesides, G. M., & Wood, R. J. (2014). Pneumatic Energy Sources for Autonomous and Wearable Soft Robotics. *Soft Robotics*, *1*(4), 263–274. https://doi.org/10.1089/soro.2014.0018

Xiangrong, S., & Goldfarb, M. (2007a). Energy saving in pneumatic servo control utilizing interchamber cross-flow. *Journal of Dynamic Systems, Measurement and Control, Transactions of the ASME*, *129*(3), 303–310. https://doi.org/10.1115/1.2718244

Zhang, Y. (2015). Comparison of Sliding-mode Control and Model-predictive Control Algorithms for Pneumatic Actuators. [Master’s thesis]. McMaster University.